ΠΟΛΥΤΕΧΝΕΙΟ ΚΡΗΤΗΣ
TECHNICAL UNIVERSITY OF CRETE

Technical University of Crete
School of Electrical and Computer Engineering

DIPLOMA THESIS

Dielectric properties of pole insulation of traction motors under constant thermal ageing

---

Author: Dimitrios Glykos

Thesis Committee:
Associate Professor Konstantinos Gyftakis
Professor Eftychios Koutroulis
Dr. Eleftheria Sergaki

JULY 2024

Acknowledgments

I would like to extend my heartfelt gratitude to all those who have played a part, big or small, in the realization of this thesis. First and foremost, I am immensely grateful to my thesis supervisor Konstantinos Gyftakis, whose unwavering support, valuable guidance and expertise have been a cornerstone in shaping the direction and focus of this thesis. Special thanks to my collaborators Antonios Douvaras, Dimitrios Chronopoulos and Nikitas Ravanis. Their dedication to our collective research efforts significantly enhanced the depth and quality of this work. The synergy we achieved in conducting the experiments and analyzing the results has played a pivotal role on the outcome of this thesis. I am also grateful to Athanasios Malisovas, a nominated PhD student, for his generous assistance regarding the installation of the experiments' equipment. Last but not least, I would like to extend my sincere appreciation to my family, my friends and especially to Alexandra Koutromanou, whose support, encouragement and understanding have been my pillars of strength throughout this academic journey.

Abstract

This diploma thesis is a study of the behavior of the dielectric properties of the pole insulation of a permanent magnet synchronous axial flux motor having the yokeless and segmented armature topology when these poles are subjected to constant thermal aging. As the need to reduce the burning of fossil fuels leads to the gradual widespread adoption of electric vehicles, this type of motor is increasingly used due to its reliability, high torque density, compact structure and high efficiency. The windings of this motor are insulated to protect the turns of the coils from stator faults. Among them, the inter-turn short circuits pose a significant threat to the condition of insulation systems due to their rapid evolution into catastrophic breakdowns. However, various stresses may arise in the environment of the motor during its operation, which are associated with insulation degradation and failure. These are known as TEAM stresses, an abbreviation for Thermal, Electrical, Ambient and Mechanical stresses. This thesis aims to provide significant insights into the behavior of the windings insulation after the application of fixed thermal stress. First, the characteristics of the electric motors used in electric vehicles (EVs) are outlined, emphasizing on the permanent magnet synchronous motors (PMSM). Next, the potential faults that can occur are analyzed, including electrical, mechanical and magnetic faults. Additionally, the widely employed diagnostic methods are described that aim at early fault detection. Subsequently, the pole insulation systems are discussed, insulation degradation with the increase of partial discharge activity is analyzed and the diagnostic tests to assess the insulation condition are described. Moreover, the thesis delves into fixed thermal stress testing as an accelerated aging mechanism along with relevant literature on constant thermal aging testing with their respective experimental outcomes. The experimental procedure encompasses the development of quality testing procedures, modeling the equivalent circuit of the poles, conducting experimental tests and the analysis of the applied fixed thermal stresses on the poles. Impedance spectroscopy, Nyquist diagrams and breakdown voltage measurements are the primary methods for monitoring and evaluating the insulation condition of the poles. A frequency response (FRAX) analyzer and an Insulation Resistance Tester (Megohmmeter) are utilized as the main measuring equipment. Particularly, the performed work on the development of the complex equivalent circuit for the poles is described. Then the impact of different temperatures acting as different fixed thermal stresses on the pole insulation is explored, elevating gradually the temperature between the cycles. Their results are recorded using the aforementioned diagnostic tools after each cycle to assess the insulation degradation. The thermal cycling test is also investigated to highlight the impact of the thermomechanical effects observed during this test on the insulation. Furthermore, multi- stress mechanisms are examined using a specially designed mechanical accelerator to conduct electromechanical stress testing, following the thermal aging procedures.

Contents

1 Theoretical background

1.1 Introduction

In today's era, where the climate crisis is just around the corner, with more and more environmental issues on the table to be addressed, the transition to a sustainability strategy is an urgent need. As urban centers grapple with escalating air pollution levels, especially in huge cities, while the pressing need to curb greenhouse gas emissions, the automotive industry strands at a crossroads. Conventional internal combustion engine vehicles contribute significantly to the abbreviation of these problems, as they burn millions of tons of fossil fuels each year. That is why, the imperative of widespread adoption of electric vehicles (EVs) presents a compelling solution to mitigate these environmental challenges.

The inherent advantage of electric vehicles lies in their zero-emission nature, as they rely on electric power resources, such as batteries, to propel vehicles. By choosing EVs, individuals and societies actively contribute to the reduction of the carbon footprint and the adverse effects of climate change. Beyond that, this transition encompasses a strategic move towards energy efficiency and technological innovation. As countries strive to achieve sustainable development goals, the transportation sector plays a critical role. Electric vehicles not only align with global efforts to reduce dependence on fossil fuels but also foster the growth of more efficient energy systems. The rise of the electric vehicle industry leads to advancements in other industries, such as battery development, charging infrastructure, and smart grid integration, stimulating a phenomenon of innovation across various sectors.

In essence, the shift towards electric vehicles is not just an environmental necessity, but a strategic and forward-thinking approach to reshape the future of mobility, energy, and the overall sustainability of our planet. Governments and businesses will have to recognize the necessity of this transition, investing in the development of electric vehicles, but always with a view to their reliability and viability for humans.

1.2 Electric vehicles

An electric vehicle is a vehicle, that is being run with the aid of an electric propulsion system. There are several categories of electric vehicles, the classification of which is based on the energy system they use. The main categories of EVs consist of battery-powered electric vehicles (BEV), which rely solely on a battery for energy storage, hybrid electric vehicles (HEV), which use both electric and internal combustion engines, depending on whether they move at low speeds in urban areas or higher and fuel cell electric vehicles (FCEV), which use fuel cells, inside of them multiple chemical reactions take place to produce electricity [1]. The block diagram in Figure 1.1 captures the basic propulsion system of an EV, which includes an energy source, a power converter, a kind of electric motor and a vehicle transmission system, all connected with each other. The energy source can be based on batteries, particularly those of lithium technology, or supercapacitors, which are high-capacity capacitors with capacitance values much higher than sold-state capacitors but with lower voltage limits. A lot of research has been done on supercapacitors and fuel cells, as they seem very promising options for electromobility due to their high power and longer life cycles.

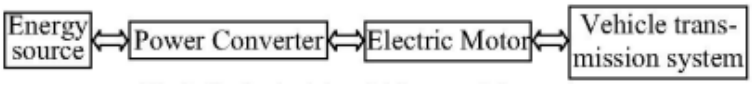

Figure 1.1: Basic electric vehicle propulsion system [1]

The overall performance of an EV is primarily determined by the motor drive type being

utilized. The motor drive is one of the most important parts of the propulsion system and consists of the electric motor, the converter and the electronic controller. The latter two facilitate efficient power conversion, precise motor control and seamless integration with various vehicle functions.

1.3 Electric motors used in EVs

The heart of an electric vehicle lies in its electric motor, the most important component of the propulsion system. There are various types of traction motors used in EVs. The selection of the proper one is a pivotal stage in the design of the overall electric vehicle system, which depends on different factors such as cost, reliability, durability, efficiency, high power and torque density and robustness[2]. Motors that are mostly used are direct current (DC) motors, induction motors, switched reluctance motors (Switched RM), permanent magnet synchronous motors (PMSM) and brushless DC motors (BLDC). They are shown in Figure 1.2.

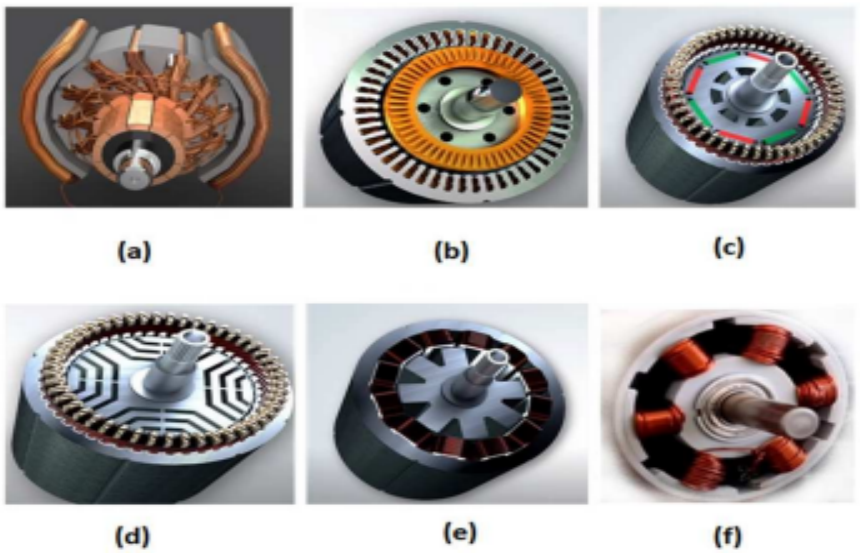

Figure 1.2: Cross section of motor types: a)DC motor, b)Induction motor, c)PMSM, d)Synchronous RM, e)Switched RM, f)BLDC motor.[3]

1.3.1 DC motors

Renowned for its straightforward construction, the ease of decoupling flux and torque and the uncomplicated control, this particular type of motor is characterized by simplicity. Predating advancements in power electronics, DC motors were conventionally utilized in various speed applications. They are favored for their ability to deliver high torque at low speeds. The commutator converts DC to AC, acting as an inverter, making power electronics devices much simpler and more cost-effective. Nevertheless, the presence of brushes and rings, requiring periodic replacement, contributes to increased difficulty in construction, high maintenance cost, reduced reliability and low efficiency. The collector also is responsible for torque ripples and imposes limitations on the motor's maximum speed.

In Figure 1.3, the inversely proportional relationship between the speed and the torque output of the motor can be shown. This is because the rated output power has a fixed value. As the output speed increases, the available output torque decreases proportionately, while as the output torque increases, the speed decreases proportionately. The point where the torque is maximum and the speed is zero is called holding torque, while the point where the speed is maximum and the torque is zero is called no load speed.

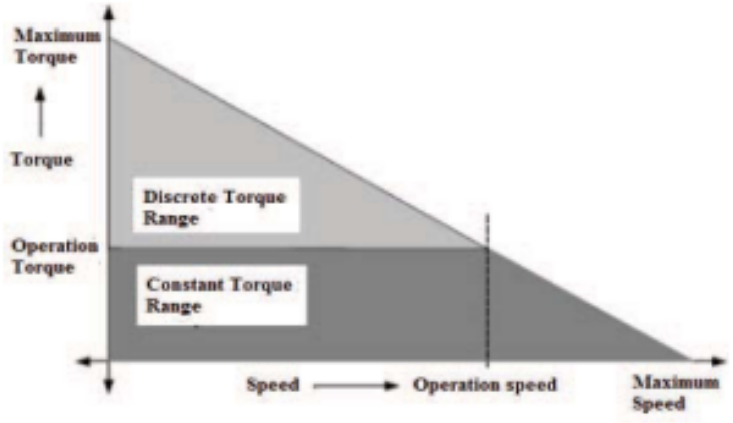

Figure 1.3: Torque-speed characteristic of DC motors [4]

1.3.2 Induction motors

Induction motors (IMs) are also called asynchronous motors because their rotor never operates at the same speed as the rotating magnetic field produced by the stator. Specifically squirrel cage induction motors are a widespread selection for applications in the automotive industry because of their robustness, reliability and simple structure. Hence there are fewer maintenance requirements and low cost. They can operate in harsh or poor environmental conditions as well.[4] The main reason for their use in electric vehicle applications is their speed-torque characteristic, which is very close to the ideal one. The main characteristics of an induction motor are shown in Figure 1.4. The torque and field control can be divided and easily controlled by vector control methods. By reducing the flux, the speed range may be extended in the constant power region.

Besides the advantages, there are also some drawbacks presented in induction motors. Because of the presence of rotor winding losses, they present inherently lower efficiency, particularly at low speeds, as compared to a permanent magnet motor. In addition, the existence of the break-down torque within the constant power region and the increment of losses at high speeds are some other negative features. Therefore, they have a low power factor. Due to their low torque density, IMs are more suitable for high-speed and low-torque applications. Their overall volume and weight are also increased as the batteries in EVs are direct current sources, so the existence of an inverter, which converts the direct current to alternating current, is necessary for their operation. Researchers have invested significant efforts in addressing these problems through various approaches. These include using dual inverters to expand the constant power region, incorporating doubly-fed induction motors for enhanced low-speed performance and mitigating rotor winding losses during the design stage.

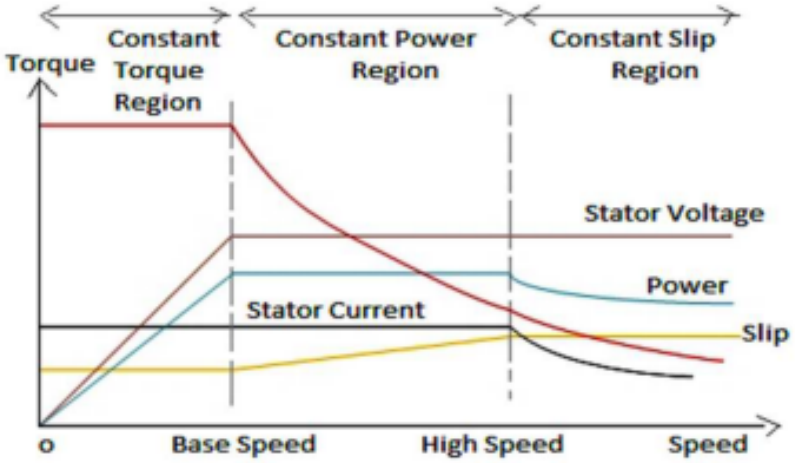

Figure 1.4: Induction motor characteristics [3]

1.3.3 Switched Reluctance motors

Switched reluctance motors (SRM) are a category of electric motors that operate based on the principle of magnetic reluctance, which represents the opposition to magnetic flux. Simple and strong in construction the rotor of this motor is a single piece of laminated steel with no windings or permanent magnets on it. That is why, these motors do not have a continuous magnetic field in the stator or the rotor. Instead, they rely on the variation in reluctance to generate motion. More specifically, the stator windings are energized in a sequence to create a magnetic field to attract the rotor poles. Due to magnetic attraction, the rotor is getting aligned with the stator poles. Once aligned, the stator windings are immediately de-energized. Thus, the rotor can move to its next position because of its inertia. The sequence of energizing and de-energizing the stator windings produces the required rotational motion[5].

SRMs are becoming an increasingly popular choice for Hybrid Electric Vehicles (HEVs), as their efficiency is over 95%. Its robust nature makes it suitable for high-speed applications. The inertia of the rotor is lower compared to the rotor of other machines due to the operating principle described earlier. Hence, these motors are a viable choice for variable reference speed applications to capture reference speed, where low inertia is a significant factor. Among the advantages of this type of motor is the fact they are rigid in construction and easily controllable. They are also fault-tolerable since there is no connection between the phases, so if one of the phases stops working the motor continues to operate.[6] Due to the lack of rotor copper losses, they can operate at high temperatures, because the temperature of the rotor itself is lower than other motors. Furthermore, the absence of magnets, collector and brushes ensures low production and maintenance costs, as no maintenance is required at all.

Unlike other electric motors, they exhibit high torque fluctuations owing to their independent phase power supply, acoustic noise, electromagnetic interference (EMI) and vibrations due to salient-pole rotor and stator, leading to a non-linear magnetic characteristic for the motor. For that reason, a special convertor topology is needed for operation. Moreover, a drive is necessary during initial acceleration and gradeability to maintain constant power. Proper motor design can extend the constant power region [7]. The torque-speed characteristic of the SRM is depicted in Figure 1.5b. This characteristic is particularly advantageous for electric vehicle applications, as the broad constant power region enables operation at high speeds.

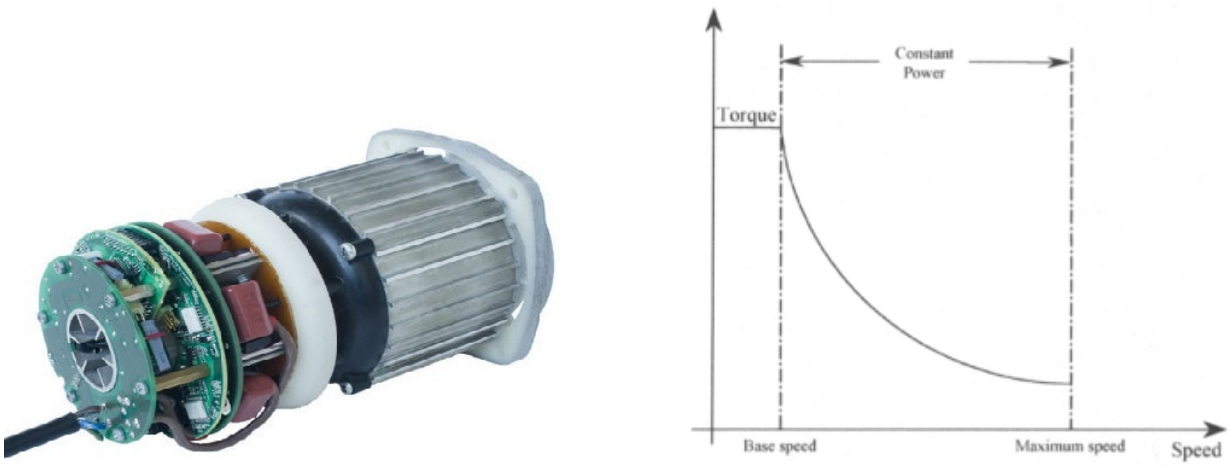

(a) A switched reluctance motor

(b) SRM torque-speed characteristic

Figure 1.5: A SRM with its characteristics [2]

1.3.4 Synchronous Reluctance motors

Synchronous reluctance motors (SynRM) represent a distinct category of synchronous motors, where the torque is generated by the disparity in magnetic conductivities along the quadrature and direct axis of the rotor. The difference in permeability of these two axes is determined through the incorporation of numerous flux barriers. The placement of the ends of the flux barriers, along with the deliberate rotor asymmetries, is carefully chosen to minimize torque ripple, primarily due to slot harmonics. [8] Notably, the rotor lacks field windings or permanent magnets. Currently, this type of motor is becoming very popular as an alternative to electric as well as hybrid vehicles due to its easy and strong construction, high efficiency, fast dynamic response and low cost[9]. The main advantages mainly depend on the non-existence of rotor cage losses by allowing a higher permanent torque than the torque of an induction motor, for example, of the same size. Considering the requirements for high torque and power density, this machine is still under research for traction applications.

1.3.5 Permanent magnet synchronous motors

Brushless permanent magnet motors are a type of motor that combines the features of permanent magnet technology and brushless design. They encompass permanent magnet synchronous motors (PMSM) and brushless DC (BLDC) motors. The distinction criterion between these two motors lies in the formation of current and electromotive force waveforms.

The name of the permanent magnet synchronous motor derives from the permanent magnets that are mounted on the motor's rotor. They are operated with sinusoidal current and sinusoidal electromotive force waveform. In a closed-loop control system, a resolver is employed to detect the rotor's position. PMSMs stand out as a formidable competitor to induction motors in traction applications, since numerous car manufacturers, including Toyota, Nissan and Honda, have already adopted them for their vehicles. They are renowned for their simple structure, compact size, lightweight design, reliability, low inertia and fast response. In addition, there are other benefits, such as high efficiency, high power density, high power factor and an improved dispersion of heat into the environment.[10] The core of the design of a PMSM lies in the arrangement of the permanent magnets in the rotor. Changing the configuration of the permanent magnets in the rotor significantly affects the performance of the motor. A well-designed structure not only enhances torque density, efficiency and temperature control but also optimizes material utilization and reduces production costs.

The torque-speed relationship is illustrated in the graph of Figure 1.6a. These motors operate in the constant torque region at medium speeds and transition to the constant power region at high speeds. As can be seen, the constant power region is narrow. This region can be widened and the efficiency of the motor can be improved by adjusting the conduction angle of the power converter at speeds higher than the base speed. The torque-speed characteristic of a PMSM under conduction angle control is depicted in Figure 1.6b. Generally, an increase in conduction angle results in higher torque output. In the constant torque region where a longer duration of current conduction leads to an increased time of torque generation. Furthermore, the conduction angle allows for control over the power factor of the motor, with larger angles leading to a more improved power factor, and also affects the speed regulation. Speed range can be extended three to four times the base speed.

Regarding the disadvantages of PMSMs, these include the high price of the permanent magnets, which affects the overall manufacturing cost of the motor, as well as the sensitivity of the magnets to high temperatures. Another effect called demagnetization [11], during which the magnetic properties of the magnets are reduced or eliminated, may occur due to heat or armature reaction. In general, faults that occur during operation are usually irreversible and pose significant challenges in terms of detection, making prevention nearly impossible.

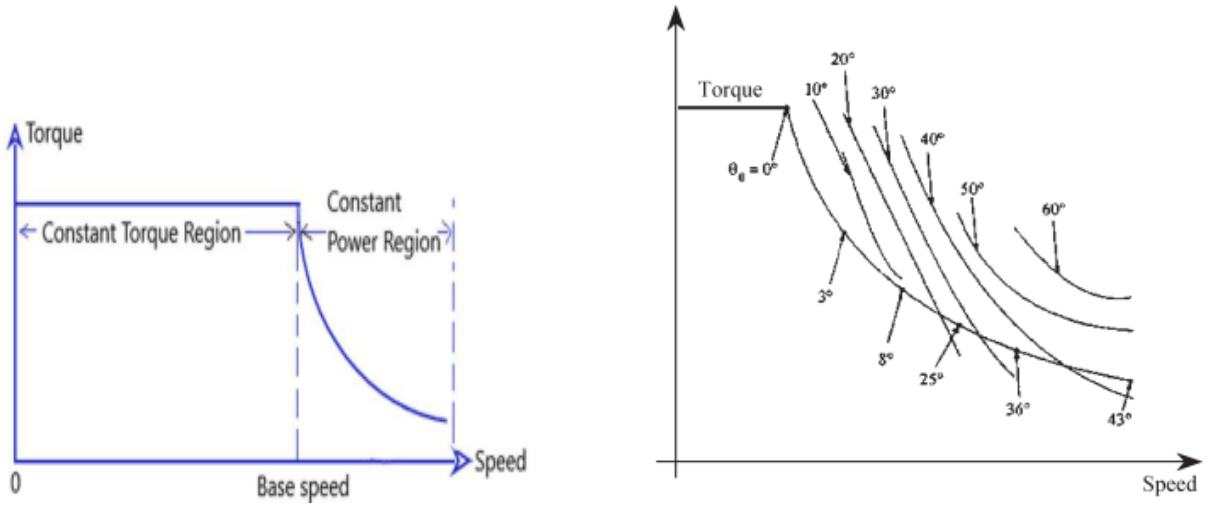

(a) Torque-speed conventional characteristic of PMSM [3]

(b) Torque-speed characteristic under conduction angle control [2]

Figure 1.6: PMSM characteristics before and after control

1.3.6 Brush-less DC motors

Brushless direct current (BLDC) motors are essentially the result of reversing the rotor with the stator in permanent magnet motors. In contrast to PMSMs, they are operated with square waves of current and trapezoidal electromotive force[12]. Unlike brushed DC motors, BLDC motors operate without brushes. Instead, they use an electronic commutation through a controller. The absence of brushes reduces friction and wear, resulting in lower maintenance requirements, costs and great reliability. The electronic commutation is achieved with a sensor. Sensors, such as Hall effect sensors, provide feedback to the motor controller, allowing precise control of the rotor position and commutation timing. These motors belong to permanent magnet motors, as they incorporate permanent magnets in the rotor that interact with the stator's magnetic field to produce rotational motion. This design contributes to high power density. They are more compact and lightweight than their brushed counterparts with similar power ratings, making them more appropriate for applications where volume and space become critical considerations.

Also, the absence of brushes and electronic commutation reduces friction and wear, which leads to better efficiency, as there are no rotor windings or rotor copper losses. Beyond that, they allow for smooth and quiet operation and precise control over speed and torque, as noise levels are minimized.

They present a similar torque-speed characteristic to PMSMs. They have high starting torque and their efficiency can reach up to 95-98%. The disadvantages are the short constant power range, the decrease in torque as speed increases after the base speed and the high production cost due to permanent magnets. In Figure 1.7(a), it can be seen for BLDC motors, by analogy with PMSMs, that through flux weakening or conduction angle control, the constant power region can be widened when the vehicle shifts to high speeds. As the angle increases, so does output torque and the speed range. In Figure 1.7(b), it is shown that a PMSM has a higher torque than the BLDC motor with a two-phase 120°conduction. BLDC motor with a three-phase 180°conduction has higher speed with lower torque[13].

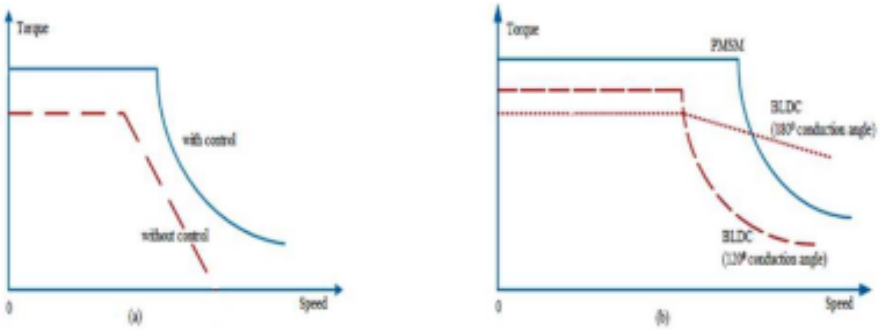

Figure 1.7: Torque-speed characteristic of BLDC: (a)Motor's control strategy (b)PMSM and BLDC conduction angle control [3]

1.3.7 Comparison between the different types of motors

Based on the descriptions of the electric motor categories analyzed in the previous subsections, some comments and conclusions can be drawn. The electric propulsion systems are evaluated based on six key factors: power density, efficiency, controllability, reliability, cost and technological maturity. A score out of 10 has been given in each of DC motors, IM, PM motors and SRM in Table 1.1.

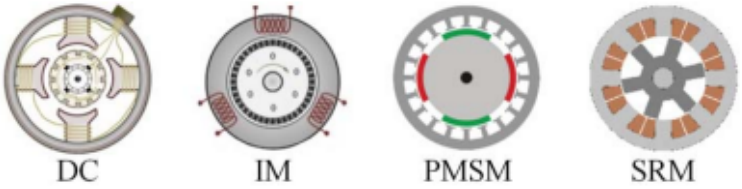

Figure 1.8: The four electric motors for comparison [6]

According to the observations of Table 1.1, induction motors and permanent magnet motors in general are more suitable for traction applications considering all of these parameters. PM motors have the highest rating for both power density due to the presence of the magnets and efficiency due to the absence of rotor winding losses. DC and induction motors are rated highest in terms of controllability, as DC motors can be controlled very simply, while IMs can be easily controlled through a vector control system and their flux and torque can be easily decoupled as well. The induction motor, also, is the most reliable due to its robustness and rigid construction.

Electric motor features	DC Motor	Induction motor	PM motor	SRM
Efficiency	5	7	10	7
Power density	5	7	10	7
Controllability	10	10	8	6
Cost	8	10	6	8
Reliability	6	10	8	10
Technological maturity	10	10	8	8
Total sum	44	54	50	46

Table 1.1: Evaluation of the four motor types

Other characteristics can be used as criteria for the electric propulsion system selection. Among them, the weight and efficiency (in percentage) of the aforementioned four types are compared in Tables 1.2 and 1.3 respectively[14].

Motor types	Motor itself	Motor with electronics
PM motor	100	200
SRM	150	250
Induction motor	200	300
DC motor	400	450

Table 1.2: Comparison of the Weight (With basis set on PM=100)

Motor types	Motor itself	Electronics	Motor with electronics
DC motor	80	98	78
Induction motor	90	93	84
PM motor	97	93	90
SRM	94	90	85

Table 1.3: Comparison of efficiency in percentage (%)

The tables confirm what has already been mentioned, in traction applications where weight is considered critical, permanent magnet motors are the more suitable option, followed by switched reluctance motors, then by induction motors, while DC motors are the worst possible option. PM motors are also the most efficient not only for the motor but for the entire unit consisting of the motor drive and the electronics. These units in SRM and IM are very close in efficiency, while the DC motor unit has the lowest value of all.

Below is a graph illustrating the percentage of occurrences of torque ripples for the four electric motor types of Figure 1.8. It can be easily observed that the highest level of occurrences is in the case of SRM, while the least occurrences occur in the case of induction motors.

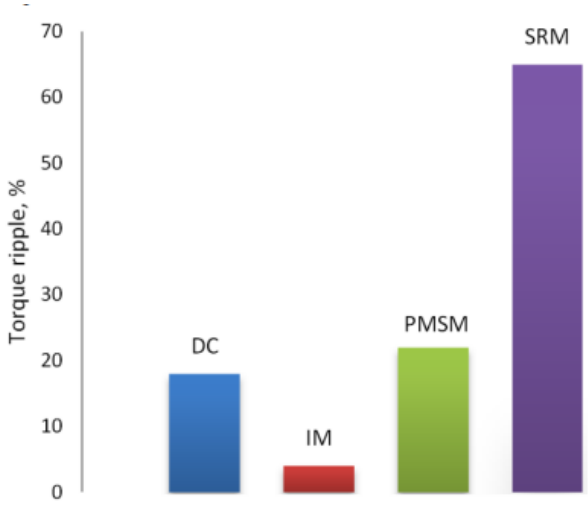

Figure 1.9: Comparison between DC, IM, PMSM and SRM, based on torque ripples [6]

1.4 Topologies of permanent magnet motors

This section highlights the features of various permanent magnet motor structures. Because of the multitude of options, it is not feasible to conduct a comprehensive analysis of all of them. Instead, the analysis focuses on the most prevalent structures.

There are two key topologies based on the orientation of the magnetic flux within the motor. These topologies are the radial flux and the axial flux permanent magnet motor. There is a cross-sectional view of them in Figure 1.10, where the direction of the magnetic flux in each case can be visualized with the red arrow. There can be a further classification depending on whether the rotor is inside of the stator or not, or whether the placement of the magnets is on the surface of the rotor or in the interior of it. Different characteristics and mathematical expressions of the basic electrical quantities appear for each topology.

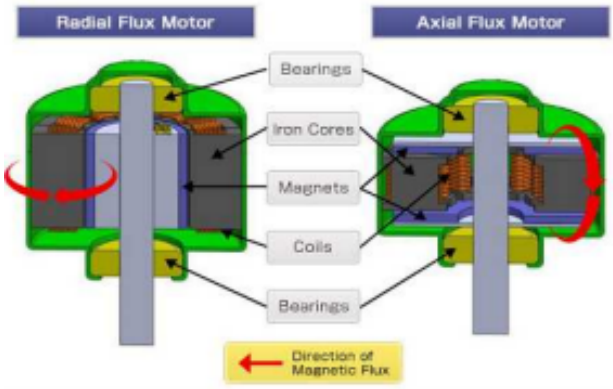

Figure 1.10: Cross-section of a radial flux and an axial flux motor [15]

1.4.1 Mathematical modeling of PM motors

First, the mathematical modeling of the permanent magnet synchronous motors will be discussed, listing some of the basic equations for voltage, current, torque and maximum speed. Field-oriented control (FOC) for PMSM is a widely used algorithm, that aims to control the stator current, as these are defined as two orthogonal components that can be visualized with vectors. FOC includes techniques, like field weakening (FW) and maximum torque per ampere (MTPA)[16]. The former refers to reducing flux linkage to limit motor voltage to the

rated value, thereby increasing the speed, while the latter ensures the desired torque level is achieved with the minimum current for the stator windings. The expressions for direct axis and quadrature axis stator voltage related to stator current are respectively:

$$V_{ds} = R_s \cdot i_{ds} + L_d \cdot \frac{di_{ds}}{dt} - \omega_r \cdot L_q \cdot i_{qs} \tag{1.1}$$

$$V_{qs} = R_s \cdot i_{qs} + L_q \cdot \frac{di_{qs}}{dt} - \omega_r \cdot (L_d \cdot i_{ds} + \lambda_m) \tag{1.2}$$

The electrical quantities are defined in the following table 1.4. Under steady-state conditions, the electrical angular velocity is presumed to remain constant and equal to the synchronous speed. Any variation in current is disregarded, so the derivative $\frac{di_{ds}}{dt}$. Consequently, the steady-state equations for the voltage can be determined as:

$$V_{ds} = R_s \cdot i_{ds} + L_d \cdot \frac{di_{ds}}{dt} - \omega_r \cdot L_q \cdot i_{qs} \tag{1.3}$$

$$V_{qs} = R_s \cdot i_{qs} + L_q \cdot \frac{di_{qs}}{dt} - \omega_r \cdot (L_d \cdot i_{ds} + \lambda_m) \tag{1.4}$$

Electrical Quantities	**Description**	**Units**
i_{ds}	direct axis stator current	A (Ampere)
i_{qs}	quadrature axis stator current	A (Ampere)
R_s	stator winding resistance	Ω (Ohm)
L_d	direct axis stator winding inductance	H (Henry)
L_q	quadrature axis stator winding inductance	H (Henry)
λ_m	flux linkage of PM rotor	Wb (Weber)
ω_r	rotor angular speed	r/s (radians per second)

Table 1.4: The electrical quantities of the aforementioned expressions

Various factors contribute to the overall torque behavior of a PMSM. Among them, cogging torque is defined as the torque produced due to the interaction between the permanent magnets in the rotor and the slots of the stator. Because the magnets are attracted to the stator teeth, the torque required to rotate the rotor changes in proportion to the relative position of the rotor to the stator. Minimizing cogging torque is critical for achieving smooth and consistent motor operation. The electromagnetic torque is considered the primary torque that drives the rotation of the motor. It is generated by the interaction between the rotor and stator magnetic fields. It is essential for efficient motor operation to ensure a high and stable electromagnetic torque. The equation which describes this kind of torque is the following:

$$T = \frac{3}{2} \cdot P \cdot (\lambda_m \cdot i_{qs} + \frac{1}{2} \cdot (L_d - L_q) \cdot i_{ds} \cdot i_{qs}) \tag{1.5}$$

where P is the number of pole pairs

1.4.2 Radial flux motors

Radial flux motors are a distinctive class of PMSM characterized by their structural arrangement. In this type of motor, the magnetic field is perpendicular to the rotational axis of the shaft and the current travels radially. Their key feature is the cylindrical or annular design with the magnetic flux moving outward from the center to the periphery. While these motors require enough space for installation due to their large size, this radial configuration allows for

a relatively shorter axial length and efficient heat dissipation. Their topologies can be primarily distinguished as outer rotor and inner rotor topologies[17].

In outer or external rotor radial flux PM (ERPM) motors the rotor spins outside the stator, as the stator is fixed inside the rotor. The magnets are mounted on the inner surface of the rotor bonded in place. An example of this topology is provided in Figure 1.11, showing the rotating part (rotor) on the left covering the stationary part (stator) on the right. Due to the outward orientation of stator teeth, winding this motor is a comparatively simple process. The external placement of the windings facilitates efficient heat dissipation. They provide more torque when compared to inner rotor motors due to the improved mechanical advantage offered by the rotor-stator configuration of the active magnetic surface, which results in larger air gaps. Thus, the ohmic losses of the stator windings can be dissipated. The primary drawback lies in the challenge of cooling the motor. Inner rotor motors benefit from a well-established thermal pathway extending from the stator to the motor housing. However, in external rotor motors, there is an absence of a direct thermal pathway which poses difficulties in applying liquid cooling solutions.

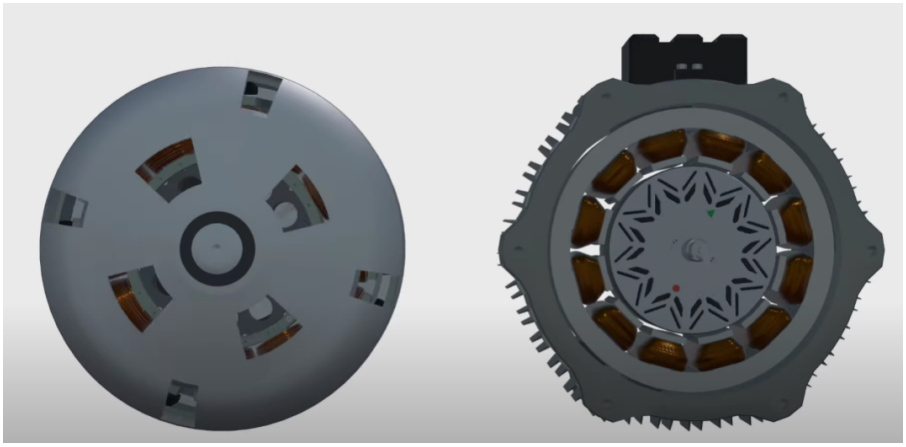

Figure 1.11: ERPM motor

In inner or interior rotor radial flux motors, the rotor is located and spins inside the stator. They include two main categories, based on the placement of the permanent magnets in the rotor. These categories are depicted in Figure 1.12:

- Surface-mounted PMSM
- Interior PMSM

Figure 1.12: Cross section of a SPM(left) and IPM motor (right)

1.4.3 Surface-mounted permanent magnets

Surface-mounted permanent magnet (SPM) motors are a topology in which the permanent magnets are mounted to the surface of the rotor, typically bonded in place [18]. They are held in place with composite tape or manufactured as a ring wrapped around the rotor. The torque is generated directly by the reaction between the magnetic field of the magnets and the field generated in the stator teeth by the windings. As a result, the magnetic field from the magnets acts directly on the air gap leading to minimal rotor losses. They exhibit high efficiency as well as viable options for high-speed applications. In SPM motors, the inductance in both axes d and q are almost equal. Thus, the ratio of q-axis inductance to d-axis inductance, which is defined as saliency ratio SR ≈ 1. Then, the direct current component i_{ds} equals zero as it does not contribute to the overall torque, but it does to copper losses [19]. Thereby, the torque equation at (5) depends only on the i_{qs} component, which has the rated current value. Torque becomes maximum when the stator current vector lies over the q axis and it can be written as:

$$T_{max} = \frac{3}{2} \cdot P \cdot \lambda_m \cdot I_{qs} \tag{1.6}$$

The main disadvantage of that topology is the high proportion of the magnetic material for torque generation of the motor, as they lack reluctance torque. That leads to increased manufacturing expenses. In addition, their structure and shape cause them to be mechanically weaker than IPM motors, as their large rotor can act as a flywheel because of the high moment of inertia.

1.4.4 Interior permanent magnets

The other category based on the assembly of the magnets is the interior permanent magnet (IPM) motor. In this type of motor, the permanent magnets are placed in the inner part of the rotor. In particular, simple bar magnets, slotted or molded into punched holes, sit inside a rotor core manufactured from a stack of laminated steel sheets[20]. The magnets are mechanically located in the slots, removing the need for any banding. In contrast to SPM motors, they typically use less magnetic material, reducing costs. IPM motors are characterized by their inherent rotor saliency[21]. The mutual inductance of the two axes is not the same, varying with the rotor's position, as they are affected by its magnetic asymmetry. Consequently, reluctance torque is created that depends on the current of both axes. This torque is directly correlated with the applied current, as the higher the current applied the greater the torque output. Reluctance torque is added to the magnetic torque generated by the permanent magnets to enhance the magnetic field strength at the surface of the rotor. That is the main difference with SPM motors which only produce magnet-based torque. This improves the torque-to-magnetic material ratio, but it reduces peak efficiency under high torque. Torque is constrained by the motor's maximum current capacity, preventing overheating and breakdown when pushed to its limits in a short period. The equations that describe the limitations for both maximum current and voltage are respectively[22]:

$$(i_n)^2 \geq (i_{ds})^2 + (i_{qs})^2 \tag{1.7}$$

and

$$(V_n)^2 \geq (V_{ds})^2 + (V_{qs})^2 = (\omega_r \cdot L_d \cdot i_{ds})^2 + [\omega_r \cdot (L_q \cdot i_{qs} + \lambda_m)]^2 \tag{1.8}$$

The values for maximum current and maximum voltage must be the rated values to protect the motor from excessive current in short periods. In PMSM, flux weakening is applied so that a wider speed range can be achieved. The maximum speed is determined by the voltage limit in equation (8) when the current of the q axis i_{qs} is set to 0. At rated speed with maximum q-axis current, the motor can exceed this limit and achieve increased speeds. By applying a negative

current to the d axis and slightly reducing i_{qs}, the magnetic field in the d axis diminishes, leading to a decrease in electromotive force (EMF) and a slight increase in speed. The maximum speed of the motor is obtained when the total current is applied in the d axis and is equivalent to:

$$\omega_{r,max} = \frac{V_n}{L_d \cdot i_{ds} + \lambda_m} \tag{1.9}$$

The disadvantages of this topology are that, although no banding is required for the magnets, the assembly of the rotor can be complex due to the use of multiple layers of laminated steel and magnet arrays. In addition, IPMSMs may rely on rare earth magnets, especially those in high-performance applications. The availability and cost of these materials may be subject to market fluctuations and geopolitical factors, potentially affecting the viability of these motors.

1.4.5 Axial flux motors

The other main category is axial flux motors, where the magnetic flux direction is parallel to the rotational axis of the rotor and the current runs axially[15]. They are alternatively referred to as disc or pancake motors due to their shape. Their flat shape is justified by the fact that the active magnetic surface is the face of the rotor rather than its outside diameter. This allows an increased active magnetic surface area compared to a radial flux motor and typically improved performance in power-to-weight ratio and torque density. Similar to radial flux motors, there are several structural configurations, shown in Figure 1.13. The simplest and widely adopted one is the single stator single rotor setup, available as either internal stator external rotor, or external stator internal rotor. However, this design has a constrained capability for generating torque. Other designs are the double stator single rotor, where the two stators are on each side of the inner rotor, and the single stator double rotor, where the two rotors are outer on each side of the inner stator windings, enabling the motor to operate even if one of the windings fails. For increasing the torque, a multi-layer design can be implemented, which includes multiple rotors and stators.

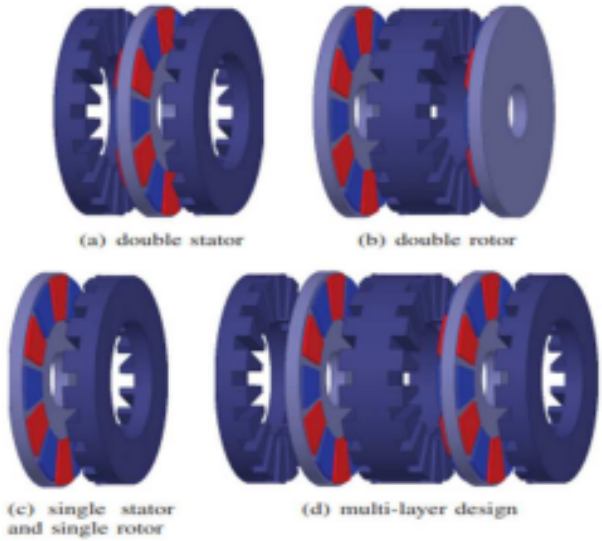

Figure 1.13: Different axial flux motor configurations [15]

1.4.6 Yokeless and segmented armature AFPM motors

One of the most promising as well as challenging types of axial flux motor seems to be the yokeless and segmented armature (YASA) topology. YASA topology represents an innovative

design within the realm of electric motors, offering unique features[23]. It combines the advantages of various other axial flux topologies. This type of motor architecture deviates from the conventional design by eliminating the traditional iron yoke found in the stator and adopting a segmented armature structure.

The YASA topology derives from the combination of two axial flux motors: the NS Torus-S and NN Torus-S, which are depicted in Figure 1.14. According to literature [24], NS Torus-S (lap) is characterized by its short stator yoke, which leads to increased power density and reduced losses. However, to generate torque, a lap winding must be employed. Consequently, the motor has a poor power fill factor and long-end windings which enlarge the outer diameter of the motor leading to reduced power density and increased losses. On the contrary, to manage the flux from both rotors, the NN Torus-S motor needs a large stator yoke. Thus, it presents high losses and reduced power density. However, a back-to-back winding with a high fill factor can mitigate this issue. This significantly decreases the prominence of the end windings, thereby enhancing the power density and efficiency of the NN Torus-S motor. Even though these two types present similar performance, the NS Torus has a slightly better power density and peak efficiency.

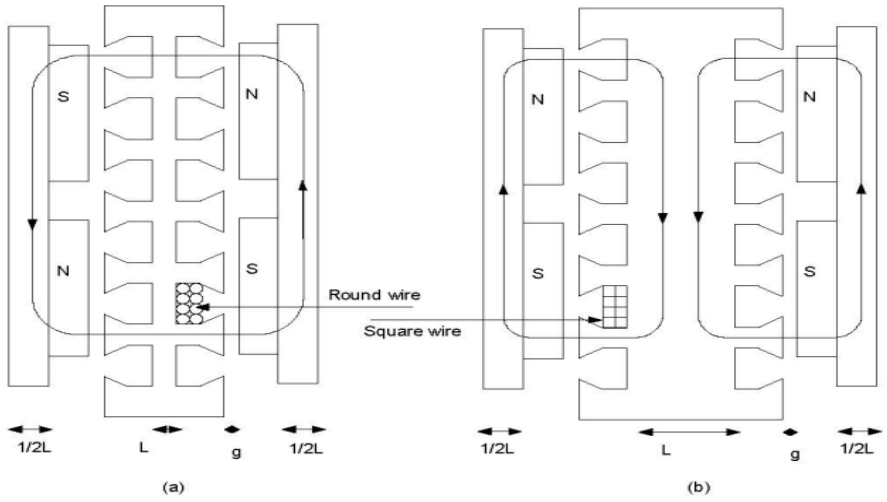

Figure 1.14: The NS torus-S (lap) and NN Torus-S motors [23]

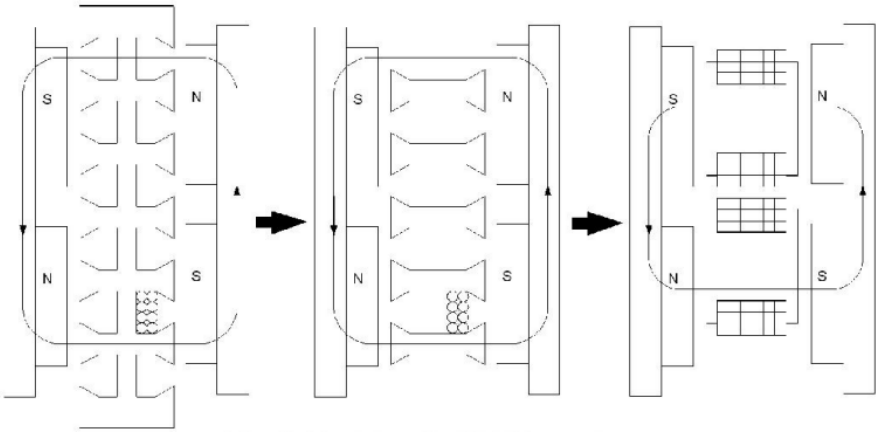

Figure 1.15: YASA topology derived [23]

The YASA topology is the result of combining the NS Torus-S motor with the NN Torus-S, by transforming the NS Torus-S topology. The aim was to adapt the benefits of these two types

to one motor type, primarily the exceptional winding characteristics of the NN Torus-S machine and the short stator yoke of the NS Torus-S. Figure 1.15 shows the manufacturing process from which the YASA topology is derived. The stator yoke of the NS Torus-S is removed since it is not necessary as the teeth become magnetically unconnected. The pitch of the teeth is enlarged to match the arc of the magnets and a single winding is wound around each of these magnets. The teeth and windings are bonded together with a high-strength material. Following the aforementioned process, a new topology has been created, forming an ideal design for electric vehicles.

As can be seen in Figure 1.16b YASA motor consists of two external rotors and an inner stator [25]. The yokeless configuration is distinguished by the removal of the bulky stator iron yoke. Instead, the stator consists of short-end windings in a disk-like formation. This design can dramatically reduce the iron in the stator by 50%. Therefore, it contributes to a more compact and lightweight solution, as the motor's overall volume and weight are reduced. The segmented armature enhances the motor's efficiency and performance. Instead of a continuous armature structure like traditional motors, in this topology, the armature is divided into magnet and coating segments, all forming the stator of the motor, allowing for more precise control of the magnetic flux. This segmentation contributes to a better magnetic field distribution, minimizing eddy current losses and improving overall efficiency, whose peak can reach up to 95-97%. The yokeless design also reduces core losses associated with the iron yoke. Furthermore, this topology results in a high fill factor, high power density and high torque density, which can be 20% higher than other axial flux motors [26],[27]. Last but not least, this topology presents an improved thermal performance. Heat dissipation is more effective due to the gaps between the stator segments. Thus, the motor is capable of handling higher power loads without compromising reliability.

The stator of a YASA motor, like this in Figure 1.16a, is made by pressing soft magnetic composite (SMC) materials. The components are bonded together and then wound to form the stator segments. It is composed of numerous minuscule surface-insulated iron particles. The stator includes three main subsystems: the part responsible for locating and securing the stator segments during operation, the liquid cooling system, which transfers the heat of the copper and iron losses to the water, preventing the stator from overheating and the electrical system that ensures even current distribution in the three phases, enabling compactness and robustness.

(a) A YASA motor

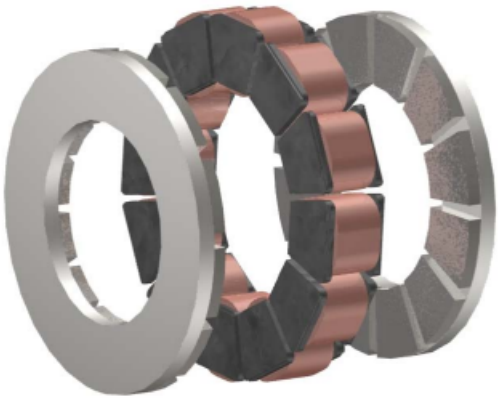

(b) The yokeless and segmented armature topology

Figure 1.16: A YASA axial flux motor and YASA topology [23]

The permanent magnets within the motor are divided into those with north-pole polarity and those with south-pole polarity. The primary magnetic flux in YASA motors, illustrated

in Figure 1.17, originates from the N(north)-pole permanent magnet and traverses the air gap, the stator core and the other air gap to reach the S(south)-pole on the opposite side[28]. After passing through the rotor core on the second side, the flux starts from the N-pole on the second side and traverses from the opposite, the air gap, the stator core and the other air gap to reach the S-pole on the initial side. The magnetic flux follows this path, forming a closed loop.

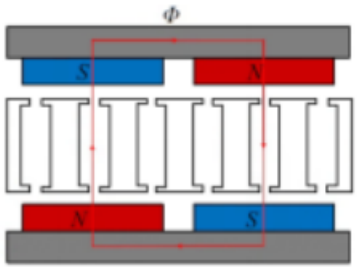

Figure 1.17: Magnetic flux path in a YASA motor [28]

In Figure 1.18, the YASA motor is shown with x, y, z axes defined as the circumferential, axial and radial directions respectively. Similar to other types of motors, it consists of a stationary and a rotating part. The former includes the stator core, supporting frame and armature windings, while the latter includes the rotor core, permanent magnets and the rotor housing. The shaft and bearings are part of the mechanism that holds the stationary and rotating parts together.

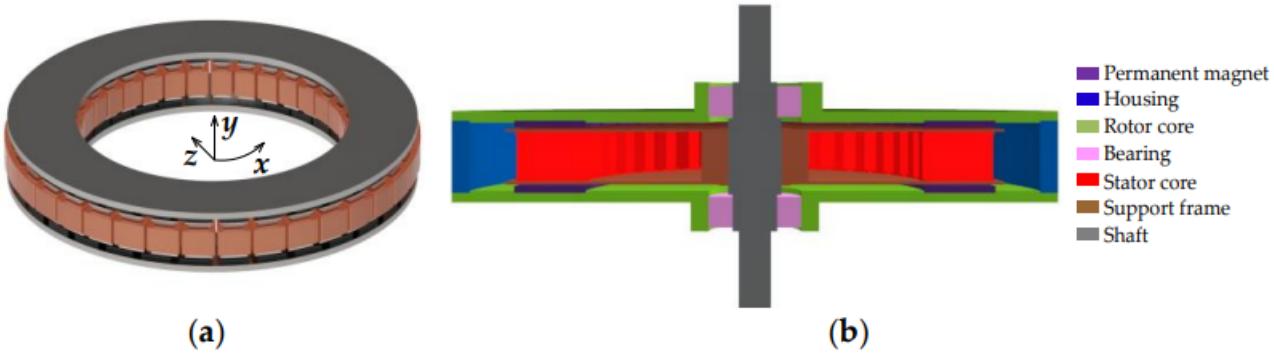

Figure 1.18: Structures of the YASA motor [28] (a)in 3D-field, (b)cross-section with its structural components

Although this configuration is the source of the aforementioned features, it also introduces a notable weakness. The mechanical construction of this motor type is still challenging, primarily due to the high axial force between the stator and the two rotors, which can further increase the asymmetrical air gaps.

2 Faults and diagnostics

While the characteristics and the operation of the main electric motor types have already been discussed, it is essential to highlight that traction motors are susceptible to various faults that can impact their operational reliability. These faults can be separated into stator and rotor faults. Typical cases are demagnetization, bearing failures, rotor eccentricity, broken rotor bars, insulation defects and stator windings faults[29]. Stator inter-turn faults are considered among the most critical faults as their fast evolution leads to a catastrophic breakdown[30]. These faults can have tremendous consequences, often requiring a vast amount of money for the machines in order to be repaired or to be replaced. Condition monitoring, where the machines are being monitored to prevent any failure, splits up into two subregions: the prognosis and the diagnosis[31]. The former is the scientific area that deals with the prediction of the faults before they occur, while the latter deals with the causes that lead to a fault, which has already occurred. Diagnostics are tools utilized for detecting early-stage defects, while the machine is still operating. Common diagnostic methods are stator current monitoring, vibration analysis, torque and magnetic flux monitoring and motor current signature analysis. This section provides a brief overview of the faults that typically occur in traction motors, especially in permanent magnet engines.

2.1 Faults

Faults are abnormal and undesired conditions or behaviors that occur in machines, leading to a potential malfunction, failure, or downgraded performance. In PM motors, faults can be divided into three main categories, according to the quantity they affect. These categories are: electrical faults, magnetic faults and mechanical faults[32]. Electrical faults include stator winding faults, such as open circuits or short circuits, magnetic faults include demagnetization of the magnets, while mechanical faults include bearing faults and rotor eccentricity. In induction motors, there could be another categorization based on the faults that occur in the stator, such as stator inter-turn winding faults, or the rotor, such as broken rotor bars. When these faults lead to total failure of the respective machine, the consequences are enormous. The most serious are the potential damage to people working at the infrastructure where the motor is installed as well as huge amounts of money for either the restoration or replacement of the machine.

There is a variety of reasons related to the appearance of faults in traction motors. Some examples are defects in the design or manufacturing process, harsh operating conditions, human factors such as wrong handling, insufficient maintenance and protection of the motor, or insulation degradation[33]. Referring to the first category, the manufacturing processes are not ideal, leading to inherent asymmetries in the magnetic field of the machines. In addition, during operation, motors are subjected to various stresses, known as TEAM (Thermal, Electrical, Ambient and Mechanical stresses) that degrade the overall motor performance.

2.1.1 Mechanical faults

Mechanical faults are defects that occur mainly in the mechanical design and structure of the motor. The most common defects that lead to motor failure are bearing faults, rotor eccentricity and mechanical imbalance.

- **Bearing faults:** Bearings are small rounded metal objects used to support and stabilize the rotor shaft[34]. They are placed in a perpendicular direction to the shaft, to prevent the rotor from falling due to gravity. Bearings play a crucial role in the smooth operation of the motor, as they enable the rotation of the shaft with minimal friction. The need for high-power applications thrusts the operating conditions of the bearings to

become harsher and harsher. Especially, bearings are subjected to fatigue, where cracks or small fractures are manifested in the bearings' components, ambient mechanical vibration, overloading, misalignment and corrosion due to improper installation or disassembly, contamination such as dirt, dust or moisture, current fluting and wrong lubrication. This poses challenges to their performance and reliability, often leading to failures[35]. Notably, bearings undergo inevitable fatigue, even under normal operating conditions. The fatigue crack begins beneath the metal surface and as it propagates to the surface, a metal fragment breaks away, leaving a small pit or flaking. This progression leads to bearing damage and eventual failure, including cage faults, inner race faults, outer race faults and ball faults. Bearing faults induce increased friction and heat generation between the bearings and the shaft, periodic intense vibrations and abnormal noise. The frequency of these vibrations is known as the rolling bearing fault vibration characteristic frequency and depends on different factors, such as the bearing geometry, the damage location and the rotational speed[36].

Bearing defects are among the most common faults, contributing to almost 40-50% of all motor faults, imposing the need for regular maintenance and timely replacements of worn components. Bearing faults can give rise to other types of faults, such as rotor eccentricity and inter-turn short circuits.

- **Mechanical imbalance:** During the manufacturing process of a PMSM, some components may not be assembled in their proper position. This leads to unbalanced loads or misalignments and therefore mechanical vibrations at high speeds, torque disturbances, wear and noise will be intensified[37]. Common examples of this kind of fault are an unbalanced rotor, a bent rotor shaft and misplaced magnets or bearings, due to uneven casting materials. Causing an unstable motor operation, mechanical imbalance results in a decrease in motor performance, accelerated wear of the components of the system and eventually a total failure of the system.

- **Rotor eccentricity:** Eccentricity is a type of mechanical fault that is caused by the imperfect inner circular surface of the stator or the incorrect positioning and mounting of the rotor inside the stator during assembly. Thus, the air gap between these two is uneven, causing serious consequences to the motor performance. More details about eccentricity are presented in subsection Eccenntricity.

2.1.2 Electrical faults

Electrical faults refer to the faults that affect the electrical properties of the system. The most common faults that affect all types of motors are stator windings defects[38]. These can be divided into Short-Circuit Faults (SCF) and Open-Circuit Faults(OCF). The former is highly detrimental and requires immediate action to deactivate the drive system, while the latter can continue without necessarily prompting a system shutdown. These include inter-turn or turn-to-turn short circuits, turn-to-ground, phase-to-phase, phase-to-ground short circuits and open circuits. As the last four faults lead to an immediate breakdown of the machine, the machine is automatically disconnected from the power supply by protective relays. In subsection **2.3** there is a further analysis of the stator inter-turn short circuits.

These faults are mainly caused by the damage to the insulation layer between the coil turns in the stator windings. The stator windings are coils of wire wound around the stator poles. These windings are connected to the motor's power supply and are responsible for creating the rotating magnetic field, necessary for motor operation when energized. The inter-turn short circuits are among the most common faults in all motor types and account for about 30% of the total cases in stator windings faults[39]. When the insulation layer between two adjacent

turns of the coil within the same winding breaks, then there is a direct contact between these two turns, leading to an inter-turn short circuit. If the insulation layer of the last turn of the coil or the inner area of the insulation breaks, this leads to direct contact between a turn and the ground, so the respective turn-to-ground short circuit occurs. A phase-to-phase short circuit occurs when two phases in a three-phase system are connected directly, bypassing the load or device. Thus, an asymmetry appears with the two phase currents being much larger than the phase current of the third phase. A phase-to-ground short circuit occurs when a phase of a three-phase system is directly connected to the ground. These direct connections in short circuits can lead to increased current flow, intense vibrations, overheating, and voltage and magnetic field imbalances. These imbalances can harm other electrical devices connected to the motor, such as inverters or motor drives. On the other hand, open circuits occur when there is a break in the stator winding, interrupting the continuity of the electrical circuit of the coils[40]. Hence, the flow of the electrical current through that portion of the winding is prevented and the magnetic field generated by that winding becomes incomplete and distorted. This can cause torque ripples, increased losses and an overall deficiency in motor performance. In summary, among the shortcomings of stator failures are undesirable torque ripples, intensified mechanical vibrations, undue stress on the inverter switches and the potential triggering of additional failures in other components of the electrical drive system.

A fault that is not associated with PMSM, but appears often in induction motors is broken rotor bars[41]. The severity of this fault varies, depending on the population of the broken bars. Structural and material defects in the manufacturing process or loose solder joints of rotor bars are common causes of broken bars. Additionally, during operation, the mechanical load of the rotor can be high and the high current flowing through the bars can lead to excessive temperatures. The rotor is most stressed under steady-state conditions, where the mechanical forces acting on the rotor are at their peak, while the rotor current can reach five times the steady-state current. Skin effect also occurs, which is defined as the tendency of the high alternating frequency currents to crowd towards the surface area of the bars. The top surface of the bars is more thermally stressed than the bottom of the bars, making them more susceptible to underlying cracks and holes. When this rotor fault occurs, it can have negative effects on motor performance. The motor may not be able to start, but even if the severity of the fault is low and the motor starts to run, it can shut off suddenly. Moreover, it causes asymmetrical magnetic forces. Under healthy operation only the supply frequency is present. When a bar breaks, a new frequency is created opposite to the direction of the main rotor magnetic field sf_s, where s is the slip. The broken bar fault induces a voltage to the stator windings with frequency $(1-2s)\cdot f_s$. Due to the broken bar, the rotor loses its symmetry with an additional frequency component $(1\pm 2s)\cdot f_s$ emerging in the magnetic flux, which results in the generation of harmonics of the same frequency in the stator current signal. Subsequently, these harmonics consistently generate new harmonics with frequency $(1\pm 4s)\cdot f_s$. Following this principle, the characteristic frequency generated by the broken roto bar in the stator current is represented as:

$$f_{brb} = (1 \pm 2ks)\cdot f_s, \quad k = 1, 2, 3, \ldots \tag{2.1}$$

It is important to note that when a rotor bar breaks, then the next ones most likely to break are exactly the adjacent bars to the broken bar, as they are the most affected by the current and load asymmetry.

2.1.3 Magnetic faults

This is a unique class of faults owned solely by PMSM due to the existence of permanent magnets. A very common fault that belongs in this category is demagnetization. Demagnetization[42] is defined as the reduction or complete loss of the magnetic properties from the permanent

magnets. It can be distinguished into local demagnetization, where only specific regions of the material are affected and uniform demagnetization which occurs consistently across the entire material due to external factors affecting the material as a whole.

The functionality of permanent magnets lies in the alignment of micro-regions, called domains, within an alloyed material. Each of them acts like a tiny magnet within the larger whole. The domains are made up of strong magnetic materials, such as neodymium-iron, samarium-cobalt or strontium-iron also known as ferrites. The process of magnetization includes exposing these materials to a strong magnetic field. In the beginning, the domains are randomly oriented towards all directions. Eventually, they start to align with the direction of the magnetic field and when almost all of them are aligned in the same direction, the material has transformed into a permanent magnet. When demagnetization occurs, the magnetic domains lose their complete alignment. The magnetic properties of a material rely on that alignment, so a disruption in the magnetic field and consequently to the domain alignment leads to the decrease of the magnetic properties of the magnet.

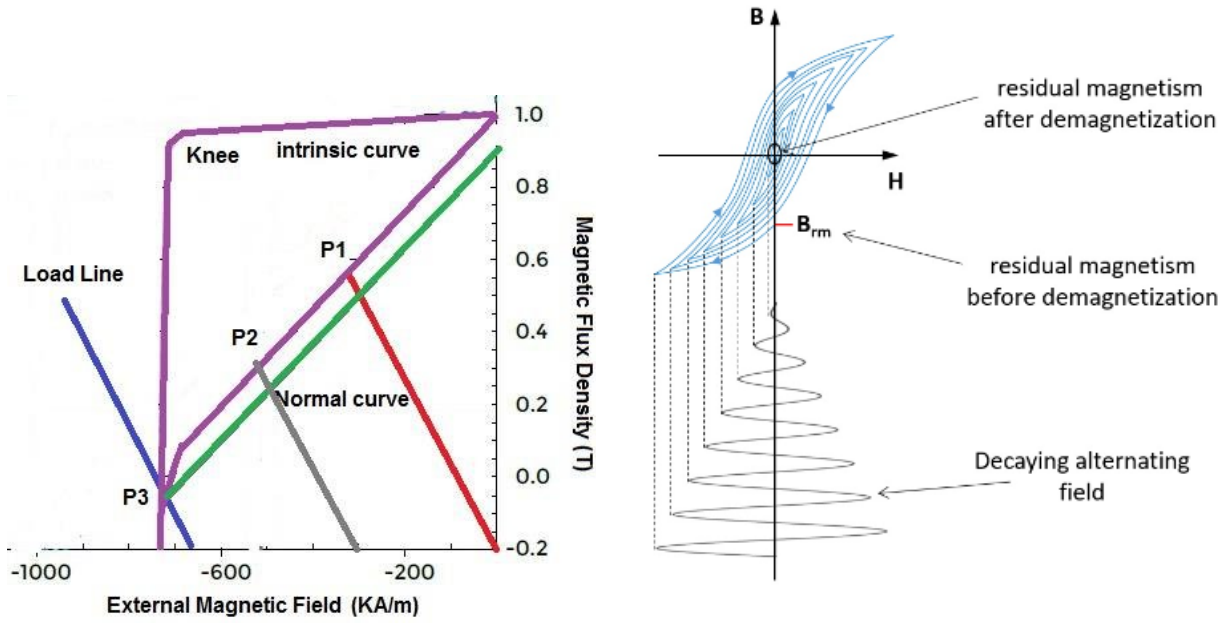

(a) Demagnetization graphically explained (b) B - H figure

Figure 2.1: Demagnetization fundamentals [43]

In essence, during demagnetization, the magnets are exposed to an opposing magnetic field. The characteristic in Figure 2.1a [43] will explain how demagnetization of the permanent magnets works. The B-H curve (magnetic flux density(T) versus magnetic field strength(A/m)) represents graphically how the magnetism of a material responds to applied magnetic field strength. The red line reaching point P1 illustrates how a magnet works without the presence of an external magnetic field. When it is exposed to an external demagnetization field, opposite to the direction of the magnet's field, the operating line shifts to the left. The knee point is the threshold in the B-H curve, which determines whether a material can retain its magnetic properties or not. Above the knee point, the material behaves differently than below it. If the magnet operates at point P2, which is located above the knee point, the material can recover its residual flux density and therefore its original magnetic properties, upon removal of the external magnetic field. This recovery is known as reversible demagnetization. In contrast, if the shift in the load line positions the operating point at P3, located below the knee point, the magnet will be unable to recover its residual magnetic flux density. Upon the removal of the

external field, the material will undergo irreversible demagnetization[44], meaning that it may not fully recover its original magnetic properties. Instead, it will follow a new path, known as the recoil line. Figure 2.1b illustrates how the residual magnetism of a given magnetic material reverts after irreversible demagnetization, while the alternating field decays. The slope between these lines is similar, but each time the magnetic flux density becomes smaller and smaller until it reaches zero values when the field is totally removed.

Certain factors affect the magnetized materials including heat, high pressure, collision with other objects, armature reaction, volume loss and conflicting magnetic fields[45]. First and foremost, temperature plays a critical role in the emergence of this fault. An increase in temperature leads to an increase in atomic movement, which eventually overcomes the alignment of the electrons. The threshold above which a magnet irreversibly loses its permanent magnetic properties is named Curie Temperature (TC). Above this temperature, a ferromagnetic material transforms to paramagnetic. Nevertheless, demagnetization can occur at some levels before the magnet's temperature reaches the Curie point. The extent of this fault is highly dependent on the specific material and grade of the magnet used. Some permanent magnet materials are more susceptible than others to demagnetization as temperature increases. The most susceptible are the neodymium magnets with TC approximately at 100°C, an alloy of neodymium, iron and boron to form $Nd_2Fe_{14}B$ tetragonal crystalline structure. They are the most widely used type of rare-earth magnets. Other choices are the samarium cobalt magnets with TC at 350°C and alnico magnets with TC at 540°C being the best choice for continuous extreme temperatures.

The impact of different temperature conditions on the demagnetization of NdFeB Neorem 593A is shown in Figure 2.2. Because of the negative thermal coefficient coercive force, the magnet is more likely to be demagnetized as the temperature increases. Below 150°C, the knee point does not fall into the second quadrant of the B-H characteristic, indicating no risk of demagnetization. However, as the temperature increases, the knee point appears on the demagnetization curve, raising the risk of demagnetization.

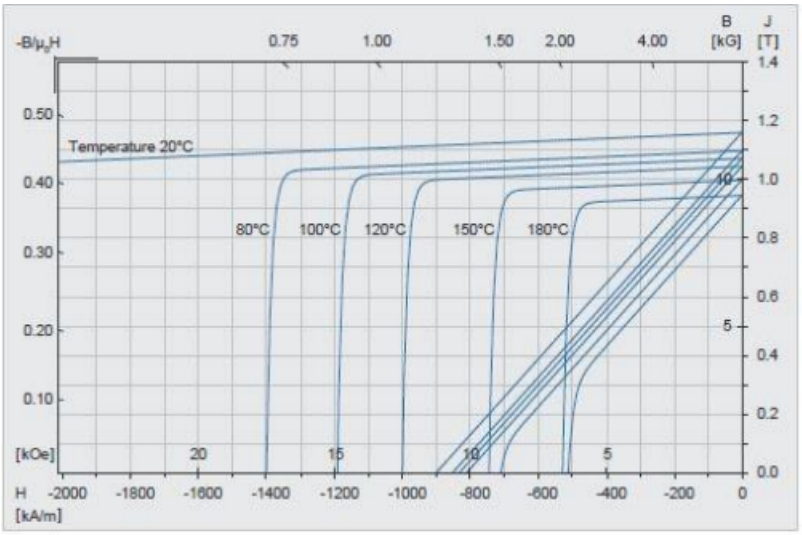

Figure 2.2: Demagnetization curve for a certain magnetic material (NdFeB) under different temperatures [43]

Another factor that can demagnetize a permanent magnet is collision with other objects, like hammering. This will disrupt the motion of the atoms and have an impact on the alignment of the north and south poles of the magnet, leading eventually to the loss of its magnetic properties. Furthermore, it can affect the physical integrity of the magnet resulting in loss of volume. Other phenomena caused by excess humidity, such as erosion or oxidation, can harm

the physical properties of the permanent magnet.

Last but not least, external magnetic force fields can demagnetize a permanent magnet. The existence of another magnetic field around the magnet can act as a demagnetizing force. The interaction between the stator windings field and the permanent magnets can lead to magnetic field distortions similar to the effects seen due to armature reaction[46] in DC machines. Armature reaction is the shift in the magnetic axis created by the distortion of the magnetic field produced by the field pole winding by that of the armature winding.

As it was referred to, PM motors are affected when operating at high temperatures. One way to reduce the risk of demagnetizing the magnets is for the motor to work at lower temperatures, but this would limit their applications. The use of magnetic materials with high magnetic field strength is an alternative but this would result in increased costs. Recent research has provided other options with the effects of the $d-$ and $q-$ axis currents[47]. While an increase in the $d-$ axis current increases the possibility of demagnetization, an increase in the $q-$ axis current, under a constant input current, leads to increased demagnetization tolerance, but decreased motor torque density. If appropriate control strategies are utilized the risk of this fault can be significantly reduced.

2.2 Eccentricity

Eccentricity is defined as a fault or condition where the motor's air gap is uneven between the rotor and the stator[48]. A substantial escalation in the severity of eccentricity can lead to friction between the rotor and the stator, causing severe and potentially irreparable damage to the motor. Eccentricity typically refers to the misalignment between the rotor's center with the stator's center. In a healthy machine, assuming that the center of the stator lies on one axis and the center of the rotor lies on another axis, these two axes are coincident[49], as shown in Figure 2.3(a). This misalignment can occur due to design and manufacturing defects, installation issues, or defective operating conditions and can have adverse effects on the performance of the machine. Some usual factors that cause eccentricity include the bearing fault, where the rotor is displaced inside the stator, a bent rotor shaft, imperfect cylindrical shapes of the stator bore and rotor face, bearing wear, or mechanical resonance at critical speeds.

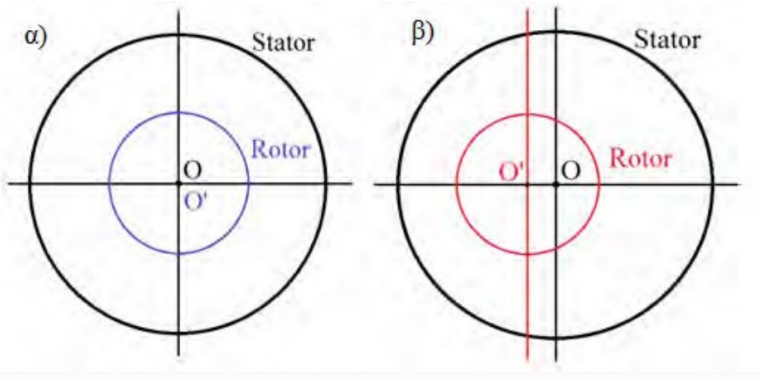

Figure 2.3: Cross section of a motor: (a)Healthy state, (b)With eccentricity [49]

There are two types of eccentricity, referred to as static and dynamic eccentricity, while a combination of them can occur as well[50]. Static eccentricity occurs when the geometric centers of the stator and the rotor no longer coincide, although the rotation and geometric centers of the rotor still align. On the other hand, dynamic eccentricity occurs when the geometric center of the rotor deviates from the rotation center, but the geometric center of the stator is aligned with the rotation center of the rotor. Mixed eccentricity is the case when a combination of the

characteristics of these two types occurs. The rotation center of the rotor does not coincide with either the geometric center of the stator or the geometric center of the rotor. Instead, it rotates around a new, separate axis resulting in a new time-varying asymmetry in the air gap. The three eccentricity types are illustrated in Figure 2.4.

In Permanent Magnet Motors, when eccentricity occurs part of the stator is closest to the permanent magnets of the rotor[51]. This generates an attractive force that acts on the rotor and consequently, asymmetric magnetic forces are generated between the rotor and stator. These forces pose a significant concern as they contribute to high levels of noise and vibration, accelerating the aging of the motor. Thus, increased wear and tear on the components are required, affecting the overall system's reliability. In addition, this uneven air gap leads to torque ripples, variations in magnetic flux density and increased losses in the motor, reducing the motor efficiency and potentially leading to higher operating temperatures. Research has shown that eccentricity affects differently the SPM and IPM motors. It has a stronger impact on the magnetic gap induction of the IPM motors. In SPM machines, magnetic asymmetric forces increase linearly, affected by the relatively smaller air gap. In contrast, in IPM machines, these forces increase significantly and non-linearly owing to the increased effect of core saturation.

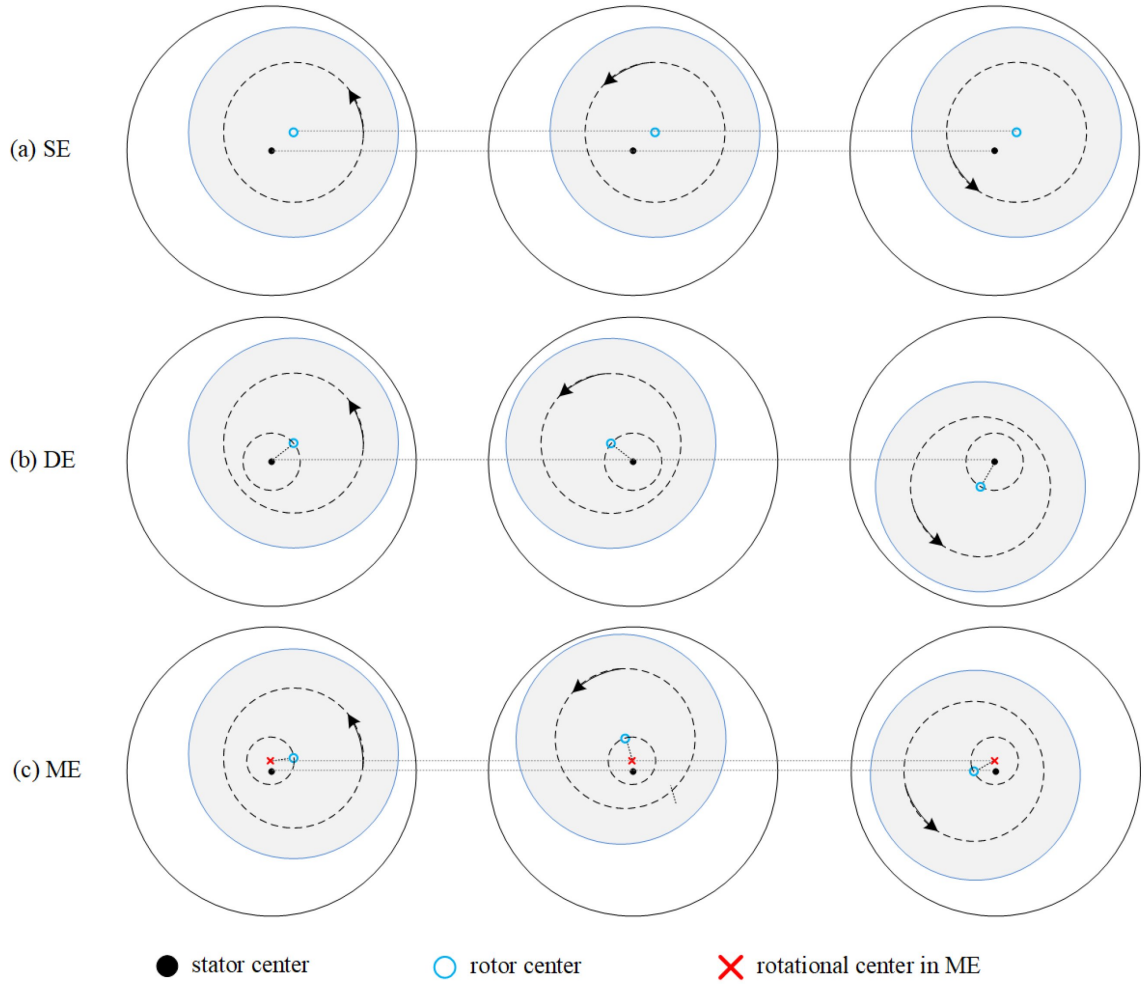

Figure 2.4: The eccentricity types [50]

The formula for detecting static, dynamic and mixed eccentricity for PM machines is:

$$f_{ecc,_{PM}} = (1 \pm \frac{2k-1}{p}) \cdot f_s \tag{2.2}$$

where k: an integer, p: the pole pairs, f_s: the supply frequency and f_{ecc}: the harmonic frequency of the eccentricity

This formula, based on the appearance of harmonics in the rotor current spectrum, in the general case for detecting only static or dynamic eccentricity applicable to induction motors is:

$$f_{ecc,1} = [(R \pm n_d) \cdot (\frac{1-s}{p}) \pm 2n_{sa} + n_{ws}] \cdot f_s \tag{2.3}$$

where R: the rotor bar number, n_d=0 for static eccentricity and ± 1,±2,±3,... for dynamic eccentricity, $n_{sa} = 0$ with no saturation, s: the slip and n_{ws} = ±1,±3,±5,... the harmonic order of the stator windings
For mixed eccentricity in induction motors, this formula becomes:

$$f_{ecc,2} = [f_s \pm k \cdot f_r] \tag{2.4}$$

where k=±1,±2,±3,... and $f_r = (\frac{1-s}{p}) \cdot f_s$ = the rotor frequency

2.3 Inter-turn faults

The turns of the coils in the stator windings are not in direct contact between them, as this would result in short circuits and subsequently failures in windings. Insulation layers are used between the turns of the coils to protect them from electrical faults. All poles of all types of traction motors are insulated and the insulation material differs depending on the application. The requirements for delivering high power and torque density and poor operating conditions are critical factors for stresses to the insulation layer[52]. The insulation is subjected to a group of stresses known as TEAM, which stands for Thermal, Electrical, Ambient and Mechanical stress. Particularly, the insulation undergoes simultaneously two or more of these stresses including high temperatures, high currents and mechanical vibrations. A turn-to-turn or more commonly known as an inter-turn short circuit (ITSC) is a short circuit that occurs between two adjacent turns within the same stator winding.

As shown in Figure 2.5a, when an inter-turn fault occurs, a closed circuit in one phase of the stator windings is created[53]. The stator winding R_α is divided into two parts: normal and faulty, while R_f is the short circuit resistance and i_f is the short circuit current. Due to the rotating magnetic field, voltage is induced in the short-circuited coils as described by Faraday's law of induction and current starts to flow in the closed circuit of the short circuit. The short circuit current is much higher than the stator current, even if the severity of the fault is low. As the fault is not addressed promptly, the rise in current in the closed circuit will result in local overheating of the coil. Consequently, this overheating can damage the insulation layer of the adjacent coil, causing the number of short-circuit turns to progressively increase. Due to overheating, this fault actually burns the coils causing black spots on the surface of them.

An inter-turn short circuit can be detected by analyzing the signal of the stator current. The stator windings are no longer symmetrical with the occurrence of this fault leading to unbalances in voltage and current. The amplitude of the short current depends on various factors, such as the number of short-circuited turns, the synchronous speed and the amplitude of the magnetic flux density. The fault appears in characteristic frequencies in the stator current signal spectrum, described by:

$$f_{sc} = f_s \cdot [k \pm \frac{n}{p}(1-s)] \qquad where \;\; k = 2m-1, (m \in N+) \;\; and \;\; n \in N+ \tag{2.5}$$

It has been extracted experimentally that the origin of the stator winding failure often originates as an unnoticed inter-turn short circuit fault in a coil, which has the potential to evolve into a phase-to-phase or ground short circuit fault very fast, resulting in high motor temperatures and additional irreversible demagnetization of the magnets. Therefore, it is essential to assess the ITSC fault characteristics in PMSM to provide early detection of stator winding issues and prevent catastrophic failures through a controlled shutdown process.

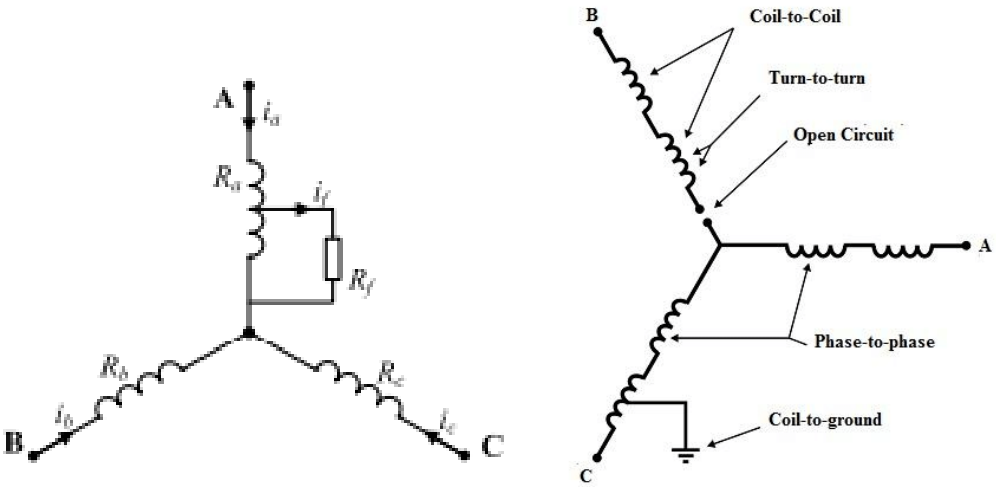

(a) Inter-turn short circuit fault (b) Stator winding faults

Figure 2.5: An inter-turn fault in comparison to all stator windings faults [36]

2.4 Condition monitoring

Condition monitoring plays a vital role in ensuring the reliable operation of electric motors. It is a proactive maintenance strategy that involves constant monitoring of equipment and systems to detect signs of potential faults or deviations from standard operating conditions. Condition monitoring is a key approach to predictive maintenance, seeking to pinpoint potential issues before they escalate into motor failure, thereby averting significant downtime and associated costs. Common parameters monitored are vibration, temperature, magnetic flux, humidity and current[54].

Condition monitoring relies on the collection and analysis of data from various sensors and monitoring devices. These devices are strategically placed on the motor to measure different parameters such as vibration, temperature, pressure, electrical signals and more. The collected data is then analyzed to identify anomalies, patterns and trends that indicate potential faults. Sensors are installed on the motor in critical areas or positions where they can capture relevant data. The selection of the sensor type depends on the application used. Sensors constantly gather data either in real-time or at regular intervals. The collected data is analyzed using specialized software or algorithms to compare data with historical trends to help identify anomalies or indicators of potential defects. If the analysis detects abnormal behavior or faults, alerts or notifications are raised by the monitoring software to inform of the need for maintenance. If proactive maintenance is implemented these abnormalities can be fixed, achieving optimized performance.

2.5 Fault diagnostics

If valid inspection and preventive maintenance are not achieved, then potential defects can evolve over time and cause damage to the machine. Fault diagnostics are methods used when a fault has already occurred in the motor and is in an early stage of severity. The main idea behind diagnostics is to find the causes behind a fault while the motor is still operational so that a potential malfunction or breakdown of the motor can be prevented. That is why these techniques are only implemented in conditions where the defects do not cause immediate breakdown of the machine. Any possible fault will produce an asymmetry in the magnetic field, which will be passed on to the electrical, magnetic and mechanical spectrum waveforms. All diagnostic techniques that are going to be listed have a common start, as they all aim to

use signal analysis methods to detect the fault in the form of harmonics [55]. Harmonics are integer multiples of the fundamental frequency f_0, which corresponds to the normal operating speed of the motor, which can indicate motor issues. Typical methods are motor signature current analysis (MCSA), torque or magnetic flux monitoring, vibration analysis, Park's vector approach and others, each of them applied to an electrical, magnetic, or mechanical fault respectively. Other diagnostic techniques make use of mathematical modeling or, more recently, algorithms and methods of artificial intelligence (AI).

2.5.1 Motor current signature analysis

The most widely used tools for identifying PMSM faults are methods that perform frequency domain analysis. The time domain signal is transformed into its frequency spectrum, and then, compared to the frequency amplitude and phase of healthy state machines, faults can be detected. The idea behind these methods is that faults create harmonics in the current signal that are not easily observed in the time domain. Signal processing in the frequency domain, particularly through Fast Fourier Transform (FFT) is well-established and remains a widely used diagnostic approach. Among them stands motor current signature analysis (MCSA), a method that is based on monitoring and recording the stator current in the steady state with the following spectrum analysis of the current signal in the frequency domain using FFT. The prevalence of this method is attributed to its simplicity, security, cost-effectiveness and capabilities of online and remote machine state monitoring. In PMSM, the use of this method can indicate stator winding defects, rotor eccentricity and demagnetization fault[56].

For the diagnosis of PMSM stator winding faults, the amplitudes of the characteristic frequency components of the inter-turn short circuits in the spectrum of stator current are monitored. A rise in the amplitude of the frequency components will occur as a result of the fault, described by:

$$f_{itsc} = f_s \cdot (1 \pm \frac{k}{p}) \quad where\ \ k = +1, +2, +3, \dots \quad and\ \ p : pole\ \ pairs \tag{2.6}$$

Moreover, an inter-turn short circuit can lead to increased amplitude in slot harmonics, which are additional harmonic components due to the slots of the stator core. They are calculated by:

$$f_{itsc,2} = f_s \cdot (1 \pm k\frac{N_s}{p}) \quad where\ \ N_s : the\ \ number\ \ of\ \ stator\ \ slots \tag{2.7}$$

According to [57], the most significant indicator for the occurrence of this fault is the third harmonic $3f_s$, as there is a high increase in its amplitude. The magnetic field asymmetry leads to current unbalances which appear as an increase of the third harmonic of the stator current. The negative sequence current is the current that arises due to unbalanced conditions such as ITSC faults and refers to the component of current that flows in the opposite direction of normal positive sequence currents of phases A, B, C in a three-phase system. The negative sequence current interacts with the fundamental harmonic of the rotor and produces an oscillating torque with a frequency twice the fundamental. The oscillation of the turns causes field components with frequency three times the fundamental, relative to the stator.

Another diagnostic method for indicating ITSC faults is the use of symmetrical components of the stator phase current. The three-phased balance indicator is:

$$f_t = |I_a - I_b| + |I_b - I_c| + |I_c - I_a|, \quad where\ \ I_a, I_b, I_c : the\ \ three\ \ phase\ \ currents \tag{2.8}$$

Assuming that I_{ps}, I_{ns}, I_{zs} are the stator current components of positive sequence, negative sequence and zero sequence respectively in a three-phase system. Under healthy-state operation, the positive sequence current is equal to the total phase current, while the other two components

are equal to zero. When a stator fault occurs, there is an asymmetry of the three phases, as one of them has less impedance than the others. There is a significant increase in the amplitude of the frequency f_s in the negative sequence component. The positive sequence current on the contrary remains untouched by this type of fault. As a result, the zero sequence current component is no longer equal to zero. The equations that describe the positive sequence, negative sequence and zero sequence stator currents are respectively[58]:

$$I_{ps} = \frac{I_a + a \cdot I_b + a^2 \cdot I_c}{3} \tag{2.9}$$

$$I_{ns} = \frac{I_a + a^2 \cdot I_b + a \cdot I_c}{3} \tag{2.10}$$

$$I_{zs} = \frac{I_a + I_b + I_c}{3}, \quad where \ a = 1\angle 120^\circ \tag{2.11}$$

For accurate detection of the severity of the fault, both the current and voltage negative sequence harmonics should be considered. However, this method can be not so reliable as there are factors that can lead to incorrect estimation of the negative sequence current and subsequently to false positive diagnostic alarms. These factors include the wrong calibration of the equipment, asymmetry of power supply, inherited asymmetries of the windings and motor temperature.

MCSA is a widespread method for the diagnosis of eccentricity as well. The mechanical misalignment causes distortions in the magnetic flux distribution inside the motor and thereby, corresponding current harmonics are induced in the stator current. The characteristic frequency components for all categories of eccentricity faults in PM motors are defined as:

$$f_{ecc} = f_s \cdot (1 \pm \frac{2k-1}{p}), \quad where \ k = 0, 1, 2, 3, \dots \ and \ p : pole \ pairs \tag{2.12}$$

It has been proven that the harmonic at $f_s(1 - \frac{3}{p})$ is more associated with static eccentricity, while the harmonic at $f_s(1 + \frac{1}{p})$ is linked to both static and dynamic eccentricity. When only dynamic eccentricity occurs, harmonics appear at integer multiples of the frequency $\frac{f_s}{p}$.

A variation of this method applied for detecting eccentricity is Static Fault Diagnosis - Motor Current Signature Analysis (SFD-MCSA). It is an off-line diagnostic tool mainly used for static eccentricity in induction motors or PM motors with a slotted design that generate Principle Slot Harmonics (PSH). Principle slot harmonics are harmonics in the current waveforms due to the interaction of the stator slots with the winding currents and are affected by the number, shape and geometry of the slots or the distribution of the windings. This method is proper for static eccentricity as this fault originates from the manufacturing quality of the motor and not from its operating conditions. The PSH were proposed to be associated with the following formula, which later was proven to be associated with other types of faults as well:

$$f_{slot} = f_s \cdot (1 \pm \frac{k}{p}) \quad where \ k = 1, 2, 3, : representing \ the \ harmonic \ order \tag{2.13}$$

Last but not least, MCSA is applied to detect early-stage demagnetization faults of the permanent magnets. The appearance of disturbances in the magnetic field of the permanent magnets results in distortion of the distributed sinusoidal magnetomotive force. Hence, the magnetomotive force in both normal and faulty states will generate a current containing multiple frequencies, which means that additional harmonics emerge in the stator current spectrum around the fundamental supply frequency. The characteristic frequencies for demagnetization faults include the following harmonic components:

$$f_{dem} = f_s \cdot (1 \pm \frac{k}{p}) = f_s \pm k f_r \quad where \ f_r = \frac{f_s}{p} : the \ rotational \ frequency \ and \ k = 1, 2, 3, \dots \tag{2.14}$$

The suitability of that method lies in the fact that a rise in the degree of demagnetization of the magnets leads to an increase in the amplitude of the stator current harmonics. However, the visibility of demagnetization symptoms is heavily dependent on the winding configuration and in certain cases, there might not be any harmonics other than those present in a healthy motor due to inherent natural asymmetries in the motor.

In summary, MCSA is a widely adopted diagnostic tool applied for detecting both electrical, mechanical and magnetic defects due to the benefits it presents. Although it can alert for the presence of a fault, sometimes it is almost impossible to distinguish the three types of failures by only analyzing the stator current, as all of them present harmonics at the same frequency components. For that reason, other diagnostic methods are also implemented, or Finite Element Analysis (FEA) is used, a numerical method where a complex structure is decomposed into finite elements, each of them tested under different parameters and conditions.

2.5.2 PVA and EPVA

The Park's Vector Approach (PVA) is a classical method applied to any three-phased device for asymmetries detection caused by stator winding faults. The method is based on the splitting of the current into the quadrature and direct axes, so that the geometric locus of these two components can be formed[59]. Under ideal conditions, the geometric locus of the two current components should be a circle. However, in the case of an inter-turn short circuit fault, an asymmetry is created between the three phases, distorting the geometric locus. The $d-$ and $q-$ axis currents are calculated by the following formulas:

$$I_d = \frac{\sqrt{2}}{\sqrt{3}} i_a - \frac{1}{\sqrt{6}} i_b - \frac{1}{\sqrt{6}} i_c \Rightarrow I_d = \frac{\sqrt{6}}{2} I_M cos(\omega t) \tag{2.15}$$

$$I_q = \frac{1}{\sqrt{2}} i_b - \frac{1}{\sqrt{2}} i_c \Rightarrow I_q = \frac{\sqrt{6}}{2} I_M cos(\omega t - \frac{\pi}{2}) \tag{2.16}$$

where i_a, i_b, i_c: the three phase currents and I_M: the maximum amplitude of the positive sequence current
In the case of an electrical fault, the geometrical locus looks more like a ring. The direction of the distortion can identify the fault that occurred. When the shorted turns are in phase A the Park's vector locus is directed more to the upper left. Conversely, when the short-circuited turns are in phase B the locus is directed more to the upper right, while the locus is shifted downward if the fault occurs in phase C.

The Park's Vector Approach has been further extended so that it led to the formation of Extended Park's Vector Approach (EPVA). EPVA[60] is a developed method to upgrade the diagnostic capabilities of the PVA. It is characterized by increased sensitivity to the severity of the electrical fault. This method uses a modulus current which is calculated from the two currents in the $d-$ and $q-$ axis according to:

$$I_{mod} = \sqrt{I_d^2 + I_q^2} \tag{2.17}$$

The idea is that an inter-turn short circuit fault leads to an asymmetry between the three phases of the windings. This causes harmonics to appear in the spectrum of the modulus of the Park's vector, at frequency components at $2kf_s$, where $k = 0, 1, 2, 3$. As the number of short-circuited turns increases the amplitude of the modulus current harmonics also increases. In a healthy motor, the two current components I_d and I_q have a phase difference equal to 90°, which means that they are perpendicular to each other. Hence, the I_{mod} current has only DC component. It is noted that for the spectra of the current components in these two approaches, the FFT is used.

2.5.3 Vibrations analysis

Vibrations analysis is a method based on analyzing the electromagnetic vibrations sources of PM motors. Its application primarily lies in the detection of mechanical faults. Vibrations and acoustic noise are inherent features in PMSM, as various factors produce them even in normal operation. Cogging torque, torque ripples and radial forces contribute to the vibration of the motors. These electromagnetic sources exhibit distinct harmonic orders that correlate with the natural frequencies of the PMSM's stator. Consequently, a thorough examination of the harmonic orders associated with each electromagnetic vibration source during the design phase allows for targeted efforts towards a substantial reduction of vibrations and acoustic noise. Similar to MCSA, this method uses the FFT to examine the harmonics of these sources[61]. To measure the vibrations, an accelerometer can be installed on the engine.

Under normal operation, the stator vibration frequency is expected to be twice the frequency of the power supply. The occurrence of an inter-turn short circuit fault or three-phase asymmetry in the stator windings can introduce magnetic field asymmetry, leading to irregular vibrations. This, in turn, generates harmonic components at $4f_s$ and $8f_s$ in addition to the fundamental frequency at $2f_s$ in the vibration signal. Thus, the fault signatures are exhibited at frequencies at $2kf_s$, where $k = 1, 2, 3, \ldots$.

Regarding mechanical faults, vibrations analysis is considered the most effective diagnostic tool. When a local mechanical failure, such as a broken bearing, occurs in the motor, it comes into contact with other parts of the motor and produces a shock pulse in the vibration. The equations that relate the vibration frequency for inner race, outer race, ball faults and cage faults in the bearings are respectively:

$$f_{in} = \frac{N \cdot f_r}{2} \cdot (1 + \frac{d}{D} \cos \alpha) \tag{2.18}$$

$$f_{out} = \frac{N \cdot f_r}{2} \cdot (1 - \frac{d}{D} \cos \alpha) \tag{2.19}$$

$$f_{ball} = \frac{D \cdot f_r}{2} \cdot [1 - (\frac{d}{D} \cos \alpha)^2] \tag{2.20}$$

$$f_{cage} = \frac{f_r}{2} \cdot (1 - \frac{d}{D} \cos \alpha) \tag{2.21}$$

where f_r: the rotational speed, N: the number of rolling balls between the inner and the outer ring, d: the rolling element diameter, D: the pitch circle diameter and α: the contact angle of the bearing

2.5.4 Stray flux monitoring

Stray flux monitoring involves the measurement and analysis of stray magnetic flux in an electric motor. Stray flux[62] refers to the magnetic flux paths that deviate or stray away from the intended or designed magnetic circuits inside the motor. In an ideal electric motor, the magnetic flux generated by the stator windings should follow a specific path, linking the stator to the rotor to produce torque and drive the motor. However, some magnetic flux might deviate from this specified path and create stray flux. In stray flux, the magnetic field lines travel outside the stator core and can be either radial or axial. Stray flux is associated with increased losses, inefficiencies and abnormal mechanical forces.

Monitoring stray flux can be a diagnostic tool, as changes in the stray flux patterns can be indicative of certain faults. When applied to PMSM, it can determine shorted turns, air gap eccentricity and magnet demagnetization. Techniques for stray flux monitoring include the use

of sensors, such as Hall effect sensors or magnetic field sensors, like those in Figure 2.6, placed radially, axially, or in a combined orientation to measure magnetic fields and identify areas of stray flux. Numerical simulations and models can also be employed to predict and analyze the stray flux behavior.

Practically, the stray magnetic field is the attenuated air gap magnetic field. The frequency characteristics of this residual magnetic field are important to analyze as the energy conversion takes place in the air gap of the motor. In case of an ITSC fault, the current flowing through the shorted turns affects the magnetic field, as it increases the magnetomotive force near the shorted turns resulting in increased magnetic flux near these turns. By monitoring the stray flux with the applied sensors externally, the stator faults can be detected and the faulty coil to be located. Similarly, mechanical and magnetic faults can be detected. The vibration and noise that appear, lead to magnetic asymmetries that define fault signatures in the magnetic flux spectrum.

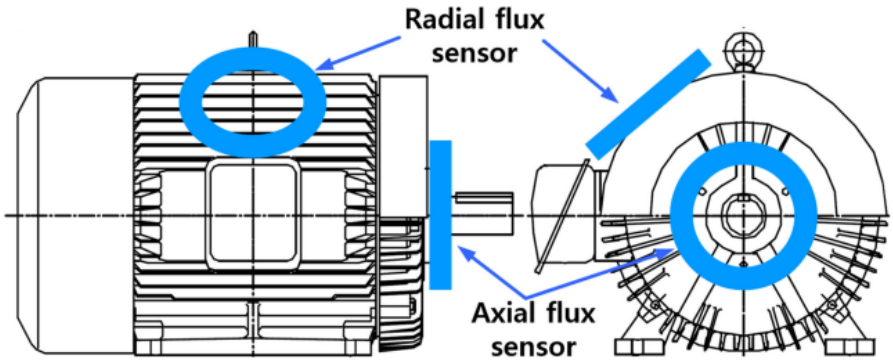

Figure 2.6: Placement of axial and radial flux sensors [63]

2.5.5 Torque and power monitoring

Numerous techniques can be applied at steady state conditions as diagnostic methods. Among them is torque monitoring which offers fault signatures in the same frequency components with vibrations analysis. This method typically involves installing torque sensors on the motor shaft that measure the torque applied to the shaft or transmitted through the drive train and then convert mechanical torque into an electrical signal. The torque signal is acquired and processed to monitor the motor operation. However, the installation of torque sensors is both expensive and not practical, so it is preferred to estimate the torque signal. The signal of the electromagnetic torque is estimated as a function of measurements and calculations of stator currents and voltages in the direct and quadrature axes.

Power monitoring involves the measurement and analysis of electrical power input and mechanical power output during motor operation. Particularly, it can be used to measure the active, reactive, or apparent power parameters, to calculate the power factor for how efficient the motor energy consumption is. To monitor the power, sensors are installed in the electrical supply lines to calculate the power input using the formula: $P_{in} = V \times I \times \cos\phi$. Simultaneously, the mechanical power output is measured by monitoring the motor's shaft rotational speed and torque. It is calculated using the formula: $P_{out} = T \times \omega$. The power conversion efficiency indicates how effectively the motor converts electrical power into useful mechanical power and is equal to

$$n = \frac{P_{out}}{P_{in}} = \frac{T \times \omega}{V \times I \times \cos\phi} \tag{2.22}$$

2.5.6 Thermography and speed monitoring

Other methods use sensors or devices as well, such as thermography or speed monitoring. These methods are useful as supplementary tools to assist with condition monitoring and fault diagnosis. Thermography uses digital thermometers and thermal imagers or infrared cameras to record temperature data in different parts of the motor[64]. When a fault occurs, it reveals a specific heat signature that can help to locate it. Speed monitoring involves installing tachometers, resolvers and encoders to record the position and angular information of the motor's shaft that are related to the motor speed. The procedure of thermography via an infrared camera with the images it produces are shown in Figures 2.7 and 2.8 respectively. Variations in all these methods from usual data are indicative of potential faults.

Figure 2.7: Examining a motor with thermography [64]

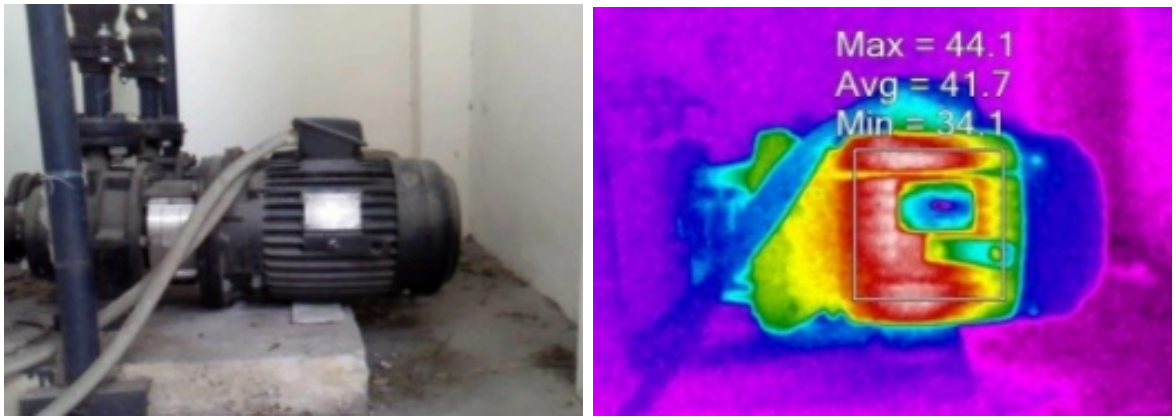

(a) (b)

Figure 2.8: A real image of a motor with its thermographic image [64]

3 Diagnostics methods applied to accelerated ageing

Among the components critical in the performance of electric propulsion systems, the insulation systems arguably stand out as the most crucial factor. There are numerous materials used for insulation purposes around the conductors with different key technologies each depending on the application. The components that constitute an insulating system are responsible for certain procedures that involve not only protection of the stator windings but also heat dissipation from conductors and mechanical support, as they can decrease the mechanical vibrations in the conductors caused by magnetic forces[65].

Consequently, pole insulation of traction motors undergoes several stresses, the intensity and impact of which are contingent on the specific application. Electrical, thermal and mechanical factors contribute to these stresses, which gradually lead to insulation degradation by accelerated aging of the insulation materials. Local incipient defects within the insulation layers present a notable threat to the machine, as they can evolve rapidly into more severe faults, potentially leading to a failure of the entire insulation system. The consequences of insulation failure can be catastrophic, elevating the risks of accidents by compromising electrical safety. The most common failure is the stator inter-turn short circuits, in which high currents flow through the defected stator windings. Moreover, downtime resulting from repairs and time-consuming repairs incur significant costs. Therefore, it is necessary to select the material combinations capable of withstanding these diverse stresses in the design of insulation systems.

Many diagnostic tests have been developed to assess insulation conditions and forecast their remaining lifespan. These evaluations serve as the basis for informed decision-making about maintenance, rewinding, replacement, or repair. Insulation testing and monitoring can be conducted offline, online, or as part of scheduled and periodic inspection and maintenance activities. Some of the most widespread insulation tests are the insulation resistance test, polarization index, surge test, partial discharge, high voltage test, dissipation factor or tanδ measurements. By the proper implementation of these tests, the insulation systems can be protected from further aging and material degradation.

3.1 Insulation systems

Insulation systems of stator windings in PMSM exhibit unique features aimed at preventing certain faults that lead to catastrophic motor breakdown including inter-turn short circuit faults, copper losses and heat dissipation from the conductors. They also help prevent vibrations and noise, caused by mechanical forces.

One of the most crucial factors that affect the machine cooling and thereby the electrical load is the thickness of the insulation layers. This thickness is referred to bibliography as thin film[66]. Thin film insulation is a coating characterized by its thin and lightweight nature that has thermal resistance properties due to its low thermal conductivity. It is designed to provide high thermal resistance while minimizing the insulation layer thickness. This results in design compactness, low manufacturing costs and high efficiency in terms of torque production. The thin film can be composed of several materials, such as polymers, foils, or composite materials. The thinness of the film does not compromise its insulating properties but it usually relies on advanced materials and technologies to maintain efficient thermal resistance. These materials may incorporate reflective layers to reduce radiant heat transfer or utilize low thermal conductivity materials to impede thermal flow. The thin film composition highly depends on specific requirements and environmental conditions.

The nature of the insulation is also determined by the formation of the stator windings. There are two main types of stator windings, the random-wound and form-wound, a cross-section of which is depicted in Figures 3.1a and 3.2 respectively[67]. As shown in Figure 3.1b,

the random-wound configuration consists of conductors of enamel wires, separators for phase insulation, slot liners and slot wedges. The conductors are circular insulated coppers wrapped around randomly within the stator slots adjacent to each other. Typically, random-wound windings are equipped in machines with a power rating of several hundred kilowatts and a voltage level less than $1kV$. This random distribution of the stator coils can lead to a scenario where the turn connected to the input terminal is adjacent to the turn connected to the low-voltage neutral point. The first turn has a high voltage value while the other one has a very low value, meaning that a significant voltage difference will arise and therefore thicker insulation layers are needed. In contrast, form-wound windings are manufactured from rectangular copper strands. The conductors are pre-shaped, giving them the proper geometry and pre-insulated with secondary insulation before being inserted into the slots. The greater advantage of this configuration is the fact that conductors can be deliberately arranged to minimize the voltage between adjacent turns in the same coil, allowing the layers of turn insulation to be extremely thin.

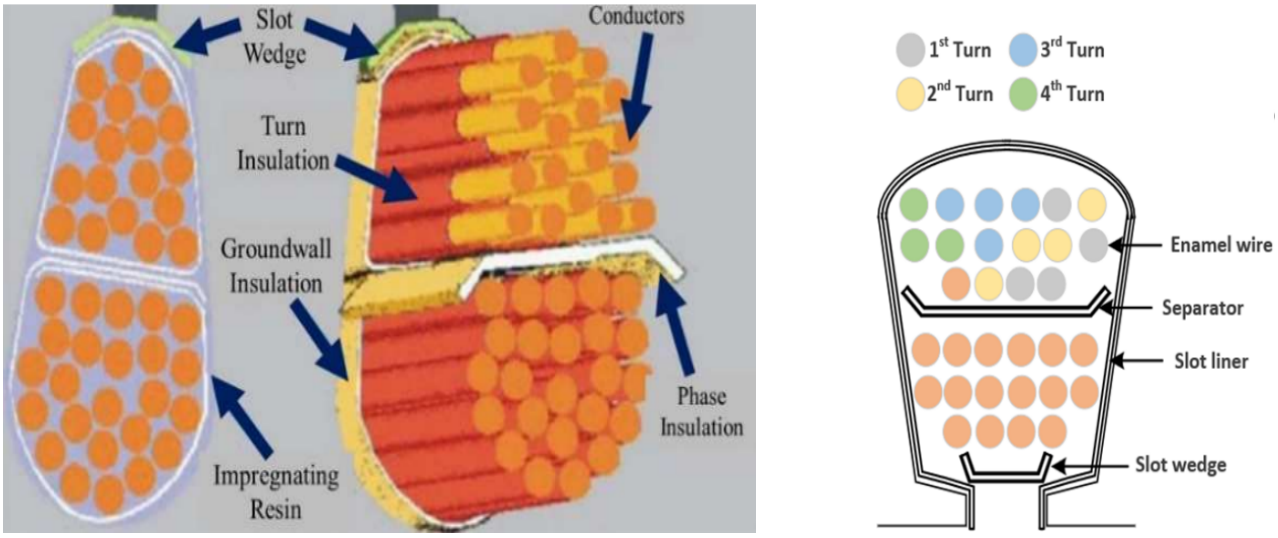

(a) (b)

Figure 3.1: Cross section of a random-wound coil [67]

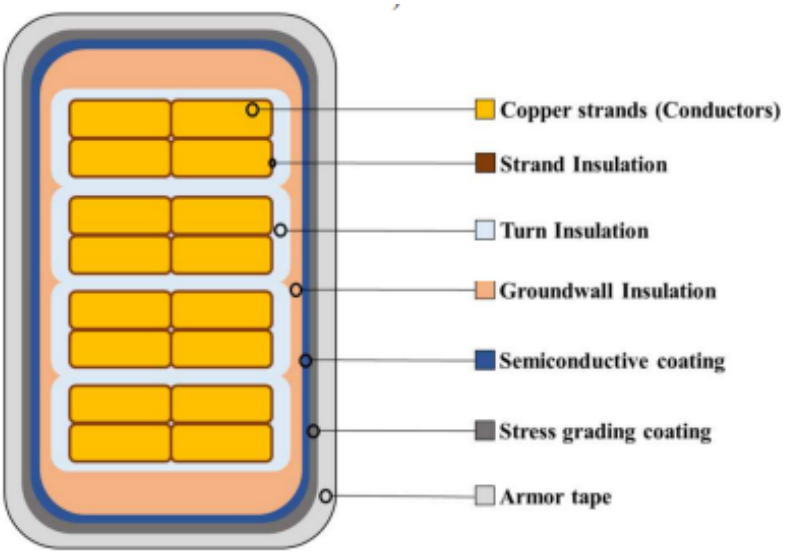

Figure 3.2: Cross section of a form-wound coil [67]

Insulation systems are composed of different components that are manufactured from a wide range of materials. The most important components are strand insulation, turn insulation and groundwall insulation. In Table 3.1 there is a categorization of the components used in each of the two main configurations of stator windings.

Random-wound coils	**Form-wound coils**
Strand/Turn insulation	Strand insulation
Phase insulation	Turn insulation
Groundwall insulation	Groundwall insulation
Slot wedge	Slot wedge
Coil separator	Top, Mid-stick and Bottom packing
Adhesive tapes	Blocking and bracing
Finishing varnishes	VPI Resin and resin-based technology
Impregnating resin	Semiconductive coating

Table 3.1: Insulation components in the two types of stator windings

Strand insulation involves the segmentation of the copper conductors into smaller bars due to mechanical and electrical reasons. Unlike form-wound coils, in random-wound coils the strand and turn insulation are the same. A conductor in a large machine must have a large cross-section to carry the current, but it will be difficult to bend to create the coils. This is solved by dividing the conductor into smaller ones. In addition, it reduces the skin effect, so the conductor resistance is not affected during its operation in AC. The electrical losses are reduced, including the reduction of higher harmonics and eddy currents, so high efficiency is achieved. Strand insulation adjusts voltages between adjacent strands.

Turn insulation protects the turns from short circuits between them. Inter-turn short circuits pose a hazard to machine operation and have the potential to lead to a ground-wall fault. It is exposed to turn-to-turn, phase-to-ground, coil-to-coil and transient voltage surges. Essential for withstanding elevated temperatures arising from losses, it must have adequate thermal properties and mechanical behavior. Turn insulation plays a crucial role in the longevity of the stator windings.

Groundwall insulation is responsible for separating the copper conductors from the grounded stator core. It protects the surface of the stator core, slots, teeth and end-winding. If the insulation fails, a relay is activated to disconnect the machine from the mains. Groundwall insulation must have good thermal, electrical and mechanical properties. The insulation is the pathway of heat transmission from the conductors to the core, so it must have high thermal conductivity to avoid high temperatures in the conductors, while it receives the total phase voltage on it. Air gaps must also be avoided, which increase the thermal resistance of the insulation that changes the chemical properties of the materials. Moreover, powerful magnetic forces act on the conductors resulting in a force equal to:

$$F = \frac{c \cdot I^2}{d} = \frac{c \cdot A^2(1 - cos2\omega t)}{2d} \ \frac{kN}{m}, \ if \ \ I = Asin(\omega t) \tag{3.1}$$

where c: a constant, d:the slot width and I:the RMS current of the conductor.
Some pole windings contain a Nomex layer, a kind of properly designed insulation paper that offers high inherent dielectric strength, mechanical toughness, flexibility and resilience. It separates the inner part of the coils from the core of the pole and finds strong application in permanent magnet synchronous axial flux motor topologies. It is used as a fabric in both fiber and sheet forms where resistance from heat and flame is required.

Other parts of the insulation system are slot liners and slot wedges, which provide mechanical support for the coil inside the slot. In form-wound coils, there are semiconductive coatings and

stress relief coatings, which are vital for defense against mechanical and thermal stresses. These coatings are manufactured from semiconductive materials like silicon carbide mixtures or silicon resins.

3.2 Insulation materials

Various materials can be used as components of an insulation system. They can be categorized into organic and mixed organic/inorganic materials. The first category includes materials based on polymers such as polyimide(PI), polyamide-imide (PAI), and polyesterimide (PEI) [68] that are mainly used in low-voltage machines. The second category consists of materials that are used in high-voltage applications and are more tolerant in partial discharges, a phenomenon that will be analyzed later. Table 3.1 summarises the most common materials used for the different components of the insulation systems.

COMPONENT	MATERIAL
Strand insulation	Enamel/Heavy polyester/polyimide/polyamide-imide/ polyester or glass fabric tape and combinations
Turn insulation	Kapton/polyimide/mica/epoxies and combinations in films
Groundwall insulation	Mica/Impregnated PET/epoxy resins
Slot wedges	Silicone/epoxy resins/rubber/glass filled epoxies and combinations
Slot insulation	Impregnated PET/Nomex/mica/PET films and combinations
Impregnating resin	Polyester/polyester-imide/ polyurethane
Semiconductive coating	Silicon carbides and combinations of semiconducting materials
VPI Resin/resin-rich technology	Varnishes/alkyd resins/silicone resins/ polyester/polyester-imide/polyurethane
Finishing varnishes	Isophthalic acid/Alkyd resin

Table 3.2: Common materials found in the insulation components

In many high-performance machines, once coils are placed into the slots, an encapsulation or potting process typically is employed. This involves immersing the winding in a polymer/epoxy resin or varnish. In certain instances, these resins may be infused with particles like alumina. The objective of such procedures is to eliminate air voids and enhance dielectric strength, mechanical durability, thermal conductivity and heat dissipation. The process of impregnating the coils with epoxy resin is known as winding impregnation. Hence, epoxy resin found broad application in the electrical industry due to its dielectric resistance and strong corrosion resistance[69]. Much research has been done to study epoxy resin's insulation characteristics under different AC voltage frequencies to enhance its performance.

The materials used for insulating purposes in electric motor applications can be categorized into classes, depending on the maximum allowable temperature that can be exposed during motor operation. The materials that belong to the same class usually present similar -if not the same- chemical properties and dielectric strength. The division of these classes has been formed according to NEMA standards, the National Electrical Manufacturers Association. They are presented in Table 3.3 with their respective temperature limits. The second column of the table shows the maximum winding temperature of each class, while the third column presents the index at which if the allowable temperature is exceeded the insulation continues to work steadily reducing its lifespan until it fails. Of these classes, classes B, F and H are most commonly used,

as the temperature limits of class A limit the range of applications in which it can be used. There is also class C which has the highest thermal resistance and is used in more recent and modern traction applications but does not follow the NEMA standards. It is necessary to choose the right materials for importing tapes, polyester compounds, papers and insulating tapes to ensure the service life and reliability of insulation systems.

NEMA Letter Class	Maximum Hot Spot Temperature Allowed	Relative Thermal Endurance Index
Class A	105 °C	> 105 to 120
Class B	120 °C	> 130 to 155
Class F	155 °C	> 155 to 180
Class H	180 °C	> 180 to 200
Class C (NOT NEMA)	>180 °C	> 220 to 250

Table 3.3: Categorization of insulation classes

3.3 Insulation degradation

Insulation systems in the stator windings are subjected to various stresses during motor operation [70]. Inside the motor, high currents flow through conductors and mechanical vibrations occur in the coils of the poles of the motor. These result in increased temperatures and heat that affect the insulation layers. These stresses are known as TEAM stresses, an abbreviation for Thermal, Electrical, Ambient, and Mechanical stresses. While thermal, electrical and mechanical stresses are easy to relate to the phenomena mentioned at the beginning of the paragraph, ambient stress is not exactly a stress but represents the environmental conditions to which the insulation is exposed and includes the effects of dust and moisture. Usually, the machine is not solely subject to one stress, but some combination of them occurs or one stress leads to the others. The intensity and impact of each stress varies, which makes the aging profile unpredictable.

The thermomechanical and electrical loads are the reason for the existence of local hot spots within the motor[71] due to inherent manufacturing defects. As the manufacturing process is not ideal, some minor insulation damage may occur in the early stages of coil production. This damage can result from deformation during bending and pressing. Hot spots are localized areas where the temperature is significantly higher than the surrounding areas. These often lead to wear, puncture, or detachment of the insulation, as the high temperatures result in changes in the chemical composition and dielectric properties of the materials [72]. The dielectric materials have a certain temperature point at which they can withstand high temperatures. When the electric motor operates at a temperature above the allowable winding temperature, the service life will always be reduced. In fact, an increase of 10°C above the maximum allowed can halve the life of motor insulation. The thermal stresses are the main reason for the delamination effects of the insulation layers. The purpose of the motor insulation classes, which were analyzed previously, is to describe the insulation capacity of the motor winding to handle heat.

Also, high currents and voltage surges, which are sudden rises in voltage that only last for a very short amount of time, can break the insulation layers and thereby inter-turn short circuit faults can occur, which if they are not diagnosed in time progressively lead to motor failure. In the case of voltage surges, the voltage can reach 10% or above the nominal voltage and they are typically caused by rapid changes in heavy electrical loads or magnetic interference of stray flux.

In the following images, some common insulation defects are presented[73]. In Figure 3.3, damage to the tape occurs before it is applied to the coil. The mica layer is separated from the

supporting backing tape during unwrapping from the roll.

(a) (b)

Figure 3.3: Coil cross section showing tape damage before applied to the coil [73]

In Figure 3.4, air voids and delaminations are visible in coil groundwall insulation due to issues in manufacturing processes or gradual degradation because of thermomechanical stresses. Delamination refers to the separation of layers in layered and laminated materials. As the insulation layers are no longer tightly connected with resin, air is trapped between the turns of the coil. Air voids are pockets or spaces within an insulation material where air is trapped due to delamination.

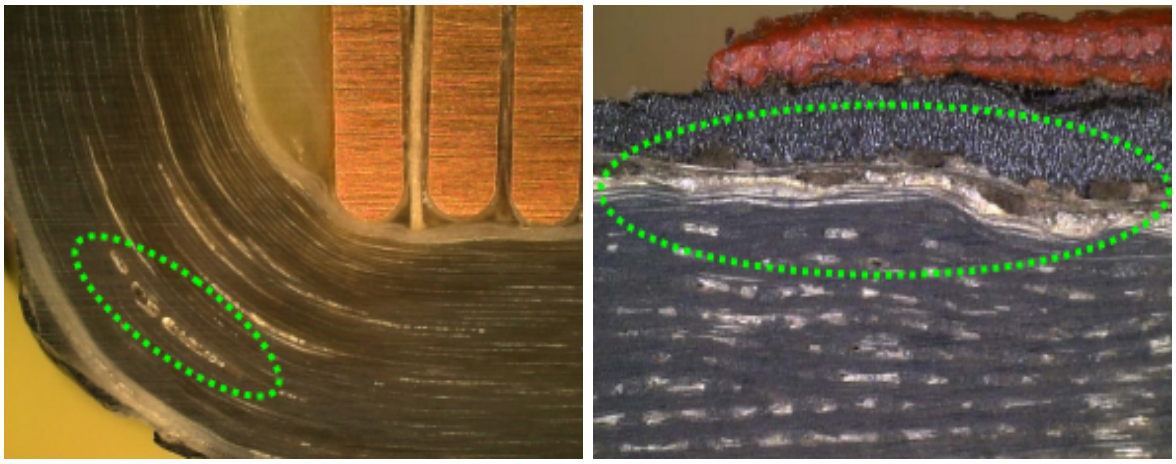

(a) (b)

Figure 3.4: Coil cross section showing voids and delaminations [73]

In Figure 3.5, deformations called wrinkles and folds are caused by improper taping in the insulation layers. Tape wrinkles are mostly created during the taping process. Wrinkles are small folds or creases in the insulation material that can create localized thickness variations in the insulation, reducing its effectiveness and potentially allowing for the penetration of moisture and contaminants. Folds are larger bends or overlaps in the insulation material that create weak points against the consistent protection of the coil.

In Figure 3.6, other deformations are shown that are named sharp edges. Sharp edges refer to points or lines where the insulation material forms a sudden and acute change in direction, creating a narrow or pointed feature. Sharp edges are the product of local insulation overpress due to tooling issues during the manufacturing process. They may lead to stress concentration points, where the insulation is more susceptible to tearing or wearing over time.

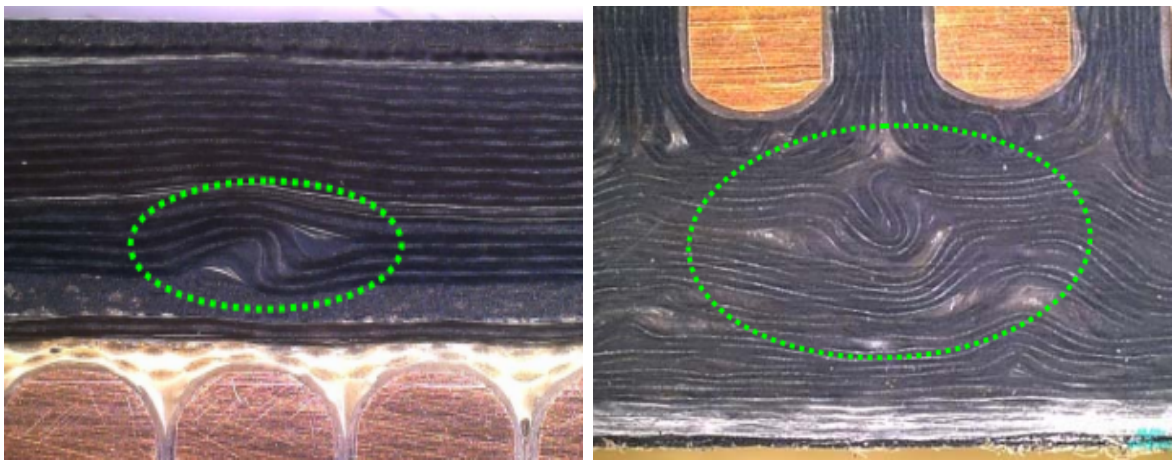

(a) (b)

Figure 3.5: Coil cross section showing wrinkles and folds [73]

(a) (b)

Figure 3.6: Coil cross section showing sharp edges [73]

The insulation was manufactured with either Vacuum Pressure Impregnation (VPI) or Resin Rich (RR) processes, two processes used for insulating electrical components with resin. In the first process, a vacuum chamber is used to evacuate the air from the chamber where the component is placed, creating a vacuum and when a desired vacuum level is reached the chamber is filled with insulating resin, which is then pressed and soldered. The vacuum contributes to removing air from the pores and voids within the component. The second process involves reinforcing materials with a high ratio of resin, creating a protective layer of resin on the surface of the component.

3.4 Partial Discharges

An important factor that affects the insulation system is the existence of air voids in the groundwall. Air pockets in the insulation would allow for vibrations in the conductors leading to the deterioration of the insulating system. Air movement through insulation diminishes its effectiveness because it increases convective heat loss. Delamination enables air to be trapped between the turns of the coils, which contributes to the appearance of partial discharges (PD)[74]. Partial discharges are electrical sparks that occur in air gaps in the insulating material due to the non-uniform distribution of the electric field. The term "partial" refers to the fact that

they only involve a portion of the insulation, rather than a complete breakdown of the entire insulation system. These localized dielectric discharges occur as they do not bridge the two conductors perfectly under the presence of high voltages of the order of a few kV. If there is an air void in the groundwall, the high electric field stress causes a breakdown of the air leading to sparking. Ionization of the air takes place as it becomes conductive by allowing charge to continuously leak off the conductor into the air. The electrons and ions of the spark cause premature aging of the insulation and if not detected and fixed, they progressively perforate the insulation leading to failures. Therefore, delamination defects must be prevented with proper systems.

Partial discharges can occur in gaseous, fluid, or solid insulating mediums [75]. The main difference between them is that in fluids such as the air, partial discharges are visible while in solids they are invisible. Two main phenomena are characteristic in fluids the Corona Discharge (CD) and Brush Discharge (BD). Corona discharges occur when the electric field strength surrounding a conductor surpasses the dielectric strength of the air (or other fluid). The phenomenon is observed due to the radiating bluish glow in the air that emits light next to the pointed metal conductors. While corona discharges occur at sharp points and edges, usually with a radius smaller than 1mm, brush discharges occur at a curved electrode [76] with a radius between 5 and 50mm. Brush discharges are characterized by numerous luminous writhing sparks and plasma streamers formed by ionized air molecules, that repeatedly strike out from the electrode into the air. They are usually accompanied by crackling sounds. The streamers spread out, creating a visual resemblance to a "brush". These two types of discharges are illustrated in Figure 3.7.

(a) A Corona Discharge in transmission line (b) A Brush Discharge in a coil

Figure 3.7: Partial discharges phenomena in air [76]

Similar phenomena may occur in solid insulation materials like epoxy resin. Electrical treeing is the term for the electrical pre-breakdown phenomenon in solid materials [77]. It progresses through the stressed dielectric insulation in a path resembling the branches of a tree. Impurities and defects create excessive electrical field stress that ionizes the gases in the voids within the bulk dielectric, causing small electrical discharges between the walls of the voids. Ultraviolet light and ozone from the discharges can react with the nearby dielectric, leading to decomposition, further degradation of the insulating capabilities, and new cracks and voids appearing. In the pictures below in Figure 3.8, a needle is used to create partial discharges in a polymer-based material, pinpointing that the curvature radius of the needle can change the morphology of the "tree" [78]. As time passes by, the tree becomes more and more dense.

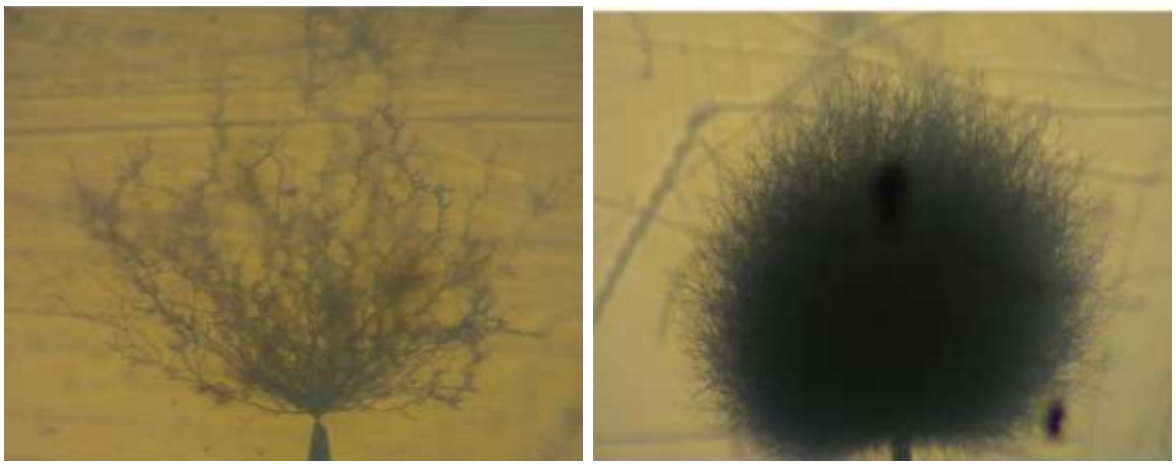

(a) Electrical tree in a "tree" shape (b) Electrical tree in "bush" shape

Figure 3.8: Partial discharges morphologies in polymers [78]

Solid insulating materials can contain voids or cavities in the medium between the electrodes and the dielectric. Two conductors or a coil with the grounded core in our case can be considered as two parallel plates with the solid material between them. Hence, a capacitance is formed between these plates and can be expressed by the dielectric constant of the material, which is the ability of the material to store energy. The dielectric constant is correlated with the permittivity of the material as a ratio to the permittivity of the vacuum, which is expressed as:

$$k = \varepsilon_r = \frac{\varepsilon}{\varepsilon_o} \tag{3.2}$$

0 where k: the dielectric constant, ε_r: the relative permittivity, ε: the permittivity of material and ε_r: the permittivity of vacuum $= 8.85 \times 10^{-12} F/m$. These voids have a dielectric constant of one, the relative permittivity of air, and exhibit a lower dielectric strength compared to the surrounding material. Consequently, the electric field strength within the voids exceeds that of the dielectric material. Therefore, even under standard operational voltages, the field within the voltages can surpass their breakdown threshold[79]. The breakdown threshold is a characteristic of the dielectric materials. When the voltage across the void surpasses the critical threshold, a discharge is triggered causing the voltage to drop rapidly. This discharge is extinguished shortly after, typically within 0.1 microseconds. The voltage in the voids begins to rise again and discharges recur. Therefore, the frequency of these discharges is strongly dependent on the applied voltage.

During each discharge, heat is generated in the voids leading to carbonization of the void surfaces and corrosion of material. The gradual corrosion and consequent reduction in the thickness of the insulating material eventually lead to breakdown. This breakdown process unfolds slowly and may extend over a long period of time.

The equivalent circuit of a bulk dielectric, featuring a cavity, can be visualized in Figure 3.9 as a capacitive voltage divider with an additional capacitor in parallel [80]. Under healthy conditions, there will be only the capacitance C_b that represents the capacitance of the healthy dielectric material in parallel to C_b that represents the capacitance of the rest of the insulation. In series with the C_b is C_c which represents the void. The gap parallel to C_c shows that void collapses after applying sufficiently high voltage across it. If voltage V_0 is applied then:

$$V_{void} = V_c = \frac{Z_{void}}{Z_{void} + Z_{ins}} \cdot V_0 = \frac{C_b}{C_b + C_c} \cdot V_0 \tag{3.3}$$

It can be shown that partial discharges depend not only on the voltage but also on the electric field. It is essential to calculate the respective electric field intensities in the previous equation

in case we want to predict whether a discharge will occur. The capacitance and electric field intensity are given by the formulas:

$$C = \frac{\varepsilon \cdot A}{d}, \quad where \quad \varepsilon = \varepsilon_o \varepsilon_r \quad and \quad E = \frac{V}{d} \tag{3.4}$$

where A:the width of the conductors, d:the distance between them and V:the voltage difference between them. So the formula in (33) can be transformed to:

$$V_c = \frac{\frac{\varepsilon_{r_b}}{d_b}}{\frac{\varepsilon_{r_b}}{d_b} + \frac{\varepsilon_{r_c}}{d_c}} \cdot V_0 \tag{3.5}$$

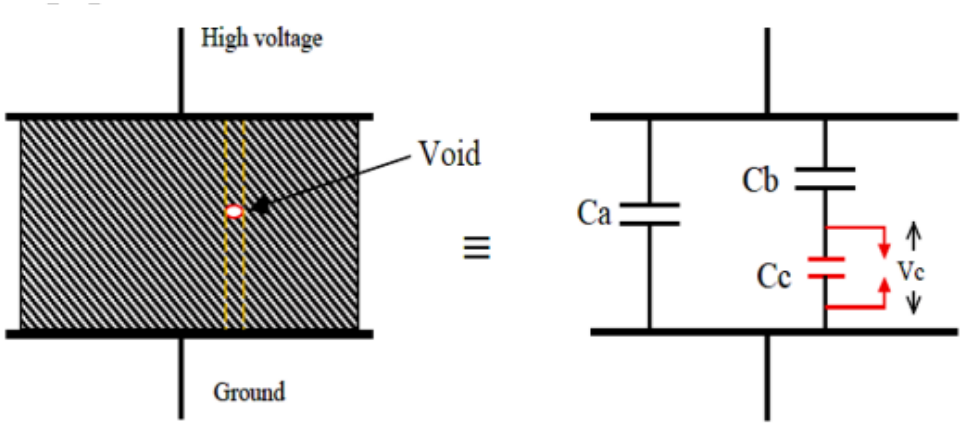

Figure 3.9: Equivalent circuit of partial discharges [80]

The stator core and coil turn can be considered as two parallel conducting plates. The negatively charged electrons of the insulation atoms, leave their positions as they are attracted to the positive voltage plate. This process is called ionization. As the electrons accelerate, on their way to the positively charged plate, they collide with other atoms which are also ionized. The positive charges are correspondingly attracted to the negatively charged plate. The electrons and ions create a conductive plasma that bridges the voltage difference between the plates and the result is the electrical breakdown of the dielectric.

At room temperature, pressure of one atmosphere (100kPa) and of low humidity, the air has an electrical resistance of 3kV/mm. If the pressure is tripled, roughly the same will happen to the voltage. In general, the resistance of gaseous insulation depends on the pressure and humidity of the gas. In contrast, solid insulators such as epoxy resin and composites of polyester show resistances around 200 kV/mm, so discharges in these materials cannot occur without air voids. Partial discharges lead to ion and electron bombardment at chemical bonds of insulation, especially in organic materials. Over time, a hole will form in the insulation, which will result in a ground fault.

Some industrial motors contain coatings that prevent the occurrence of partial discharges in any air void between the windings and the stator core. These coatings are known as groundwall stress relief coatings. As the width of the windings is smaller than that of the stator teeth, manufacturers coat the coils with partially semiconductive (semicon) coating, either paint or tape enriched with graphite. Its resistance is very small since the coating is in contact with the stator core meaning at ground potential. Hence, the voltage drop across the air void is zero and partial discharges are eliminated.

3.5 Diagnostic methods

TEAM and manufacturing stresses affect the health of the insulation systems and exacerbate their aging, as they contribute to the occurrence of partial discharges, reduced dielectric strength and chemical properties, delamination, oxidation and severe other electrical faults. Thus, many diagnostic methods have been adopted as proactive approaches for early-stage detection of potential faults, preventing catastrophic breakdown of the insulation systems. Diagnostic tests can be divided into two main categories: the online tests that are performed while the motor is in operation, presented in Fault Diagnostics, monitoring the deterioration of insulating materials by capturing real-time stresses, and the off-line tests[81], which involve diagnostic procedures performed on motor windings when the motor is not in operation. These are applied shortly after the motor is shut down and disconnected from the power supply. Insulation resistance (IR) test, Breakdown High Voltage (HV) test, Frequency Impedance Spectroscopy and Dissipation Factor (DF) measurement are among them. Offline testing helps to identify potential issues before they escalate, aiming to prevent unexpected downtime, extend motor life and enhance overall system reliability.

3.5.1 Insulation resistance & Polarization Index test

Insulation Resistance (IR) test is the most frequently utilized method for detecting pole insulation defects. It is also called Megger test[82] from the name of the company that developed the first measuring system. This test aims to assess the health of the insulation system by measuring the resistance between the conductive components of the insulation. When measuring the groundwall resistance, it measures the resistance between the turns of the coil and the stator iron core.

The insulation resistance test shall be carried out following the IEEE 43 standard "IEEE Recommended Practice for Testing Insulation Resistance of Electric Machinery"[83]. According to IEEE 43, insulation resistance is a measure of the conductivity of an insulation system and is defined as the ability of winding insulation to resist direct current. It involves the application of high DC voltage across winding insulation for 1 minute. It is calculated by dividing the applied direct voltage of negative polarity by the current passing through the insulation and taken at a specified time (t) from the start of the measurement. All resistance measurements must be corrected to use a constant, compensated temperature of 40°C.

For the test setup[84], a high-voltage DC source, typically 500V or 1000V, is connected to the equipment under examination. The positive terminal of the DC source is connected to the conductive end of the winding, while the negative terminal is connected to the ground of the insulation. The voltage is applied for a specified duration, typically one minute, allowing the insulation to charge. Then, the insulation resistance is measured by a high-impedance device, the megohmmeter. The megohmmeter applies a specific DC voltage and measures the resulting current flowing through the insulation. The insulation resistance is calculated using Ohm's law $R = \frac{V}{I}$, where R is the insulation resistance, V is the applied DC voltage and I is the measured current. Its value can be compared to the manufacturer's recommended minimum insulation resistance value. Typically, a higher value indicates better insulation quality. Ideally, this resistance should be infinite to prevent any current leakage between the copper and core. However, in reality, insulation resistance has a very high value instead of being infinite. A low resistance value is a mark of an issue within the insulation system.

To make the measurement less sensitive to temperature, an alternative to the IR test is utilized, known as the Polarization Index (PI) test [85]. High DC voltage is applied over a specified time period, typically for 10 minutes. It is defined as the ratio of the insulation resistance value at the tenth minute divided by the insulation resistance value at the first

minute, according to the formula:

$$PI = \frac{R_{10}}{R_1} \tag{3.6}$$

The IEEE 43 standard recommends a minimum PI value of 2.0 for most insulation systems. The two resistances are calculated using Ohm's law, but it needs attention as the current does not remain constant over the time of the measurement.

Four primary current components compose the total current: the capacitance current I_C, absorption current I_A, conduction current I_G and surface leakage current I_L. By the four currents, the Insulation Resistance Profile (IRP) can be exported, shown in Figure 3.10, appearing as an inverse exponential function.

- The capacitance current I_C decreases exponentially and is equal to:

$$I_C = I_0 \cdot e^{-\frac{t}{\tau}}, \quad where \quad \tau = RC \tag{3.7}$$

  This is because when a continuous voltage is applied to a capacitor, initially a high current flows through it which decays exponentially. The magnitude of the internal resistance of the source and the capacitance of the capacitor determines the exponential damping.
  The IR measurement has been set to a duration of one minute in order to disregard the effect of capacitive charging. Particularly, a form-wound stator coil can have a capacitance between the core and conductors equal to $1nF$ or a hydroelectric generator may have a $1\mu F$ capacitance. It is easy to understand that the current is practically zero in less than 10s.

- The conduction current I_G is the current that flows due to electrons or ions crossing the insulation and traveling from the conductors of the coil to the stator core. Conduction current can be present if the insulation has absorbed moisture. It can also appear if there are cracks or holes in the insulation and there is contamination such that it creates a galvanic coupling between the conductors and core. This current is constant in time and ideally equal to zero. Modern insulation systems lead the conduction current to zero under healthy conditions. Any deviation from zero indicates a fault.

- The surface leakage current I_L is a direct current that flows on the surface of the insulation of the windings. It exists due to external pollutants, such as oils or moisture mixed with soil, dust, dirt, ash, chemicals, salts, etc that cause current conduction. Ideally, this current is zero. High values of this current are associated with the rapid aging of insulation, as there is electrical conduction and heat. Studies have shown that surface leakage current is high in machines with round rotor windings or in salient pole windings, in which the excitation winding is exposed.

- The absorption current I_A is the last primary current component. Most dielectric materials in the insulation system contain polarized dipoles. By applying an external electric field, these dipoles are aligned. The energy needed for the alignment comes from a current provided by the voltage source.
  When alignment is succeeded, the current becomes zero. This current is named polarization current and is part of the absorption current. Current also flows through the layers of the insulating tape. The reason is that there are trapped electrons within these layers. Experience has proved that the absorption current is initially high and driven to zero after approximately 10 minutes in modern groundwall insulation systems.

Among the four primary current components, only conduction and absorption currents contain diagnostic information. If only R_1, the resistance that corresponds to the measurement for the

first minute, is measured, the absorption current has not been equal to zero yet. R_1 depends on the temperature, which means that an increase of 10°C decreases the R_1 from 5 to 10 times. The Polarization Index can help to mitigate the impact of temperature.

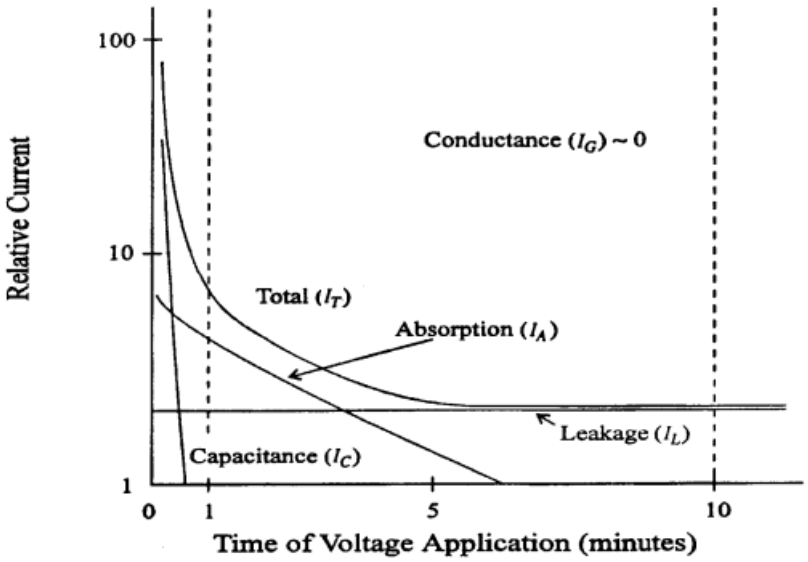

Figure 3.10: Primary current components of PI test [84]

IR and PI tests can only detect contamination, moisture and some other serious defects. The current components are not affected the same by the presence of moisture, contamination, embrittlement and temperature. When moisture is present on the surface of the insulation system, the surface leakage current I_L is dominant in the overall test current I_T, while the absorption current I_A becomes negligible. Thus, the insulation resistance and the time in which this is achieved are dramatically reduced. When moisture is inside the insulation system, the conduction current I_G is dominant and the absorption current I_A is negligible.

When some kind of surface contamination occurs, the surface leakage current I_L becomes higher than that of a healthy insulation system and causes spikes in the IR profile. In the case of an insulation system that becomes embrittled, after being subjected to TEAM stresses, the absorption current I_A is affected. The ability of the insulation to polarize reduces, which leads to a "flattening" of the IR profile.

The impact of temperature on insulation results in changes in the conduction current I_G. A decrease in the overall insulation resistance, which is caused by an increase in temperature, increases the conduction current I_G.

The following table provides a guideline for the DC voltages applied during Insulation Resistance and Polarization Index tests. The winding rated voltage refers to rated line-to-line voltage for three-phase AC machines, line-to-ground voltage for single-phase AC machines and rated DC voltage for DC machines or rotor windings, according to IEEE 43 standards[83].

Winding Rated Voltage (V)	**Insulation Resistance Test Direct Voltage (V)**
$<$ 1000	500
1000 - 2500	500 - 1000
2501 - 5000	1000 - 2500
5001 - 12000	2500 - 5000
$>$ 12000	5000 - 10000

Table 3.4: A Guideline for DC Voltages to be applied for IR/PI Test

3.5.2 Surge test

Surge test, also called surge comparison, is a method that tests the integrity of turn-to-turn insulation of coils, mostly in induction motors[86]. It can directly measure the integrity of the insulation in any windings topology of stator and sometimes even in rotor windings. It is applied based on IEEE 522 standard[87]. It is also based on the use of high DC voltage.

Motors powered by power electronics exhibit sudden voltage spikes, which leads to an imbalanced voltage distribution across the coils. If the occurrence time of these spikes is too short, the voltage is high enough and there is a weakness in the insulation then there will be a breakdown leading to a fault. Surge test simulates this phenomenon, as it is a destructive measurement in which the specimen will either pass or will be destroyed. If the insulation fails the test procedure, it is automatically assumed that in real conditions it would also fail under switching conditions, power converter surges, or dynamic phenomena[88]. The test setup for

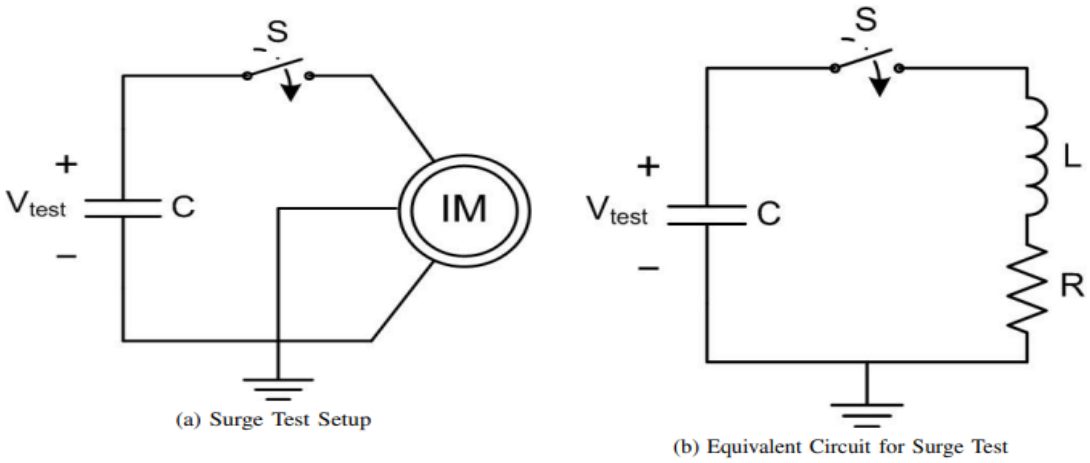

(a) (b)

Figure 3.11: Surge Test Setup with its equivalent circuit [86]

the surge test and the equivalent circuit for it are shown in Figure 3.11. In essence, when the windings are tested, a fault between turns can be diagnosed due to the change of resonant frequency. The capacitor is charged by a high DC voltage through the winding. When the charging of the capacitor is finished, the switch S in 3.11b closes. The stored energy of the capacitor oscillates the circuit. The resonant frequency, the characteristic frequency in which the system reaches its maximum degree of oscillation, is:

$$f = \frac{1}{2\pi\sqrt{LC}}, \tag{3.8}$$

where L and C are parameters from the circuit.

If there is no fault, then the oscillation frequency remains constant. On the other hand, if there is a turn-to-turn fault, then the circuit is driven to decrease the circuit inductance and increase the resonant frequency. This can be detected on the oscilloscope. The surge test can also be applied comparatively between the three phases.

3.5.3 High Potential test

A HiPot test, an abbreviation of High Potential test, also known as a Dielectric Withstand test, is a diagnostic procedure that applies high voltage between the windings and ground. The aim is to determine the adequacy of the insulation to withstand voltage transients and ensure that insulation is not marginal. During the test, the insulation resistance and current leakage are monitored. If the insulation system is intact and has sufficient dielectric strength, it should be able to withstand the high applied voltage without allowing excessive current leakage. However, if there are any defects in insulation, such as cracks, voids, or contamination, the high potential test may reveal them by causing electrical breakdown or excessive leakage current. There are three main types of HiPot testing, based on the voltage sources used: AC HiPot, DC HiPot, and Very Low Frequency or shorter VLF at 0.1Hz [89].

DC HiPot involves high DC voltage to be applied in the stator windings. The DC voltage exceeds the peak AC voltage of the motor under normal operating conditions. The voltage is gradually increased from zero volts to a specified level and maintained for a predetermined duration, typically for 1 minute, according to IEEE 95 standards[90]. After that period it is gradually decreased back to zero volts. A winding passes the test when it maintains the test voltage for one minute without experiencing insulation breakdown or tripping the overcurrent protection of the test set. DC Hipot test provides satisfying but limited diagnostic information, as it can detect insulation weaknesses that are more pronounced under DC stresses, such as surface tracking or partial discharges. Failures during the DC HiPot test are indicative of the need for repairs or rewinding, as they indicate a break in the insulation between the coil and the core.

The AC HiPot test highly resembles the DC HiPot test[91]. The main difference lies in the fact that AC voltage is applied at 50Hz (or 60Hz with American standards) following NEMA MG1 or IEC 60034 standards [92]. The AC test voltage increases gradually at the desired level and is maintained there for one minute. Similar to DC testing, the windings successfully pass the test if they can withstand the high AC potential for one minute without any insulation abnormalities being observed. It is considered to be more effective than the DC test, as it can detect more insulation defects. An alternative to AC HiPot is the Very Low Frequency (VLF) test, which involves applying a continuous sinusoidal AC voltage ranging from 0.1 to 1Hz. VLF testing is particularly effective for assessing the condition of high-voltage cables and insulation systems, as the lower frequency allows for better penetration into the insulation and detection of defects, such as water trees and partial discharges.

The choice of the type of high potential test varies, depending on different factors[93]. The use of AC HiPot testing at power frequency has been adopted worldwide for new machinery due to its ability to reproduce the stress conditions encountered during operation, the perceived effectiveness of AC testing in locating defects and the ease of access to AC power sources. For maintenance purposes, both DC and AC tests are employed, with DC testing being favored. This preference stems from the availability of cheap and small DC power supply sources compared to similarly rated AC sources, the ability to stop tests warning signals are received before a catastrophic failure occurs and the diagnostic insights gained from controlled testing. Conversely, VLF testing appears to be decreasingly used in recent years for rotating machines. That technique shifted towards cable testing.

3.5.4 DC Ramp test

Similar to the DC HiPot test, in DC ramped voltage testing a DC voltage is gradually increased from zero to a predetermined level at a defined ramp rate per minute over a specific time. The voltage ramp rate, duration and maximum voltage level are selected based on industry standards [90] or testing objectives. Commonly used rate are 1kV/min or 2kV/min, reaching up to 15kV in a total period of 15 minutes or in half of that period respectively. The removal of manual voltage adjustments enhances both voltage control and test sensitivity compared to the conventional DC HiPot test.[94] By slowly ramping up the voltage, the test focuses on detecting insulation weaknesses that may not be apparent during steady-state or instantaneous voltage tests.

During the DC ramp test, the insulation current and the voltage applied are recorded and plotted in X-Y axes, providing the I-V response curve which is continuously monitored[95]. The continuous monitoring of the current allows for better control as each measurement is compared to past value records to detect potential changes or abnormalities in the current. The measured current can be separated into its leakage, capacitive and absorption components.

If a given voltage $U(t)$ is applied in a linear insulating material, the general equation in the time domain for current $I(t)$ is:

$$I(t) = \frac{C_0 \sigma U(t)}{\varepsilon_0} + C_0 \frac{\partial}{\partial t}[\varepsilon_\infty U(t) + \int_0^\infty f_s(\tau) U(t-\tau) d\tau] \tag{3.9}$$

$$and \quad I(t) = I_L(t) + I_C(t) + I_{abs}(t) \tag{3.10}$$

where C_0:the vacuum capacitance, ε_0:the vacuum permittivity, ε_∞:the dielectric constant of the insulating material and σ:its conductivity. The function $f_s(t)$ is the material dielectric response calculated from the slow polarization process. The analytical solution of the total current $I(t)$ involves the use of numerical methods.

When a linearly rising voltage is applied, the voltage function is $U(t) = at$, where a:a constant, and the capacitive charging current can be assumed constant, since:

$$I = C\frac{dV}{dt} = C \cdot a = constant \tag{3.11}$$

Therefore the capacitive current can be neglected in equation (41). Variations in the rate of voltage rise will lead to nonlinear changes in the leakage current and consequently to the measured current. It is crucial to maintain a steady rate and well-regulated high-voltage power source.

3.5.5 Partial Discharge Analysis

The off-line Partial discharge analysis (PDA) is a method employed to assess the condition of the insulation by examining electrical discharges within the insulating material. These discharges are absent or negligible in well-built stator windings that are in good condition, but they will occur in systems that are subjected to contamination by dirt, and moisture or to defects, such as air voids and corona effect. Partial discharges contribute to the corrosion of the insulating material and may eventually lead to its failure. Additionally, they can form gases and acids, such as nitric acid and ozone, which accelerate the deterioration of insulation.

The Partial Discharge Analysis relies on the fact that each partial discharge generates a current pulse with high frequency components to the hundreds of megahertz (MHz) in the Fourier spectrum [96]. This current pulse is the result of the current $i = \frac{dq}{dt}$ from the movement of electrons in the air gap, each of them carrying a charge q and the flow of positive ions in the opposite direction. Any device designed to detect high frequencies can identify these PD pulse

currents. The most conventional means to detect PD currents is by a high-voltage capacitor connected to the stator terminals, typically ranging from 80 pF to 1000 pF. The capacitor presents a high impedance to the high AC in the stator, yet offers a very low impedance to the high-frequency PD pulse currents. The output of the high-voltage capacitor drives a resistive load, typically a 50-ohm resistor. As the PD pulse current passes through the capacitor, it generates a voltage pulse across the resistor, which can be observed on an oscilloscope, frequency spectrum analyzer, or other display device. The lower band of the detector is the frequency range of the high-voltage detection capacitor combined with the resistive or inductive-capacitor network load. Early detectors were sensitive to frequencies in the ranges of 10kHz, 100kHz and 1MHz. Modern detectors can be sensitive up to several hundred megahertz ranges. The PDA is conducted under the IEEE 1434 standard[97].

Measurement units for testing are voltage in mV (milliVolts) and charge in pC (pico-Coulombs) [98]. Partial discharges can be measured both online and offline in machines with rated voltages surpassing 6kV, exceeding the 3kV/mm threshold for partial discharge occurrence in air voids. Various analyses of partial discharge levels are suggested, including:

1. evaluation of the number of pulses in a single cycle
2. determination of the magnitude of the pulses
3. assessment and analysis of the shape of the distribution of the pulses to the discharge location

According to the IEC60270 standard [99], new and repaired machinery should undergo PD measurements to determine the condition of the impregnation process. Numerous test circuits can be used for PD measurements. All of them can be summarized into the following circuit in Figure 3.12 as the most commonly used circuit:

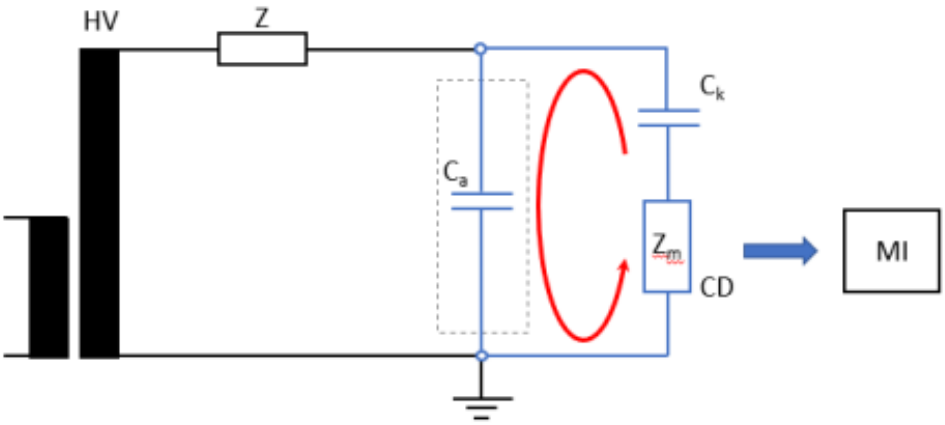

Figure 3.12: PD equivalent measurement circuit [100]

In this Figure [100], HV is the high-voltage supply, Z is the high-voltage filter, which is optional, C_a is the capacitance of the device under test, C_k is the coupling capacitor, Z_m is the measuring impedance that decouples the PD signals, CD is the coupling device and MI the PD detector instrument. The high-voltage filter aims to attenuate unwanted signals, referred to as background noise, and can disturb the sensitivity of the measurement. In particular, it reduces the high frequency interference from the voltage source and limits the propagation of transient signals into the voltage source. The coupling device converts the pulse current to the output voltage displayed in the instruments afterward. It can also include fast overvoltage protection and some filtering features that separate the test voltage and allow for synchronization.

A typical PD measurement in an oscilloscope is shown in Figure 3.13. The apparent charge expressed in pC has been used to measure the intensity of a partial discharge pulse. The apparent charge of a PD refers to the charge that, if injected within a very short time between the terminals of the test object in a circuit under test, would give the same reading in the measuring instrument as the PD current pulse itself. This is determined by the integral of the current over time within the frequency limits of the measuring system. The key is to measure the peak PD magnitude, the magnitude of the highest PD pulse due to the fact of being proportional to the largest defect in the insulation.

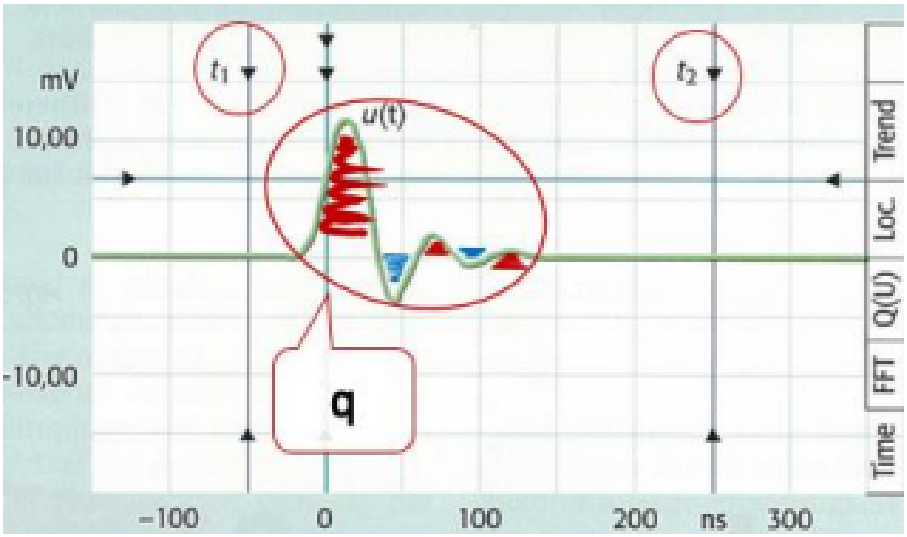

Figure 3.13: Time domain integration of a PD pulse [100]

Measurements also include:

1. The voltage marking the onset of the partial discharge, known as Partial Discharge Inception Voltage (PDIV)
2. The voltage marking the cessation of the partial discharge, known as Partial Discharge Extinction Voltage (PDEV)
3. The highest repeatedly occurring magnitude of the partial discharge at rated voltage

The charge can be calculated by the integration of the current going into a resistor:

$$q = \int_{t1}^{t2} i(t)dt = \frac{1}{R}\int_{t1}^{t2} u(t)dt \tag{3.12}$$

3.5.6 Capacitance measurements

Capacitance-to-ground (CTG) and capacitance tip-up (CTU) measurements are diagnostic tests used in high-voltage systems that can provide valuable information about the capacitive characteristics of the insulation system and thereby identify insulation abnormalities[98]. Changes in capacitance values may indicate the deterioration of the insulation system. Particularly, capacitance-to-ground measurement involves determining the capacitance between the windings and the ground. The test assesses the state of insulation wear by conducting multiple measurements during the motor lifespan. A rise in capacitance suggests contamination of insulation by moisture or external agents, like dirt, oil, or chemicals. On the contrary, a decrease in capacitance reveals aging or thermal degradation.

Capacitance-tip-up measurement detects intensified partial discharge activity in the insulation and should be monitored during the motor lifespan[101]. CTU measurement is conducted at both low and high voltages, signaling an increased occurrence of partial discharges in the insulation, giving:

$$CTU = CTG_{HIGH} - CTG_{LOW} \tag{3.13}$$

There are two ways to measure the capacitance tip-up. One way involves measuring each phase separately with an accurate capacitance bridge, while the other two are connected to the ground, which is the preferred method and the other suggests measuring the phase-to-phase voltage. The $HIGH$ value refers to the capacitance related to the rated line-to-ground voltage of the stator U_N and the LOW value refers to the capacitance that corresponds to the 20% of the rated line-to-ground voltage. The capacitance at low voltage corresponds to the capacitance of insulation with voids, whereas the higher the voltage, the voids have been shorted, so the one at high voltage corresponds to the insulation itself. The formula for capacitance tip-up is [102]:

$$\Delta C = \frac{C_{hv} - C_{lv}}{C_{lv}} \tag{3.14}$$

An increase in capacitance with voltage suggests the presence of internal voids. When voids are absent, capacitance remains unchanged as the test voltage is raised. A high value of ΔC is indicative of many voids in the winding groundwall. Figure 3.14 shows that the ΔC percentage is increased in proportion to the volume of voids within some insulation specimens of epoxy resin. For well-bonded modern epoxy mica groundwall insulation, the capacitance tip-up is usually less than 1%.

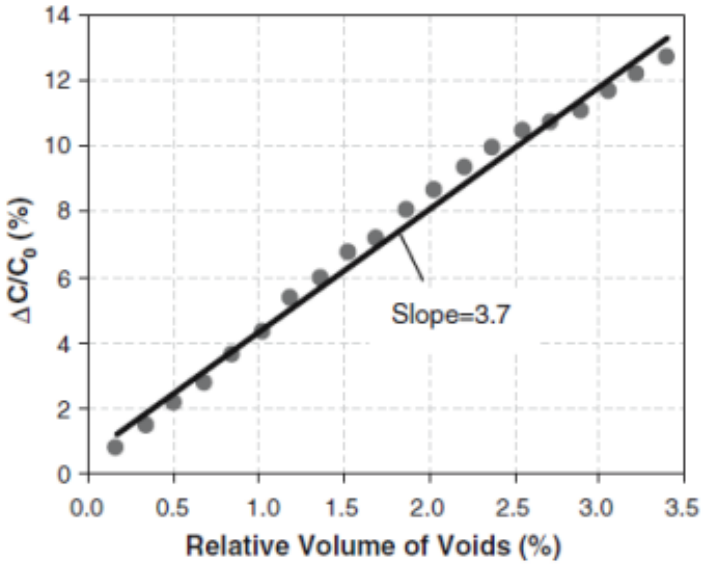

Figure 3.14: Change of ΔC as a function of the relative volume of voids within epoxy resin [96]

Tip-up testing relies on the observation that when phase-to-ground voltage is applied and voids exist within the groundwall insulation, the air in these voids ionizes [96]. Hence, sufficiently high conductivity is produced which can short the voids out. This results in a decrease in the effective thickness of the insulation, causing an increase in capacitance between low and high line-to-ground voltages. While a single void may not affect the system significantly, the presence of numerous voids due to inadequate resin impregnation or issues with tape or bonding materials in the insulation system will result in a noticeable change in capacitance.

3.5.7 Dissipation Factor & Power Factor measurement

Dissipation Factor (DF), also known as tanδ, and Power Factor (PF) or cosθ measurements are conducted to show the level of dielectric losses in the insulation system, exposing contamination or thermal degradation [103]. A single measurement cannot fully indicate the insulation condition, as dielectric losses vary based on material and machine size. Continuous monitoring throughout the lifespan of the motor is essential to accurately diagnose insulation degradation. Manufacturers commonly use Dissipation Factor or Power Factor measurements during the winding manufacturing process to verify the impregnation and curing quality of the insulation.

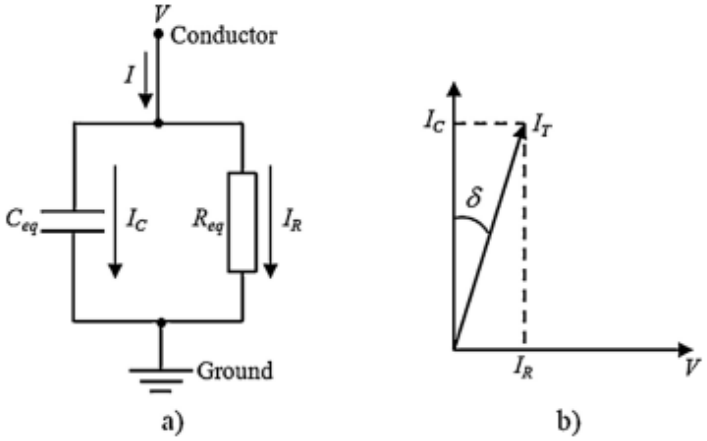

Figure 3.15: (a)Insulating material Equivalent Circuit and (b)Decomposition of the total current for DF and PF measurements [98]

The idea behind these tests is that in practice, insulation behaves differently from the ideal conditions. The insulating material can be visualized as a circuit, like that in Figure 3.15, which includes a capacitor C_{eq} and a resistor R_{eq}, which represent the ideal lossless behavior and dielectric losses respectively. When a 50/60 Hertz voltage is applied across the stator insulation, ideally the total current that flows through it resembles the current of any capacitor. The total current has two main current components [96]: a significantly high capacitive current I_C, leading the voltage by 90°, and a smaller resistive current I_R, in phase with the voltage. Under ideal conditions, there would be no resistive current, as there would be no dielectric losses and all of the total current would be capacitive. However, similar to the capacitance test, the presence of voids alters the dielectric properties of the insulation system. The dielectric of this simulated capacitor is the insulation between the windings and the stator core. Also, the total current precedes the voltage by an angle $\theta(< 90°)$ in the loss vector diagram of 3.15, which theoretically would be 90° in an ideal capacitor. Due to the resistive component, the complementary angle δ of angle θ is induced, representing the dielectric losses. The dissipation factor is the tangent of δ, which is between the total current I_T and the capacitive current I_C and is expressed as the ratio of the resistive current component to the capacitive current. The higher that ratio is, the higher the degree of insulation losses. The expressions for the relations between the angles of the loss vector diagram and the tanδ are respectively:

$$\delta + \theta = 90° \Rightarrow \delta = 90° - \theta \quad or \quad \theta = 90° - \delta \tag{3.15}$$

$$DF = tan\delta = \frac{I_R}{I_C} \tag{3.16}$$

The dissipation factor can detect several defects, including moisture, thermal deterioration, contamination or damage at the end windings. It can also be used to determine the degree of

curing of a new insulation system, as uncured components exhibit distinct dielectric properties compared to cured components. With the rise in the applied test voltage, the partial discharge activity within the voids will also increase, resulting in a corresponding increase of the resistive current I_R or real power loss. Thus, the Dissipation Factor measurements can indicate the existence of faults in the groundwall insulation and provide insights into its overall health condition. Digital measuring instruments have been adopted to measure the phase difference between the applied voltage and current flowing through the stator windings, which corresponds to the angle δ. The tangent of this angle translates into the dielectric losses. This test is conducted under the IEEE 286 [104], or IEC 60034-27-3 [105] standards.

Similar to the Dissipation Factor, the Power Factor (PF) looks for changes in the insulation of the windings. The Power Factor is expressed as the cosine of the angle θ, which is the angle between the applied voltage and the total current. From the loss vector diagram of Figure 3.15, the Power Factor is equal to the ratio of the resistive current I_R to the total current I_T:

$$PF = cos\theta = cos(90^\circ - \delta) = \frac{I_R}{I_T} \tag{3.17}$$

The Power Factor also expresses the dielectric losses of insulating materials. As the PF increases, it is indicative that there is moisture and contamination in the insulation system. Typical tests are conducted at a specified applied voltage that enables the comparison with the results from other motors. Their value lies in evaluating the level of curing in new coils or windings. However, the results may be affected by the presence of voltage stress control in a complete winding, leading to ambiguity in tests conducted on complete windings.

Practically, Power Factor is the ratio between the real power P to the total apparent power S, which is the product of the voltage applied across the conductors and iron core of the windings and the current flowing through. The measurement units are Watts (W) and Voltage-Amperes (VA) respectively. The most common tools used for measuring the Power Factor are the wattmeter and power analyzer, which directly measure the true power and apparent power and calculate their ratio.

$$PF = \frac{P}{S} = \frac{P}{VI} = \frac{W}{VA} \tag{3.18}$$

The correlation between the DF and PF is expressed as:

$$PF = \frac{DF}{\sqrt{(1+DF)^2}} \quad or \quad DF = \frac{PF}{\sqrt{(1-PF)^2}} \tag{3.19}$$

PF and DF measurements are performed by applying power-frequency AC voltage. If the windings are supplied with a low AC voltage, the measurement may lack reliability since the capacitive and inductive components of the equipment could induce power-frequency currents into the windings, thus distorting the measurement. To mitigate this issue, a frequency other than 50/60 Hz should be selected or alternatively, a high-power frequency voltage should be applied to the stator windings. Both measurements are used to ensure the quality of impregnation and curing of the insulation during the manufacturing process of the winding. A proper insulation satisfies the conditions $I_R \ll I_C$ and $I_R \ll I_T$.

3.5.8 DFTU & PFTU measurements

The Dissipation Factor Tip-Up (DFTU) and Power Factor Tip-Up (PFTU) tests appear as alternatives to the typical DF and PF tests [98]. They are defined as the difference of DF and PF values respectively, measured at two different voltage levels. The target of these tests is

to indicate the increase in dielectric losses resulting from the intensification of the activity of partial discharges in the insulation system [106]. The measurement of both these tests increases with voltage when delamination has occurred.

The DFTU testing involves measurements that start from 20% of the rated line-to-ground voltage and increase at voltage steps of 20% to the rated normal voltage. The purpose of the test is to monitor the increase in real power losses because of the voids in a delaminated insulation. Partial discharges and ionization of gas within the voids cause increased losses as a function of the applied voltage. The general equation describing this method is:

$$DFTU = \Delta(tan\delta) = DF_{HIGH} - DF_{LOW} \tag{3.20}$$

The IEEE 286 standard [104] recommends the 80% of the rated line-to-ground voltage for the $HIGH$ value and the 20% of it for the LOW value respectively:

$$DFTU = \Delta(tan\delta) = tan(\delta)_{0.8U_N} - tan(\delta)_{0.2U_N} \tag{3.21}$$

The IEEE 60894 standard recommends the 80% of the rated line-to-ground voltage for the $HIGH$ value and the 60% of it for the LOW value respectively:

$$DFTU = \Delta(tan\delta) = tan(\delta)_{0.8U_N} - tan(\delta)_{0.6U_N} \tag{3.22}$$

In addition to the variation of voltage levels for calculating DFTU, IEEE Std-286 allows the winding to be tested with a voltage up to 120% of the rated voltage U_N.

The total current I_T does not show a linear increase with voltage, as, besides the increased loss current I_G, there is also an increase in the capacitive current I_C due to the intensification of partial discharges. An example of a series of DFTU tests is shown in Figure 3.16. It highlights the non-linear behavior of the measurements of the dissipation factor as the applied voltage increases. Thus, to ensure an accurate diagnosis of the insulation condition, it is imperative to maintain constant test voltage over the motor lifecycle.

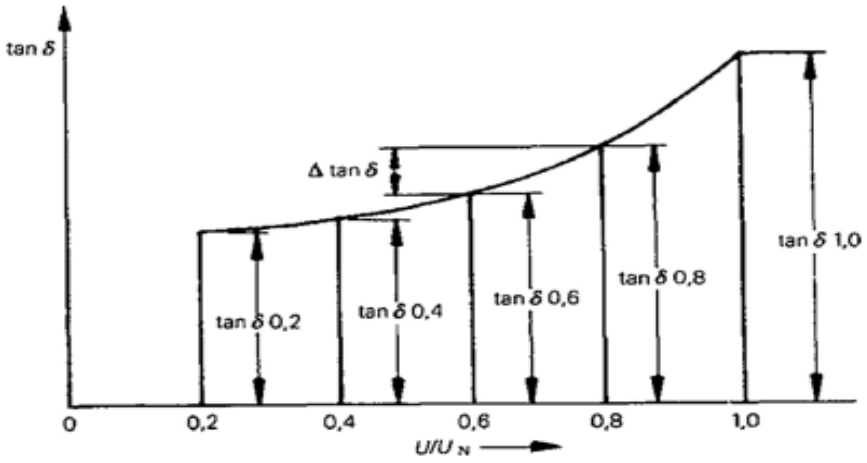

Figure 3.16: Example of a series of DFTU tests [98]

Similarly, the PFTU testing is conducted at two voltage levels. One measurement is taken at the voltage below the inception of partial discharge activity (PDIV), set at 25% of the line-to-ground operational voltage (PF_{LOW}) and the other at 100% line-to-ground voltage (PF_{HIGH}). Like DFTU, the difference between the two power factors at these two voltage levels can be attributed to the energy loss because of the partial discharges. The higher the difference, the more energy has been consumed. This test is defined according to the IEEE Std-286 and IEC Std-60034 [105].

$$PFTU = \Delta(cos\theta) = PF_{HIGH} - PF_{LOW} \tag{3.23}$$

3.5.9 Frequency Response Analysis

The Frequency Response Analysis (FRA) is a well-known technique that has been traditionally used on power transformers but has been eventually adopted for the diagnosis of rotary motors [107]. The FRA technique is widely adopted due to its high sensitivity and accuracy. It is based on the theory that deformations or displacements in the stator windings cause changes in the impedances of the motor components and thereby a modification of the frequency response. The technique involves the injection of a voltage signal with a constant magnitude but a varying frequency [108]. This approach reveals how the parameters describing the elements change as the signal frequency shifts. However, several issues can arise during this process. Firstly, the distribution of the device's parameters is unknown, essentially making it a black box. The frequency response depends solely on the geometry of the device and the material it was made from. This is because the FRA records how the electrical charge distribution changes with frequency throughout the device.

Therefore, a reference is needed to compare the response of a healthy motor, which remains consistent as long as the geometry and material conditions do not change. If either of these factors changes, the distribution of the electrical charge will vary and may be detectable through its frequency response.

In Figure 3.17, the equivalent circuit of any winding consists of capacitances, resistances and inductances in series and shunt connections. A variable frequency voltage is injected on one side of the winding, marked as V_1 the input voltage, and it is measured on the opposite side, marked as V_2 the output voltage. The impedance Z is the impedance of the voltage measuring equipment and is usually equal to 50Ω.

$$\vec{H}(j\omega) = \frac{\vec{V_2}}{\vec{V_1}} \quad or \quad H_{db} = 20 \cdot \log_{10} |\vec{H}(j\omega)| \tag{3.24}$$

Bode plots that express voltage gain H in decibels are usually preferred for the analysis. The Sweep Frequency Response Analysis (SFRA) is used to analyze and evaluate this transfer function. This involves applying a sinusoidal signal at one end of a winding and measuring it at the other end. The measurement results can be obtained with a FRA analyzer. The FRA analyzer generates the sinusoidal voltage with 1.44V amplitude, covering a frequency range from 20Hz to 20MHz. A computer then records the voltage transfer function to measure the input and output voltages.

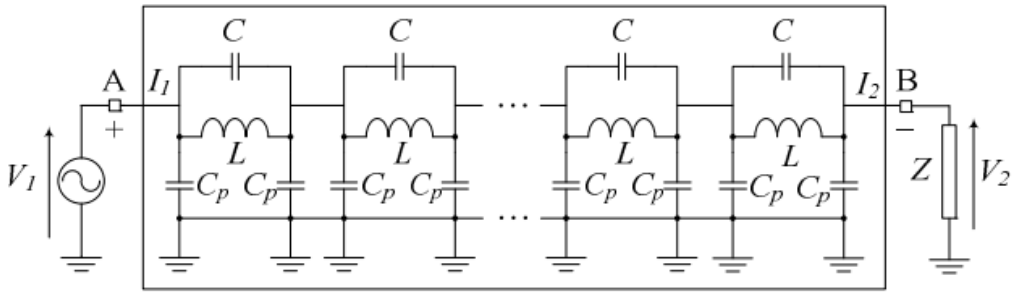

Figure 3.17: Representation of the FRA technique in a machine field winding [107]

3.5.10 Dielectric & Impedance Spectroscopy

Broadband Dielectric Spectroscopy (BDS) and Electrical/Electrochemical Impedance Spectroscopy (EIS) are non-destructive tests that are widely used for the examination of the dielectric response and the complex impedance responses over a wide range of frequency components.

Much research has been done, in which spectroscopy appeared as the primary tool for testing, ex-situ inspection, condition assessment and partially in in-situ inspection with both low and high voltages [109]. In-situ inspection refers to the examination of the condition of the insulation of the windings while the motor is still installed and operational within its designated environment. Ex-situ inspection, on the other hand, refers to the assessment of the insulation after the windings have been removed from the traction motor. In the literature, investigations of Dielectric Spectroscopy precede the studies done in Impedance Spectroscopy, which has been a subject of study for the last two decades.

- **Dielectric Spectroscopy**

Dielectric spectroscopy facilitates the assessment of the dielectric properties of a material or components. It analyzes the response of dielectric permittivity and loss over a range of frequencies. This method enables the evaluation of its polarisation and conductivity across the frequency spectrum by analyzing the response of dipoles and dipole moments in the material, as well as their movement, notably dielectric displacement [110]. These dipoles can be atomic, electronic, or ionic. The real and imaginary components of permittivity represent the dielectric strength and dielectric losses respectively. This analysis can identify the degree of deterioration in dielectric samples, conductors, or insulation components. Although Dielectric Spectroscopy can detect insulation degradation, which is caused by a series of phenomena such as synergic effects, dielectric relaxation, and conductive contributions to the dielectric response, it exhibits limited efficacy in detecting deficiencies like corrosion, manufacturing defects, or incipient insulation failures. Prior research has investigated the electrical insulation parameters of the stator windings, exploiting the frequency response of $\tan\delta$, PF and complex capacitance and focusing on the complex dielectric permittivity [111].

- **Impedance Spectroscopy**

Over the past two decades, the limited effectiveness of dielectric spectroscopy and the challenges in interpreting measurements have led to increased research interest in electrical impedance spectroscopy for modeling electrical insulation of various applications [112]. These include power transformers, cables, motor windings and power converter drives. It facilitates non-destructive measurements at low voltage levels to identify manufacturing flaws, material anomalies, and incipient faults. Moreover, it assists in investigating thermal, electrical and mechanical stresses, as well as evaluating the cumulative impact of multiple stresses, including environmental variables. Impedance spectroscopy evaluates the impedance characteristics of a material sample or component by measuring the amplitude and phase response across a wide frequency spectrum. It enables comprehensive analysis, while simplifying equivalent circuit analysis by representing total complex impedance in the frequency domain. This process allows impedance to be represented as a complex transfer function, or V/I function in electrical terms, and subsequently allows to determine the order of the system in electrical circuits, characterize it and assess its stability [113]. This information is presented through impedance Bode plots, which reveal details about amplitude and phase response with the electrical resonance of the components.

This method also utilizes Nyquist plots to analyze the impedance function [114]. Nyquist plots depict the trajectory of the real and imaginary components of complex impedance across the frequency sweep as a locus. The imaginary components are represented on the vertical axis, while the real components are represented on the horizontal axis. Each data point on the plot represents a specific frequency at which impedance is measured. They provide valuable insights into the behavior of the system under test. The shape of the locus can indicate the presence of certain phenomena such as capacitive or inductive behavior, or the presence of electrochemical

processes in insulating materials. A rightward shift of the Nyquist plot indicates an increase in resistance, while a leftward shift a decrease in resistance. On the other hand, a downward shift denotes an increase in capacitive reactance, thereby a decrease in capacitance, while an upward shift indicates a reduction of capacitive reactance and thereby an increase of capacitance.

3.6 Fixed Thermal Aging Test

As new and more sophisticated traction motor technologies are explored in the automotive industries, the need for more advanced insulation material compositions is evident. Different insulating materials are used, each serving a different purpose. Polyamide-imide (PAI) is among them, which primarily composes the enamel coatings on conductor wires of the motor windings. The selection of PAI over other organic-based materials like PI and PEI lies in the fact that PAI exhibits high temperature performance characteristics [115], while PEI is used in applications with lower temperatures.

Insulating materials undergo aging after a period of normal use, in which some of the properties of the material are irreversibly deteriorated. During motor operation, insulation is subjected to various stresses, which are recognized as TEAM, an abbreviation for Thermal, Electrical, Ambient and Mechanical stresses. These stresses may occur either individually as a single-factor aging when only one of them stresses the insulation or a combination of them can occur, which is more common, known as multi-factor aging [116].

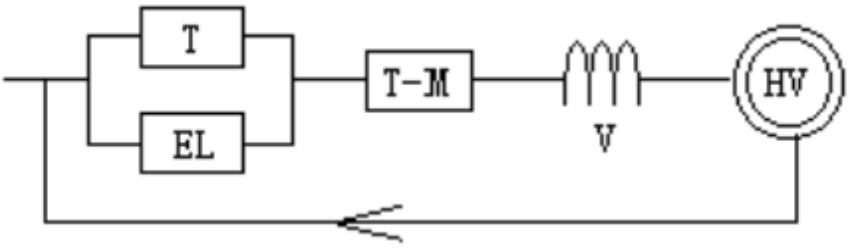

Figure 3.18: Diagram for Multistress aging test, T:Thermal, EL:Electrical, V:Vibrational, TM:Thermomechanical, HV:High-Voltage stresses [116]

Undergoing stresses can change over the lifespan of components and can manifest simultaneously or sequentially. These stresses degrade the insulation mechanisms and lead to the gradual failure of the system. Researchers are interested in evaluating the behavior and performance of insulation systems under these harsh conditions exhibited in the motor's environment. For this reason, they simulate these conditions in laboratories to subject samples of insulation components to experiments that artificially age the samples. Accelerated aging tests are very popular as they provide an effective approach to assessing the aging mechanisms of insulation systems and give better insights into the aging resistance limits of different materials. Manufacturers routinely use accelerated aging tests for several purposes, including single-factor aging and multi-factor aging techniques with the implementation of thermal, electrical, ambient and mechanical stresses. Stresses are applied at different levels, typically exceeding normal operating conditions and at a faster rate, leading to an accelerated wear and failure process within a much shorter time span, ranging from a few hours to a few days, rather than years. The application of the aging tests serves multiple purposes, including the evaluation of insulation systems, qualification procedures, development of new innovative insulating materials, and post-production acceptance testing.

In this section, there will be an overview of the previous work done in accelerated thermal aging tests, focusing on fixed thermal stresses. Thermal stresses are the main stress that deteriorates insulation systems. In particular, they are responsible for:

1. Chemical degradation reactions, including diffusion and polymerization, which lead to chemical and physical changes

2. Thermomechanical effects resulting from forces produced by thermal expansion and contraction

The main challenge in achieving a reliable prognosis is the inherent difficulty in separating the different physical mechanisms and their independent effects on insulation aging. For instance, testing insulation under electrical stress causes current to flow in the tested winding, producing heat. This heat leads to thermal degradation alongside electrical degradation. Furthermore, thermal cycling results in different mechanical expansion rates between various materials, causing mechanical stress to coexist with thermal stress. Therefore, a suitable research plan requires understanding and modeling fixed thermal stress. The next step would involve thermal cycles to distinguish the impact of mechanical expansion rates from thermal aging. Electrical testing should also be conducted independently to separate the effects of thermomechanical stress from electrical stress. The specimens tested, found in literature, are mainly stator coils or copper bars, but also many other investigations have been performed involving twisted pairs, mounted coils, motorettes and formette coils [117],[118]. Results and conclusions extracted from these investigations will be presented, obtained with different diagnostic tools.

3.6.1 Related work

The literature contains many significant contributions to accelerated thermal aging, which can be achieved through thermal cycling or fixed thermal stress. Experimental work involving thermal cycling aging is less common than that with fixed thermal stress.

The Thermal cycling (TC) technique appears as a more representative evaluation method, as it can replicate the real conditions and thereby the thermomechanical stresses found in the environment of an EV motor [119]. The samples are subjected to thermal cycles of high temperatures in specially designed ovens. The temperature does not remain constant, but instead, spans a range around a predefined value. The temperature spans and rating limits of stator windings are defined by IEEE standards, depending on the type of insulation materials. Usually an interval of 40°C is defined, but intervals of 45°C are also found in literature [120],[121],[122]. For instance, if the temperature is preset to 200°C, the thermal cycling extends from 180°C to 220°C. The purpose of this accelerated aging method is to cause the groundwall insulation to separate from the copper of the stator windings.

On the other hand, a constant thermal aging method imposes a fixed thermal stress. Fixed thermal stress simulates the consistent thermal load applied to the stator windings during normal operation. This stress typically arises from heat generated due to electrical losses, such as:

1. **Copper losses (I^2R):** Heat generated due to the resistance of the copper windings when current flows through them

2. **Iron losses:** Heat produced in the stator core due to hysteresis and eddy currents in the magnetic material

3. **Stray Load losses:** Additional losses caused by leakage flux and harmonics during motor operation

This constant heat load leads to a steady temperature rise in the windings, which must be managed through effective cooling mechanisms.

During this accelerated aging technique, samples are set up in a controlled environment where they are subjected to a constant high temperature, typically 180°C or 200°C. This setup

involves specially designed temperature-controlled ovens or chambers that can maintain a precise temperature over extended periods. The applied temperature is chosen according to the thermal limits of the insulation class and international standards, while it depends on the operating conditions of the motor as well. It is usually higher than the normal temperature that prevails during motor operation to accelerate the aging process, allowing for quicker observation of the thermal effects. Samples are continuously exposed to this fixed temperature to mimic the heat load of copper, iron losses and stray load losses. Various parameters are monitored throughout the aging process, such as insulation resistance, dielectric strength, insulation capacitance, and dissipation factor. These measurements provide valuable insights about the degradation rate and impact of thermal stress. Next, the collected data is analyzed to determine the thermal endurance of the insulation materials. This analysis identifies how the insulation properties change over time under fixed thermal stress.

An overview of completed research on fixed thermal aging technique follows, presenting parts of the test procedures followed and the results they led to. Generally, the resistance of winding insulation material is investigated. Different specimens of windings insulation coating materials are used as test samples, including rectangular copper wire [123]. These are divided into groups and each of them has been aged in different but identical ovens at specified fixed temperatures and for different time periods. Insulation coatings consist of an inner PEI layer and an outer PAI layer and typical aging temperatures are at 200°C, 215°C, 230°C, 245°C and for 100, 200, 400, 800, and 1600 hours. In [124], [125] and [126], the dielectric properties of coating copper wires with PAI insulation material are investigated. This time, samples were aged under 6 different temperatures set at 6 identical ovens, 200°C, 215°C, 230°C, 245°C, 260°C and 275°C for 100, 200, 400, 800 and 1600 hours respectively. [127] and [128] define a threshold of 230°C and categorize the impact of temperatures below or above this value on the PAI insulation. Other contributions [109] suggested the exposure of concentrated coils (Fig. 3.19b) to cycles of 100 hours maintaining only one constant temperature of (200°C). Following each thermal cycle, the samples were removed from the oven and left to cool down at ambient temperature and humidity conditions. The entire process, encompassing thermal exposure, cooling, and measurement, was iterated until a cumulative aging time of 1400 hours was achieved. Generally, impedance spectroscopy was used as the main diagnostic technique to assess the deterioration process of the insulation of the windings before and after each thermal cycle. In [129] thermocouples and thermal sensors were employed to continuously monitor the temperatures, creating a thermal profile of the samples via thermography.

(a) Samples inside the oven [123] (b) Concentrated coils as test samples[109]

Figure 3.19

3.6.2 Impact of fixed thermal aging

In all cases, some populations of specimens have remained unaged for comparison purposes with the aged specimens after the applied aging techniques. The main method for assessing the insulation condition was the application of high breakdown voltage between the thermal cycles on the samples. Significant outcomes of these measurements were extracted depending on the insulation resistance, dissipation factor, capacitance, partial discharges, and lifetime of the insulating materials.

(I) **Insulation Resistance & Thermal Conductivity:**

The analysis in [123], [124], [118] and [130] revealed that the thermal degradation appeared to be driving the resistive characteristics of the thin-film insulating materials towards a more homogenized state. As expected, a general decrease in insulation resistance as a function of temperature for each aging period was observed. However, this decrease does not exhibit a logarithmic trend but a relatively slow rate of change throughout the aging cycles. This observation suggests a low decomposition rate for the bonding materials within the insulation systems. Furthermore, the resistance does not display a monotonic relationship with aging time when the thermal stress is held constant. Figure 3.20 exhibits the dependency of IR on the increasing temperatures and aging period.

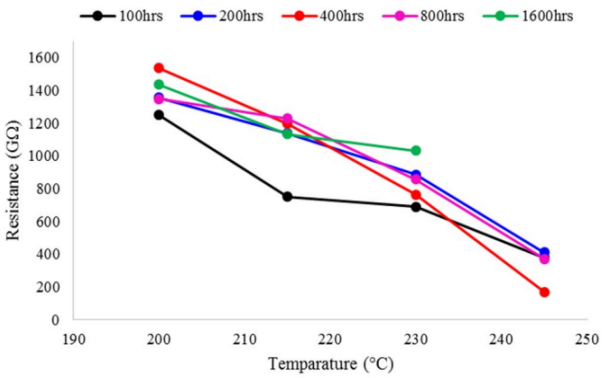

Figure 3.20: Thin-film insulating material maximum IR dependency on the aging time and temperature [123]

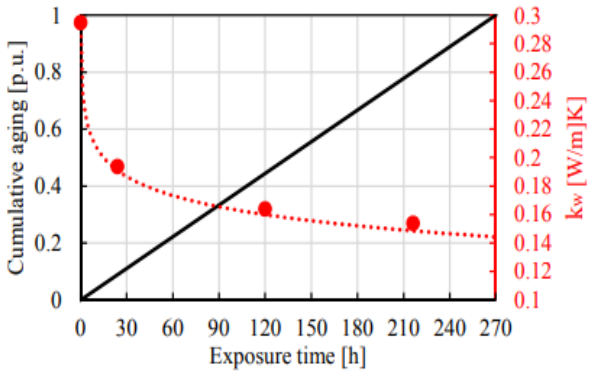

Figure 3.21: The dependency of winding thermal conductivity on cumulative aging time at 230°C [129]

[131] and [129] revealed that the dielectric and physical properties of the insulation system were strongly influenced by thermal aging, referring to the thermal behavior of the motorettes. The steady-state hot-spot temperature within the windings increased with the cumulative aging time. This was ascribed to the thermal conductivity alteration of the wire enamel and impregnating resin due to thermal aging. The variation of the thermal conductivity k_w is displayed in Fig. 3.21. The intersection of the cumulative aging linear plot (black) with the y-axis, where the cumulative damage is $1p.u.$, enables the identification of the end-of-life point, which is 270 hours at 230°C. It is clear that k_w has dropped to 0.16 W/m/K at almost half of the life from the initial unaged value of 0.3 W/m/K. Thermal conductivity follows an exponentially decreasing slope with the aging exposure time, while the failure probability increases inversely with the increasing temperatures.

(II) **Dissipation Factor:**

[132] indicated a variation of the dissipation factor and power factor between low and high frequencies. Below 1Hz both DF and PF exhibit high initial values, which are progressively decreased and finally stabilized at 0.01 at 100Hz. As a group of laminated specimens

was subjected to constant thermal stress at 200°C for 1000 hours, tanδ increased from 0.2-0.3 to ≈1 at very low frequencies (around 0.01Hz). Similarly to the unaged samples, the tanδ gradually decreases as the frequency increases. At high frequencies above 100Hz, there is no difference between the thermally ages samples and the healthy ones. When the aging period was doubled, a significant loss in the dielectric was observed, ascribed by the increment of tanδ at low frequencies. Cosϕ of the thermally aged samples exhibited a similar trend, with its initial values being much higher compared to the healthy samples.

[118] highlighted the dependence of the dissipation factor on the applied test voltage. The initial aging cycle resulted in a shift in the response of the DF at all voltages, affected by the insulation drying and post curing. Moreover, thermal aging caused an increase in the initial value of the DF (low voltage tanδ). This parameter reflected the combined effect of the polarisation and conducting losses within the insulation. This increase is attributed to the chemical reactions of the organic materials of the insulating materials triggered by the thermal stress, which involve the scission of high-weight epoxy molecules, leading to the formation of lower-weight molecule species. Since these molecules are typically more polar, they contribute to more dielectric losses. An increase in moisture within the insulation also elevates the initial value of DF. As aging cycles progress, tanδ elevated with increasing test voltage (Fig. 3.22b). This is due to delamination forming within the bulk insulation or at the copper conductor interfaces caused by thermal stress. The progressive aging cycles contributed to the development of more air-filled voids and delaminations within the insulating material. These defects promoted increased partial discharge activity and consequently, higher ionization losses.

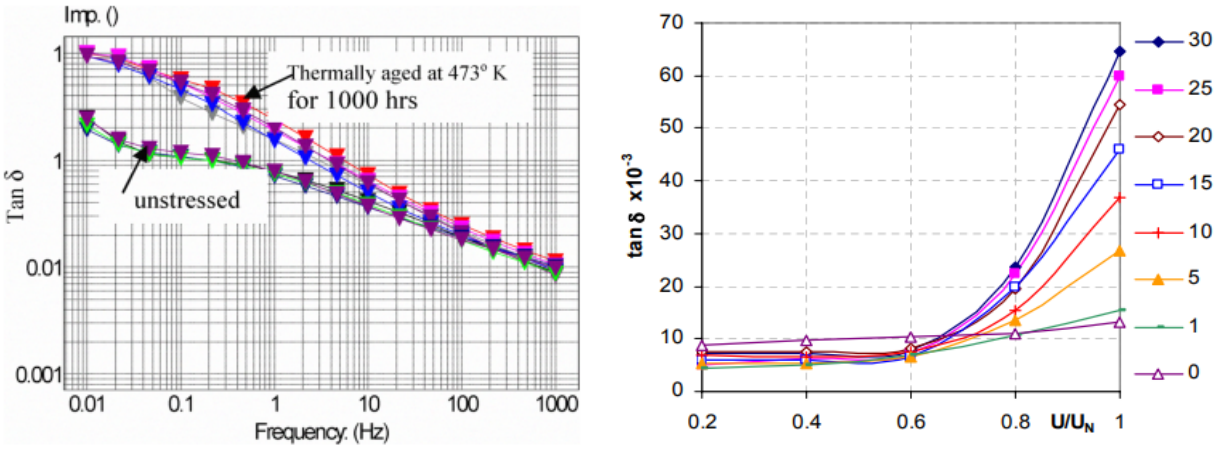

(a) Tanδ vs frequency on unaged and aged samples at 200°C [132]

(b) Tanδ vs test voltage with increasing number of aging cycles [118]

Figure 3.22: Dissipation factor affected by fixed thermal stresses

(III) **Capacitance:**

[125] suggested that capacitance might not be an appropriate tool for reliable prognosis. The statistical analysis of the capacitance values of the aged samples showed that these values spread and scattered during thermal stress for long aging periods. At 200°C, 215°C and 230°C the capacitance first increased and then dropped to initial values, while at 245°C and 260°C the opposite trend occurred, thus no monotonic pattern was provided.

In [118] two primary changes in the capacitance characteristics were observed due to thermal aging, including a decrease in the initial capacitance value and an amplified reliance on voltage. These alterations are linked to the formation of delaminations within the

insulation and the subsequent partial discharge activity within these delaminations. At low voltage, the overall capacitance represented the combined capacitance of the solid insulation with the air-filled voids. However, at high voltages, the partial discharge activity effectively shorted out the air voids, resulting in a measured capacitance that reflected only the solid insulation.

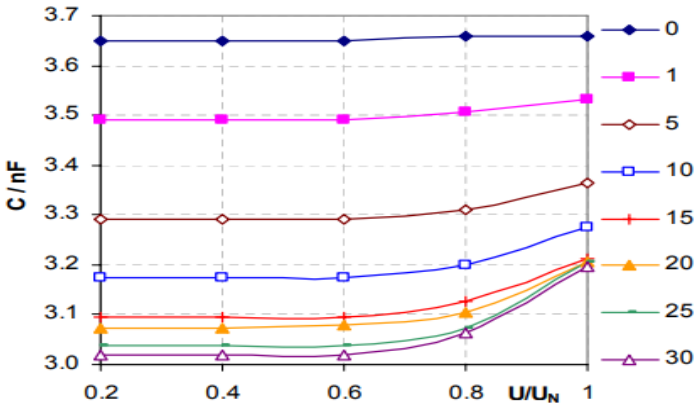

Figure 3.23: Capacitance vs test voltage with increasing number of aging cycles [118]

(IV) **DF Tip-Up and ΔC:**

The Dissipation Factor Tip-Up and Capacitance Tip-Up increased as the number of aging cycles grew. A minimal change in DF from cycle to cycle suggests a reduction in the formation of air-filled voids and delaminations. Conversely, a progressively increasing change in DF signifies a rise in energy consumption due to the increased occurrence of partial discharges.

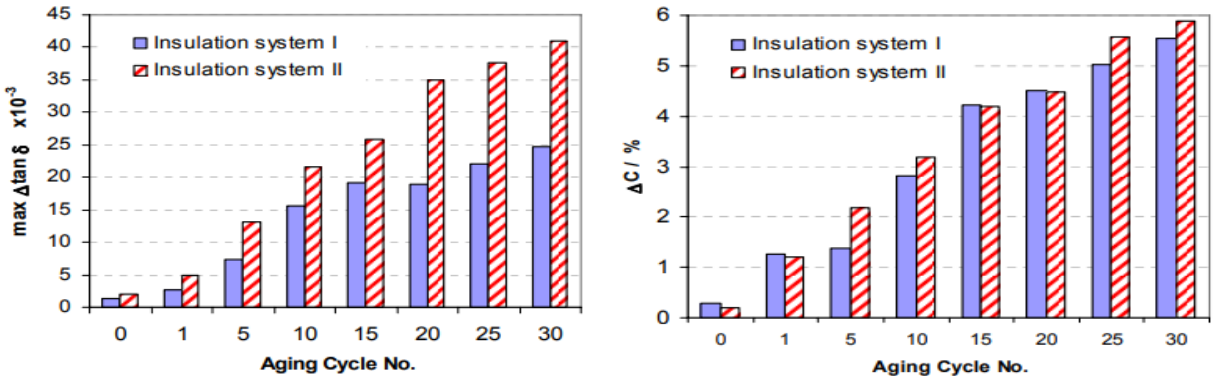

(a) Change of $\Delta\tan\delta$ with increasing aging cycles (b) Change of ΔC with increasing aging cycles

Figure 3.24: $\Delta\tan\delta$ and ΔC of 2 distinct insulation systems affected by fixed thermal stress[118]

(V) **Partial Discharges:**

Partial Discharge measurements demonstrated a high degree of sensitivity in changes in insulation systems during constant thermal aging process [118]. The symmetrical PD patterns observed in both positive and negative half cycles suggest that the discharges predominantly occurred within coil-to-core insulation. Furthermore, an overall increase in partial discharge activity is evident with increasing aging cycles, compared to the unaged state. After a certain number of cycles, the magnitude of the highest PD pulses relatively stabilized. As the aging progresses, the number of low-amplitude discharges notably decreased, whereas the "hollow" of the PD pattern expanded within the phase

range of 0° to 90° and 180° to 270°, indicating an increase of the number of discharges with higher amplitude. This change may be attributed to the growth of small voids as the aging process develops.

The increase in PD activities is mainly due to the formation of delaminations within the bulk insulation. These arose from the differing thermal expansion coefficients of steel, copper, and the mica-epoxy composite. The ongoing aging process further exacerbated this phenomenon by altering the characteristics of epoxy resin. Consequently, delaminations developed within the main insulation or at the interfaces between the copper conductors and the main insulation. As aging progressed, the magnitude and density of partial discharges generally rose significantly, indicating an increase in the number and size of voids, and subsequently, deterioration within insulation.

A general increase in both the number of PD pulses and the transferred charge per second for two different insulation systems with increasing aging cycles is illustrated in Figure 3.25. After a certain point, the number of PD pulses per second is stabilized, reaching a relatively constant value. This suggests that the number of discharge sites in the insulation likely increases during the initial aging cycles and then stabilizes. The total transferred charge per second also exhibits a rapid rise in the early stages of aging. As aging cycles increase, the total charge can either progressively increase or remain roughly stable.

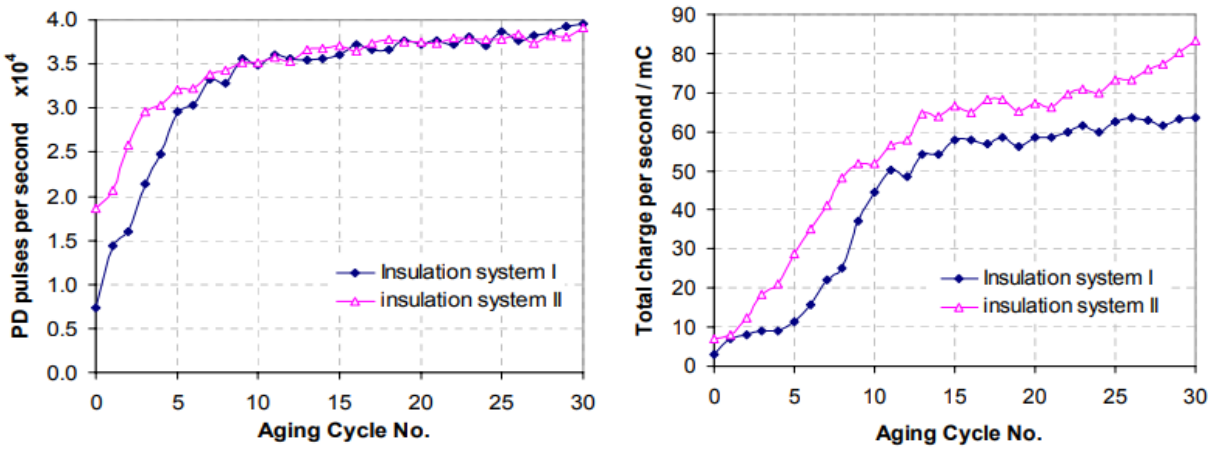

(a) Change of the number of PD pulses per second with increasing aging cycles

(b) Change of the total transferred charge per second with increasing aging cycles

Figure 3.25: Partial Discharge activity for two distinct insulation systems affected by fixed thermal stresses [118]

(VI) **Lifetime:**

The findings demonstrated a non-monotonic trend in the electrical properties of the insulation material when subjected to high constant thermal stress [123]. This observation challenges the applicability of the well-established Arrhenius law [133] for modeling such degradation and predicting the remaining useful life (RUL) of thin-film insulation materials. Thus, the Arrhenius model has to be expanded.

The visual inspection of the aged samples revealed two distinct aging mechanisms based on the temperature applied [124]. At lower temperatures, a slower degradation process was observed, as the material aged gradually. This manifested as bubble formation on the conductor's surface, followed by a characteristic zigzag cracking pattern in the insulation. Interestingly, this phenomenon was absent in samples aged at 275°C. At this higher temperature, the insulation underwent rapid degradation, resulting in the complete removal

of the insulating material and exposing localized areas of the bare copper conductor. The two distinct aging mechanisms are depicted in Figures 3.26a and 3.26b respectively.

[127] [128] showed a decrease in the lifetime of the insulation materials, as the constant thermal stress increased and the aging period expanded. Similar observations were extracted from almost all investigations. Particularly, when the upper rated limit of the insulation class was exceeded, the dielectric properties of the insulating materials degraded at a faster rate. As the temperature increases a smaller population of samples withstand the corresponding aging profile. In [134], a substantial proportion ($\geq 50\%$) of the samples exposed to 230°C for 1600 hours exhibited catastrophic failure. At 245°C and the same exposure time, no samples survived. Furthermore, at 200°C and 800 hours, two samples experienced catastrophic failure, whereas this number increased to four at 245°C for the same duration. Moreover, less than 20% of the samples survived at 260°C and almost 11% at 275°C at early aging periods. When the aging period exceeded beyond that time, none of the samples survived. The PAI material was totally destroyed and stripped of the conductive parts, leading to a complete failure of the insulation systems.

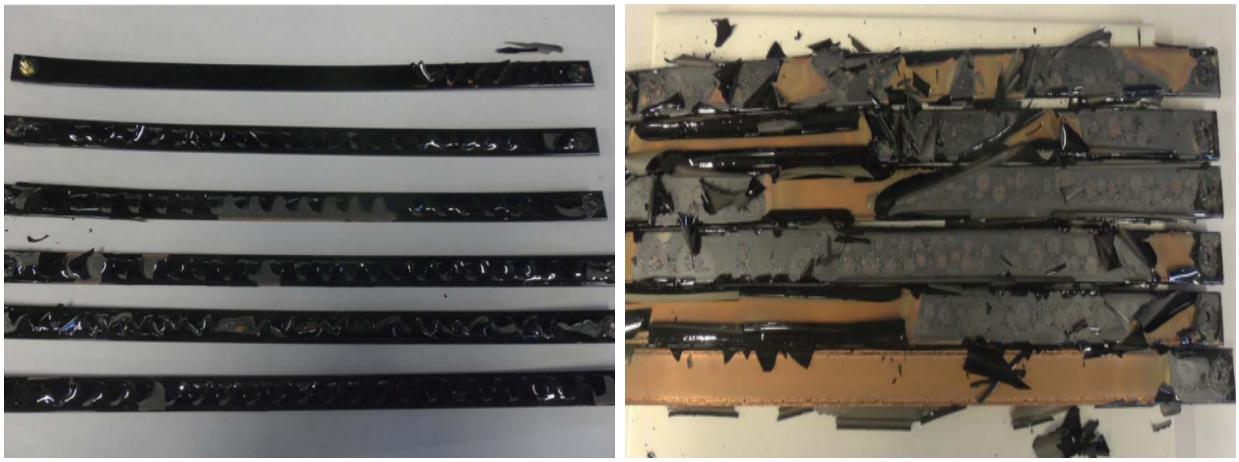

(a) Zigzag-shaped crack of insulation material (b) Catastrophic failure of insulation material

Figure 3.26: Insulation failure at 260°C for 800 and 1600 hours respectively[124]

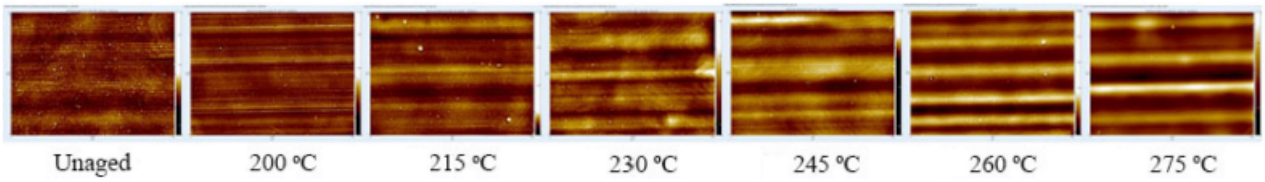

Figure 3.27: Measured surface profile at various temperatures for the early onset aging period of 100 hours [134]

The measured surface profile of thin-film insulation materials (PAI and PEI) is shown in Fig. 3.27. Visual examination of the unaged samples revealed a relatively smooth surface characterized by subtle horizontal striations aligned with the direction of insulation extrusion, a signature of the coating process. Notably, these striations became progressively broader and more accentuated with increasing thermal aging exposure temperature [134]. In addition, the mass of the samples was decreasing with increasing temperatures.

(VII) **Breakdown Voltage:**

The decrease in resistance translates to a higher current flow through the thin-film insulation [123]. To investigate the relationship between current increase and the applied

thermal stress during breakdown, the resistance values both before and at the breakdown are crucial. The normalized current increase α is:

$$\alpha = \frac{\Delta I}{I_0} = \frac{I_{EBV} - I_0}{I_0} = \frac{R_{EBV} - R_0}{R_0} \tag{3.25}$$

where $V_0 = R_0 \cdot I_0$, $V_{EBV} = R_{EBV} \cdot I_{EBV}$ and $V_0 \approx V_{EBV}$.
A consistent trend was revealed. As the aging temperature increased, both the leakage current at breakdown and the resistance at breakdown I_{EBV} and R_{EBV} respectively exhibited a decrease. Consequently, this reduction in resistance resulted in a corresponding decrease of the breakdown current difference required to break the insulation over time, signifying degradation of the magnet wire [134]. This monotonic aging trend was observed consistently across all four aging temperature profiles investigated.

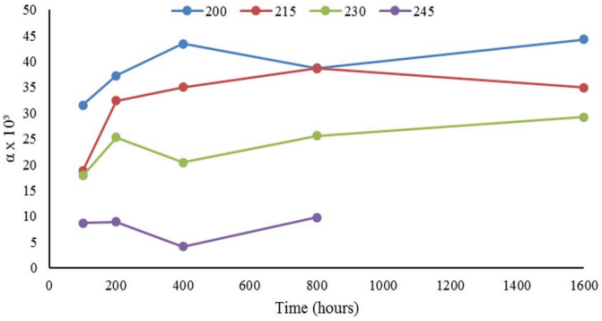

(a) The dependency of α on the applied fixed thermal stress [123]

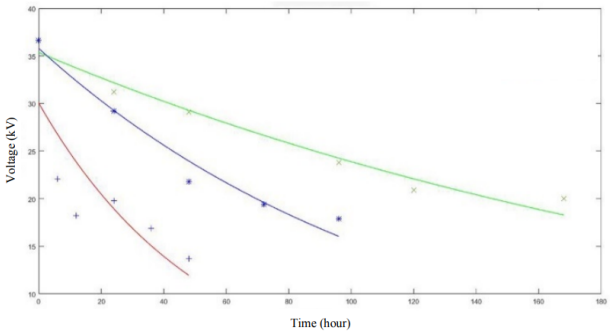

(b) The trend of breakdown voltage decreasing with increased applied temperature [133] (green:100°C, blue:115°C, red:125°C)

Figure 3.28: Breakdown voltage impact

Moreover, between the aging cycles the measurements from the corresponding early breakdown voltage test showed a reduction of the voltage in which the breakdown of the insulation occurred. The reduction of the breakdown voltage is emphasized in Fig. 3.28b, in which the reduction increases as both the aging time and temperatures are higher.

4 Megger user manual

For the purposes of achieving certain diagnostic tests, the MIT1525 15kV diagnostic insulation resistance tester, an instrument developed by Megger, was used. This instrument serves as a compact tester for the diagnostic testing and maintenance of high-voltage electrical equipment. In our case, it was used to stress the pole insulation of a yokeless and segmented armature axial flux motor for the TEAMstress project. This section provides a user manual for the aforementioned instrument, describing the basic operations of the instrument as well as the test procedures that can be performed.

4.1 Instrument description

The Megger MIT1525 is the flagship unit in Megger's MIT series of insulation resistance testers. The series also includes the MIT515, MIT525, and MIT1025, but these instruments can only go up to 5kV and 10kV respectively, as the first digit in their name suggests. The main diagnostic technique that the unit can perform is insulation resistance tests up to 15kV with a 30 teraohm ($T\Omega$) maximum resistance and an accuracy of $\pm$ 5% from 1 $M\Omega$ up to 3$T\Omega$. The MIT1525 tester includes a full range of test modes including Insulation Resistance (IR), Timed IR, Dielectric Absorption Ratio (DAR), Step Voltage (SV), Polarization Index (PI) and ramp diagnostic tests. The unit includes an internal memory that records data every 5 seconds while in operation, for a maximum duration of 5.5 hours. Users can also choose to transfer this data to a computer using an integrated USB port and visualize them via the installed software application PowerDB. Its safety is rated up to CAT IV 1000V to 3000m altitude, following the requirements of IEC 61010-1. The short circuit output current is rated at 3mA and the maximum noise rejection is at 6mA.

Figure 4.1: Megger MIT1525 15kV instrument

In Figure 4.1, the Megger MIT1525 15kV instrument is displayed with two cables connected at the two terminals. As it can be easily viewed, the instrument consists of some buttons, rotatory switches and a large LCD screen with back-light that facilitate control and operational adjustments. The instrument is placed inside a sturdy and waterproof case that protects it from

noises, humidity and dust, factors that affect the sensitivity of measurements, or damage in case of falling. Also, a lightweight Li-on battery is placed inside the instrument which enables wireless operation and is charged with a specialized charger plugged in a socket. In Figure 4.2, there are some arrows used as indicators to explain the role of each button and rotatory switch, as shown in Table 4.1.

Figure 4.2: Instrument indications

Number	Description
1	Positive Terminal (+)
2	GUARD Terminal
3	Negative terminal (-)
4	LCD Display Screen
5	Four Arrow Buttons and OK
6	Test Mode Rotatory Switch
7	Save button
8	Back-light
9	TEST button with associated warning lamp for High Voltage
10	Central Rotatory Switch
11	USB Device Interface
12	LED indicating line power/mains
13	Functional Earth Terminal
14	Power socket

Table 4.1: List of instrument indicators based on the Figure 4.2

The LCD screen of MIT1025 is shown in the Image 4.3 below. It provides similar if not the same icons as the MIT1525 unit, involving features for voltage values and insulation resistance measurements, icons for timer, storing and accessing data, alarm, warning signals, battery condition and other modes. The icons are listed in Figure 4.4.

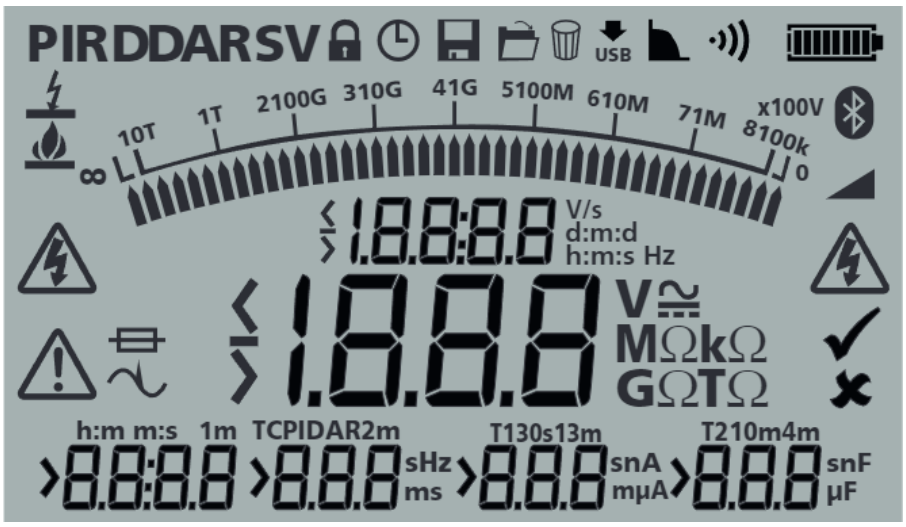

Figure 4.3: The LCD Display Screen of the instrument with its icons

Icon	Description	Icon	Description
V	User lock voltage		Delete records
	Timer	USB	Download via USB
	Save		Filter
	Open records		Alarm
	Battery		Breakdown mode
	Ramp test		Burn mode
	Danger HV		Refer to manual
	Fuse		Noise detected

Figure 4.4: The icons of the screen with their description

The control of the MIT1525 IR Tester is primarily achieved by the two rotary switches and the TEST button, shown in 4.5. The TEST button is used to start and stop a test. The main rotary switch includes an "OFF" setting. The device activates by rotating the switch either clockwise or counterclockwise from this position. Various test voltage options are provided for IR tests up to 15kV. Additionally, users can select a custom voltage range, which can be adjusted between 500V and 15000V. The "lockable" test voltage range can be modified in the settings function.

The settings function, marked by a spanner symbol, allows users to manage various functions such as lock voltage, low resistance alarm, temperature, and time/date adjustment. A light blue colored segment on the rotary switch indicates memory-related functions that include accessing saved records, downloading via USB and deleting records. Also, a save button to store records within the memory of the device and a back-light button are incorporated.

A second rotary switch is responsible for controlling the insulation test mode, offering various tests. From left to right in 4.5, the tests that can be set are the basic insulation resistance (IR), timed insulation resistance IR(t), Dielectric Absorption Ratio (DAR), Polarization Index (PI), Dielectric Discharge (DD), Step Voltage (SV) and ramp test.

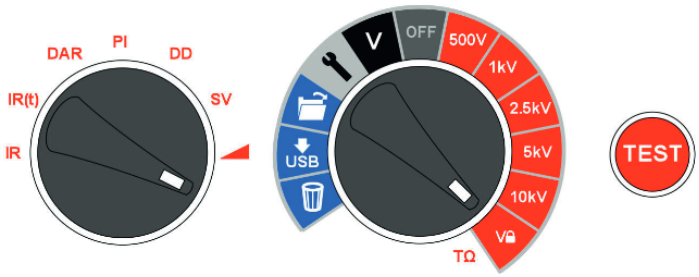

Figure 4.5: The primary elements for control

A set of directional buttons and an OK button are utilized for settings and memory functions. The up/down arrows also allow for adjustments of the test voltage during testing. Before the start of an IR or IR(t) test, burn mode can be activated by holding down the left arrow button with a selected voltage level on the main rotary switch. Burn mode is deactivated upon changing the voltage range or mode or by pressing the right arrow, which can also be used as the breakdown button. In breakdown mode insulation tests stop automatically and indicate "Brd" on the display screen if a fault causes a rapid decrease in the applied voltage. Conversely, breakdown events in burn mode IR tests are disregarded, allowing the insulation tests to proceed despite faults, making these tests destructive. Burn mode is deliberately used to induce carbon track in the insulation to aid in fault identification. It is noted that burn mode only operates at test voltages of 500V or higher. Backlight and Save buttons provide light on the LCD screen and save data records respectively.

The instrument is equipped with an incorporated voltmeter capable of measuring AC/DC voltage within the range of 30V to 660V. For AC voltages, the frequency is measured in Hz and displayed accordingly. The voltmeter mode is activated by switching to 'V' mode in the main rotary switch. For the voltmeter function, clamps, like those depicted in Figure 4.7, are connected to the positive and negative terminals of the device. GUARD terminal is not proper for use in voltmeter mode. As a safety precaution, the instrument automatically transitions to voltmeter mode when detecting a voltage of 50V or higher connected to the terminals. The measured voltage will be displayed on the screen, accompanied by an intermittent beeper to alert the user to dangerous voltage levels.

Figure 4.6: Elements for adjustments and settings

Figure 4.7: Clamps to be connected to the terminals and a USB cable

4.2 Instrument control and setup

For proper control of the device, it is necessary to set the Real Time Clock (RTC). The RTC guarantees accurate time/date stamping of records stored in the instrument and is equipped with a separate battery, ensuring that settings are preserved even when the main battery is removed. The date and clock are adjusted by accessing the settings function on the central rotary switch and switching the mode rotary switch to IR. The left and right arrows are used to navigate to the time and date display. Time can be set by the up and down arrows, changing the minutes and hours, and when set, the time is saved by pressing the OK button. The day and month are set by selecting the appropriate format. The right arrow is pressed to adjust the date and then the OK button to save it. A checkmark on the left side of the display screen signifies that a setting has been saved, while a cross displayed during adjustment means that it has not been set. To exit settings, switch the central rotary switch to a different position. Figures 4.8 and 4.9 illustrate the proper adjustments done for the correct time and date of the Real Time Clock. In 4.9a the format h:m stands for hours and minutes, while in 4.9b the format d:m stands for days and months respectively.

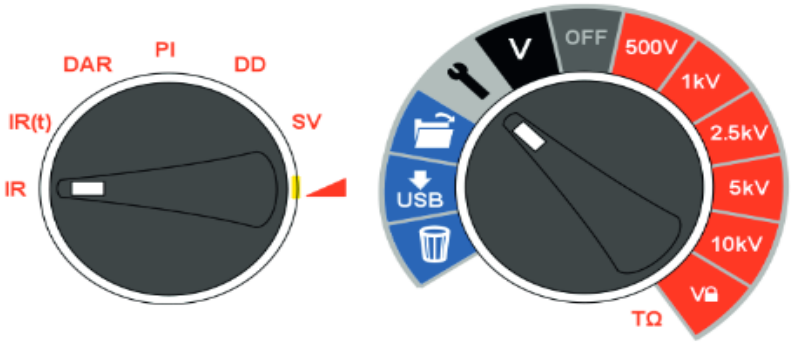

Figure 4.8: The rotary switches adjustments for RTC setup

(a) Adjustments for time setup

(b) Adjustments for date setup

Figure 4.9: Setup for clock adjustments

The up and down arrow buttons can adjust the desired voltage displayed for the user-selectable "lock" voltage range. Then this setting is saved by pressing the OK button, which will remain unchanged even if the instrument is switched off.

When the alarm has been set and activated, a low-resistance alarm will sound as the resistance level of the insulator triggers it. The default alarm setting is $500k\Omega$ and is shown on the right side of the screen if it is active or not. The low resistance alarm is set by rotating the mode and main rotary switches to the IR and settings positions respectively and then pressing the right arrow button once. Users can set the low-resistance alarm back to the default value by pressing the OK button or change it to a different alarm resistance level with the up and down arrow buttons and save it with the OK button.

The left and right arrow buttons switch between burn and breakdown modes when a voltage range is chosen in IR and IR(t) test modes respectively. Pressing and holding the left arrow activates the burn mode, while the same process involving the right arrow activates the breakdown mode. In breakdown mode, the test will automatically stop and indicate "Brd" once it detects a fault to protect the insulation from damage. In contrast, burn mode deactivates the standard breakdown detection, allowing the test voltage to continue even after insulation breakdown. This facilitates the identification of failure locations but entails a destructive test. To protect against potential damage, the unit emits two long beeps when initiating a test with burn mode activated. Figure 4.10 depicts the breakdown indication displayed on the screen and the arrow buttons used to activate each mode.

(a) "Brd" indication on the LCD screen

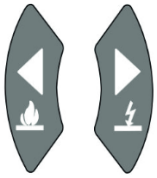

(b) Left and arrow buttons for burn and brd mode

Figure 4.10: Breakdown/ burn mode in IR & IR(t) test modes

4.3 Test procedure

First of all, it is important to mention that to run an insulation test, the insulation must be fully discharged before the execution of the test. When connecting the test leads before starting a test, any voltages of 50V or higher will be displayed on the screen, accompanied by an intermittent beeping sound. If electrical noise is present, it will induce a current through the instrument's internal discharge resistors. If this current surpasses the instrument's rating, it could damage the instrument. That is why MIT1525 is designed to withstand high noise currents up to 6 mA. Any detection of a current exceeding 6 mA will trigger an urgent 'warble' tone from the instrument, accompanied by the symbols ⚠ ∿. The instrument will not allow a test to start if the induced voltage is above 6 mA for safety reasons. Moreover, it is imperative to promptly disconnect the instrument from the power supply after discharging the DC voltage, all while adhering to Safe Working Practices.

Tests can be applied to stator and rotor windings on synchronous and asynchronous AC motors, poles of permanent magnet motors, copper bars and generally conducting elements

with insulation layers. Tests are started by pressing and holding the red button 'TEST' for approximately 3 seconds. A timer will appear to show the elapsed time during the test. The test is stopped by pressing the TEST button. While the test is stopped the insulator will automatically discharge. An indication of 'StP' will alert the user that the test terminates and after a few seconds, the voltage on the terminals will be shown. The left and right arrow buttons can be used to navigate between the terminal voltage, the last test voltage and the set range voltage. If the terminal voltage is $\geq 50V$, the voltage will be shown on the display screen with a warning. The LCD screen displays the final values of resistance, capacitance, test current and Time Constant (TC) with test duration time.

The test voltage can be adjusted either before or during the test, using the up and down arrow buttons. It is preferable to adjust the voltage in the first 10 seconds after the start of the test, to avoid interference with the capacitive and absorption currents of the insulator. Furthermore, the LED and display warnings must be turned off before disconnecting the instrument leads or clamps. This indicates that the unit under test has been fully discharged. Capacitors or inductors, which are reactive loads, can store significant currents that can pose a lethal hazard.

4.3.1 Insulation resistance test

Insulation Resistance (IR) or spot IR test is the most famous test for this instrument. The test is applied for a short and specific duration of time and then a reading is recorded. This reading can be compared with the minimum installation specifications. Tracking this value over time and comparing it against previously recorded measurements is recommended, unless the result is exceptionally low, indicating potential issues.

Each test mode is selected on the test mode rotary switch. Rotating the switch to the IR position sets an IR test. The desired test voltage is chosen using the preconfigured voltage ranges on the red segments of the main rotary switch or the user lockable voltage range. While all preconfigured voltage ranges are adjustable using the up and down arrow buttons before and during the test, the settable voltage range setting should be restricted to the first 10 seconds of IR and IR(t) tests. The test will start by pressing and holding the TEST button.

The user-defined lockable voltage is configured by rotating the main rotary switch to the settings position and the mode switch to IR, as shown in Fig.4.11a. The default voltage setting of 5000V will flash, but it can be adjusted using the up and down buttons. Once the desired maximum voltage is displayed, the setting can be saved by pressing the OK button and will remain until it is modified again. Whenever this setting is selected, the set voltage will be visible on the display screen. The voltage lock feature is beneficial, especially when testing the insulation of XLPE cables, ensuring that the test voltage does not surpass the specified limit, such as 5000V. This lock function guarantees that the output voltage remains within the stated accuracy limits. Upon completion of the test, the insulation capacitance C and its associated time constant TC are calculated and displayed.

The Time Constant TC is expressed as the product of the insulation resistance with the insulation capacitance:

$$TC = R_{ins} \times C_{ins} \tag{4.1}$$

A timed insulation resistance IR(t) test measures the insulation resistance, but with the difference that it automatically terminates the test after a preset duration. The timer is set by default to 1 minute and can be adjusted within the settings function. This feature eliminates the need for the user to continuously monitor the display throughout the full duration of the test and the risk of missing the reading at the 1-minute mark.

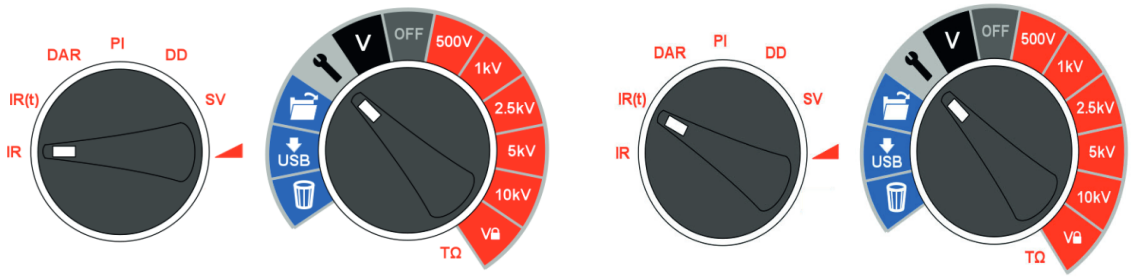

(a) IR test mode

(b) Timed IR test mode

Figure 4.11: Insulation resistance tests modes

If the timer needs to be adjusted, the main rotary switch must be rotated to the settings position and the mode rotary switch to the IR(t) mode, as shown in Fig.4.11b. The default time setting of 1 minute will flash, prompting the user to adjust the duration using the up and down arrow buttons. By pressing the OK button the test duration is set and then the main rotary switch must be rotated to select the desired test voltage. Finally, the test will be started by pressing and holding the TEST button.

4.3.2 DAR and PI tests

The Dielectric Absorption Ratio (DAR) and Polarization Index (PI) tests are resistance measurements over time in which two resistance values at different times are expressed as a ratio. The resistance measured at time t2 is divided by the resistance at time t1. According to the IEEE Standard 43-2000 [83], PI is defined as the ratio of insulation resistance at 10 minutes divided by the insulation resistance at 1 minute:

$$PI = \frac{IR_{10}}{IR_1} \tag{4.2}$$

If IR_1 is greater than $5000M\Omega$ the PI may or may not be a good indication of insulation condition. Thus, for these values, PI is not recommended by IEEE std. 43. Table 4.2 shows the importance of different PI values as diagnostic information about insulation conditions. When the condition of the insulation is characterized as "good", the leakage current tends to be small and resistance steadily increases as the current decreases due to charging and dielectric absorption effects. Typically, a low ratio suggests minimal change and thereby "poor" insulation, while a high ratio implies the opposite.

Insulation Condition	PI value
Poor	< 1
Questionable	1 - 2
Acceptable	2 - 4
Good	> 4

Table 4.2: PI values showing their diagnostic information about insulation condition

During a DAR test, the times t1 and t2 are chosen differently. The concept is to take successive readings at specified times during a single test. DAR is defined as the ratio of insulation resistance measured at 1 minute divided by the insulation resistance at 30 seconds, although the division with a 15-second measurement is also popular.

$$DAR = \frac{IR_{60s}}{IR_{30s}} \tag{4.3}$$

The test relies on the comparison of leakage and absorption currents between clean and dry insulation with those in moisture or contamination. In good insulation, resistance continuously increases. However, in contaminated insulation, the leakage current is significantly higher, making the effects of the absorption current less noticeable. Similarly, table 4.2 indicates the diagnostic information about insulation conditions provided by different DAR values.

Insulation Condition	DAR value
Poor	< 1
Acceptable	1 - 1.4
Excellent	1.4 - 1.6

Table 4.3: DAR values showing their diagnostic information about insulation condition

Timers t1 and t2 for DAR and PI tests are set from the settings position of the central rotary switch as long as the test mode rotary switch is rotated to the DAR or PI position. First, timer t1 will be set followed by timer t2. The default values of t1 and t2 can be adjusted by using the up and down arrow buttons and then each setting can be confirmed with the OK button. DAR and PI insulation test voltages are selected on the central rotary switch by aligning it with the desired voltage setting. A DAR or PI test will begin once pressing and holding the TEST button.

It is worth noting that DAR or PI measurements are temperature-independent as the insulation temperature should not change throughout the tests. The maximum allowed temperature is 40°C.

4.3.3 Dielectric Discharge test

The Dielectric Discharge (DD) test, also known as re-absorption current, measures the current flowing during the discharge of the test dielectric sample, in contrast to the other test modes that measure current during the charging process. DD enables aging, deterioration and voids of the insulation to be assessed. Since insulation systems consist of multiple layers, each characterized by its own capacitance and leakage resistance, this test can detect a faulty layer between healthy layers. The leakage resistance of this layer will decrease while capacitance likely remains unchanged. A conventional insulation test typically reflects the condition of the intact layers and may not detect this issue. However, during dielectric discharge testing, the time constant of the faulty layer will differ from the others, resulting in a higher DD value.

First, the insulator needs to be adequately charged until it reaches stability, meaning both charging and polarization processes are complete and only leakage current remains due to the insulation. During discharge, the capacitive component of the discharge current decreases rapidly from a high level with a short time constant, usually a few seconds. Conversely, the released absorption current decreases from a lower level with a higher time constant, spanning several minutes.

By default, the DD timer is set to a 30-minute charging period, sufficient for complete absorption within the insulating material. The default test voltage is 500V so the main rotary switch must be set at or above this voltage level. The default duration t1 consists of a 30-minute insulation test followed by a fixed 1-minute discharge phase. While the initial 30-minute period can be adjusted, ensuring that the insulation undergoes complete absorption during this test interval is essential. Figure 4.12 shows the configurations for the DD test. DD must be selected on the mode rotary switch and settings on the main rotary switch. Timer t1 can be set using the up and down arrow buttons and then is confirmed by pressing the OK button.

The instrument measures the discharge current one minute after the test voltage is removed, a timeframe that exceeds the primary time constant of the discharge. When the test

is completed, the instrument uses this measurement along with the test voltage and calculated capacitance to produce a metric indicating the quality of the insulation, expressed as:

$$DD = \frac{I_1}{V \times C} \tag{4.4}$$

where I_1 is the discharge current in mA one minute after the removal of the test voltage V in V (Volts) and C is the insulation capacitance in F (Farads)

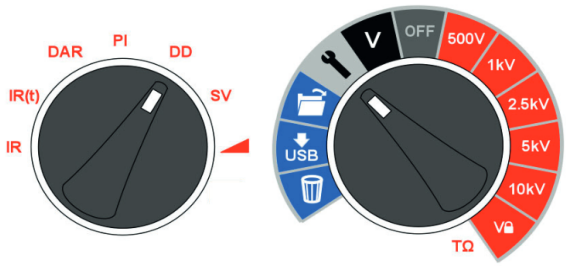

Figure 4.12: Dielectric Discharge test mode

DD results identify excess discharge currents, which occur when a layer within a multi-layer insulation is worn out or contaminated. If an internal layer is damaged, the discharge current will be higher, for a given constant voltage and capacitance. The mismatch in the time constant of this individual layer compared to the others results in a higher current value than that of intact insulation layers. Table 4.4 reflects the insulation condition according to DD test values. Good multi-layer insulation exhibits values of up to 2, while homogeneous insulation yields a DD value of 0.

Insulation Condition	DD value
Bad	> 7
Poor	4 - 7
Questionable	2 - 4
Good	< 2
Homogeneous	0

Table 4.4: DD values providing diagnostic information about insulation condition

4.3.4 Breakdown Step Voltage test

The Step Voltage (SV) test is a controlled overvoltage test, which relies on the fact that an ideal insulator will yield consistent readings across all voltage levels. Conversely, an insulator under stress will show lower insulation values at higher voltage levels. Since good insulation is resistive, an increase in voltage will result in a proportional increase in current, maintaining a constant resistance value. Any deviation from this may indicate defective insulation. These defects might go unnoticed at lower test voltages, such as 500V or 1000V. However, as voltage increases, ionization can occur within cracks or cavities, resulting in an increase in current and a corresponding decrease in insulation resistance. A recognized standard procedure involves increasing the voltage in five equal steps at one-minute intervals and recording the final insulation resistance at each level.

Figure 4.13 depicts the configurations set for SV testing. The SV test is selected using the SV mode switch position and can be performed at any voltage range, including the V range

setting. If no custom SV test has been set up, a standard five-step test will be conducted with each step being 1/5th of the test voltage and 1/5th of the test time. For a standard five-step at the V voltage, the timer is set 1 to 0 seconds if a custom SV test has been previously adjusted.

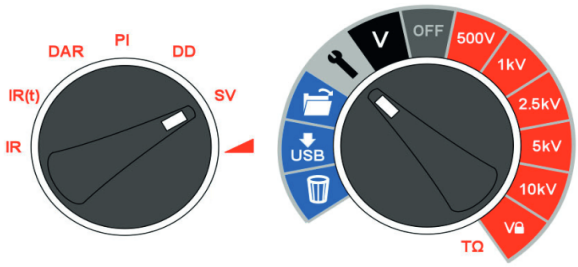

Figure 4.13: Step Voltage test mode

During the test, the applied voltage increments by one-fifth of the final test voltage each minute for a total of 5 minutes, with measurements taken at each step. Resistance readings for the first four steps are displayed under consecutive time designators '1m' to '4m'. The main display shows the 5-minute reading. If the user changes the default 5-minute test duration, the indicators for the four readings will not display the respective '1m' to '4m' markers.

The SV test duration can be adjusted from the default 5 minutes using the up and down arrow buttons and the setting is saved by pressing OK. The step timer will always be set to the total test time divided by five. It is noted that setting a step time that is too short may lead to incorrect readings, while a step time that is too long can over-stress the motor. The reference standard for step voltage testing is IEEE 95-2002.

4.3.5 Ramp Voltage test

The ramp voltage test is an overvoltage test that resembles the SV test but offers better control and early warning of potential insulation failure. Unlike the rapid step increases used in the SV test, the slow, continuous voltage ramp is less likely to cause unpredictable damage to the insulation. When using this test method, the test voltage is gradually increased at a predetermined rate to a final level, causing an increase in current. Any variations in current relative to the increase in applied test voltage can offer valuable diagnostic insights into the condition of the insulation.

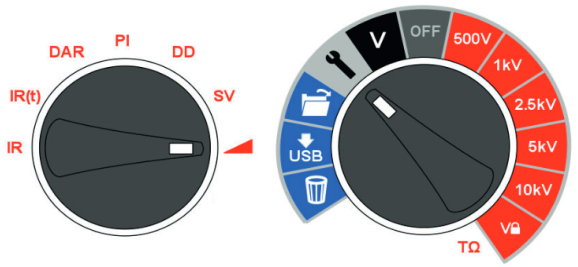

Figure 4.14: Ramp Voltage test mode

Before performing the overvoltage test, it must be ensured that the windings are completely discharged if a PI test was conducted to verify its suitability for overvoltage testing, a practice that is also performed in SV testing. The default voltage ramp rate ($\frac{dV}{dt}$) is 1kV/min, which can be adjusted in the settings function of the main rotary switch. As shown in Figure 4.14, the mode rotary switch must be rotated to the ramp mode position. The up and down arrow

buttons can adjust the $\frac{dV}{dt}$ rate to the desired level and then the setting is confirmed by pressing OK. The test will start by pressing and holding the TEST button.

During the test, the voltage will increment at a ramp rate until it reaches the selected test voltage unless a breakdown or sudden rise in current is detected. After the test, the final insulation resistance, voltage, and current are displayed. If the result is saved a complete curve of current in μA and voltage in kV is recorded. This data can be read into PowerDB, PowerDB Lite, or converted to a spreadsheet, allowing the current-voltage curves to be compared to published curves in IEEE 95-2002.

Figure 4.15: The Megger MIT1525 15kV instrument in the lab with clamps connected to the positive (red) and negative (black) terminals

4.4 Memory functions

The MIT1525 instrument can save the results of a resistance or voltage test by pressing the dedicated save button. The save button will momentarily appear to confirm that the data has been saved. If a full test curve is needed, the user must enable logging by pressing the save button before the start of the test. Data will be logged every five seconds throughout the duration of the resistance test. Voltages cannot be logged in voltmeter mode. The display backlight can be activated by pressing the corresponding button. Pressing the button again will turn off the backlight. If not manually deactivated, the backlight will automatically turn off after a preset timeout period.

The instrument includes an internal memory that has advanced storage capabilities. This allows the recall, download and delete of insulation test records by selecting the proper settings from the blue segments of the main rotary switch.

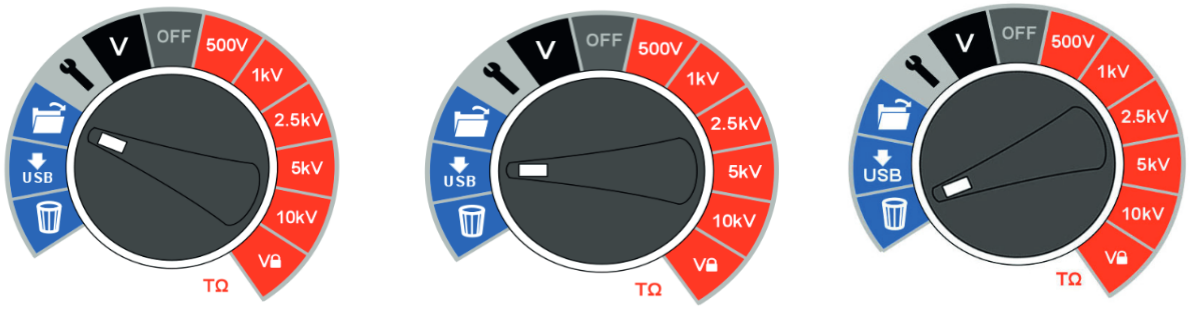

(a) Recall results (b) Download results (c) Delete results

Figure 4.16: Memory function modes

- **Recall results:** Selecting the 'open folder' position in the main rotary switch allows the user to recall saved results, starting with the most recent result. The up and down arrow buttons let the user scroll through results based on a sequential four-digit index, while the left and right arrow buttons scroll through a single result, displaying all saved test data including time and date. When logging is enabled, only the final result appears on the screen. The full result can be viewed by the PowerDB app, which is described in 4.5. In saved results, the test mode is indicated by an icon or abbreviation of each test on the screen. Furthermore, the open folder icon shows that recall memory mode is active.

- **Download results:** The default downloading of the instrument is a single test log or summary result. Downloading of all results is possible by pressing an arrow button. The download procedure involves the PowerDB app, in which the results are downloaded using a cable connected to a PC where the data are stored afterward.

- **Delete results:** There are two options to delete records. These options involve the deletion of a single result or the deletion of all results. The bin icon must be selected on the main rotary switch to enable deletion. The first record shown is the most recent test result. Users can navigate through results by the up and down arrow buttons and when the desired result is found, it is selected for deletion with the OK button. An 'X' icon will change to a tick and the on-screen bin icon will flash. Pressing again OK will confirm this deletion. The default action is to delete a single test result, however this can change by pressing the right arrow button. This action will enable the deletion of all test results from memory.

4.5 PowerDB

PowerDB is a free software application that can be used for real-time data output records. Resistance, voltage and current data are sent at a rate of 1 Hz from the instrument and are shown in real time on figures and graphs. The most common graphs involve plots of current (μA) and voltage (kV) on the x-y axes, such as those produced on SV or ramp tests. Before running a test that requires real-time output, a computer with PowerDB downloaded must be attached via a USB cable. The serial port allocation on Device Manager must be checked, so the correct serial port number is assigned when starting PowerDB. PowerDB provides specific instructions about real-time data capture.

PowerDB is a software tool for collecting and reporting data, which provides a simple and consistent user interface to many Megger instruments, such as insulation power factor, relays, transformers, circuit breakers, power transformer ratio, winding and insulation resistance, battery impedance and discharge test sets, including the MIT1525 15kV IR tester. It can be directly downloaded from the official Megger website. The latest version will be at the top and can be installed by clicking the "Download" button and following the onscreen instructions. After the installation is completed, a shortcut of the application will be created on the desktop of the user's computer.

If there is a need for the results of a test to be stored locally in the storage system of a PC/laptop, the PowerDB acts as the interface for that purpose. On the right side of the MIT unit, there is a USB cable connection port. The procedure is direct and simple. First, the instrument must be connected to the PC/laptop via the USB cable, which is provided with the instrument (shown in Fig. 4.7), and the driver for the instrument must be enabled to be found online. The instrument is powered up through the USB cable to respond to the driver. The PowerDB software should be launched by clicking its icon on the desktop. As shown in Figure 4.17, the "Instrument Selection" window opens as the main portal, from which the appropriate instrument tester must be chosen. The instruments are organized by the type of equipment being tested. The user will be redirected to the Instrument Configuration Window (Fig. 4.19a). In Device Manager, the 'Ports' section contains the serial ports of the user's computer and one port should be assigned to 'Megger Device (COMxx)', where xx represents the port number. If the port number xx is correctly assigned, it will be shown in which port of the computer is connected in the 'Serial Port' tab of the Instrument Configuration window. Other information regarding the instrument model, test mode, manufacturer, and baud rate is also included and must be correctly selected. The setting will be completed after clicking OK. Finally, the Form window pops up, shown in Figure 4.19b. Users must select the appropriate test mode for the required equipment in this window and click OK to proceed with the test run.

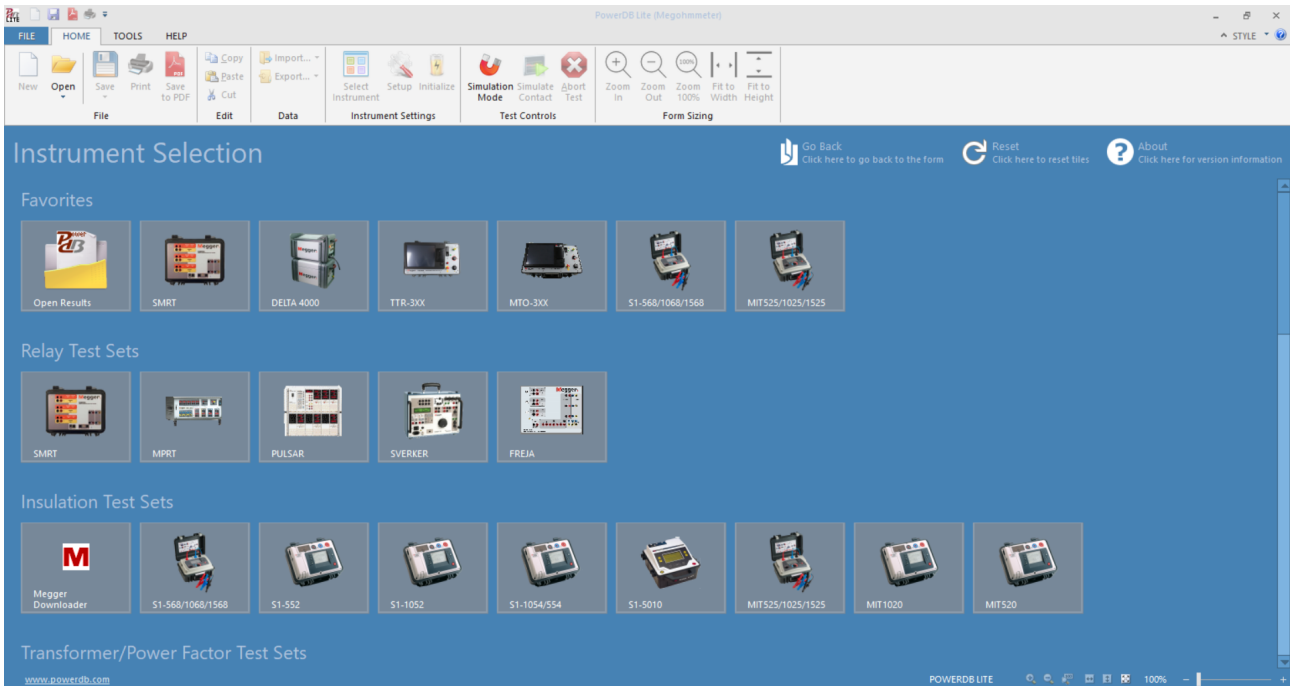

Figure 4.17: PowerDB Lite app environment

When the form loads, there is an option in the toolbar at the top to initialize the instrument. If the communication is successful, an 'OK' will appear at the top of the form. There is also an option to set the instrument by clicking the 'Setup' icon next to the 'Initialize' icon. The

simulation mode to run a test is enabled by clicking the 'Simulation mode' icon and by clicking it again it is deactivated.

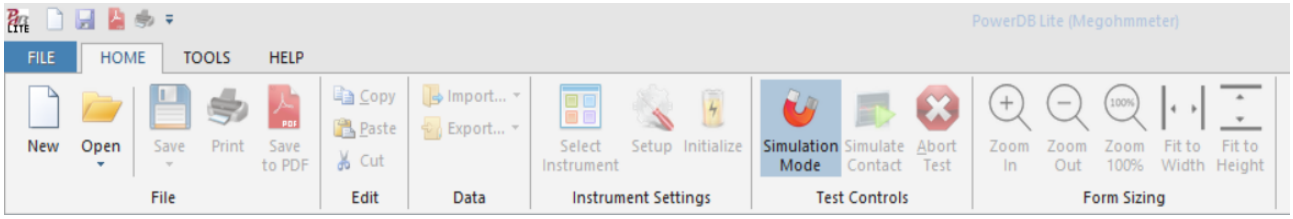

Figure 4.18: PowerDB toolbar

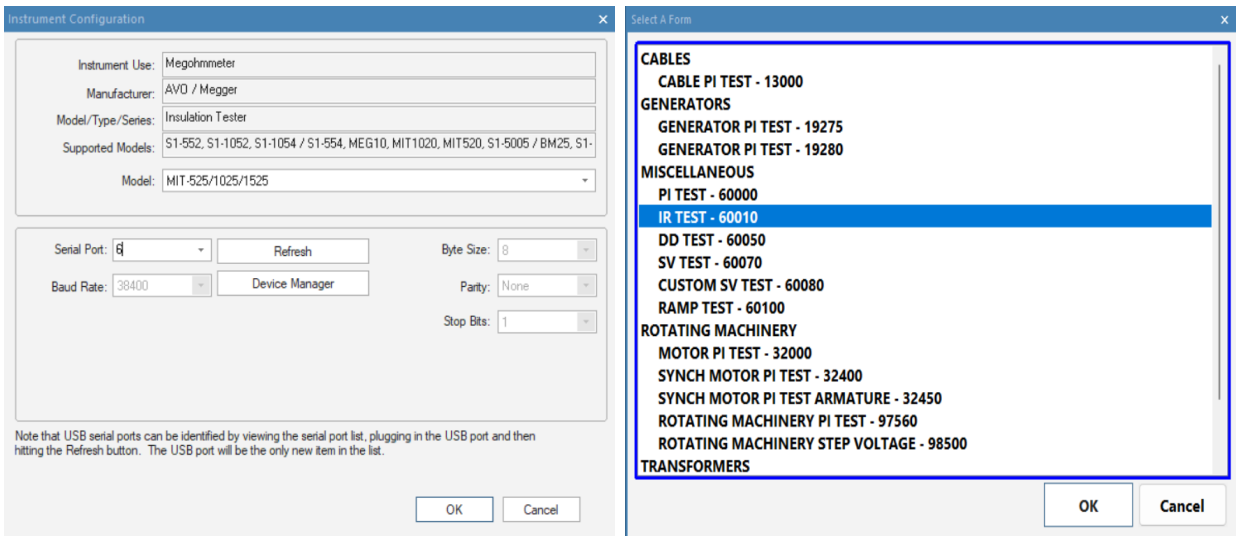

(a) The Instrument Configuration Window (b) Form window for test mode

Figure 4.19

A new window will appear with the test mode selected for the required equipment. It provides information regarding the date, humidity and temperature of the equipment, and graphs that it will produce. At the bottom of the window, a table like the one in Figure 4.20 enables the MIT control application. The table contains headers for voltage (kV), current (μA) and readings with their corresponding test time execution. The IR test has been selected in the photo, so the readings contain resistance values in megaohms. The cells represent three phases A, B and C. Right-clicking on one of the readings of the three phases activates the MIT control application and clicking on a phase opens up the appropriate application.

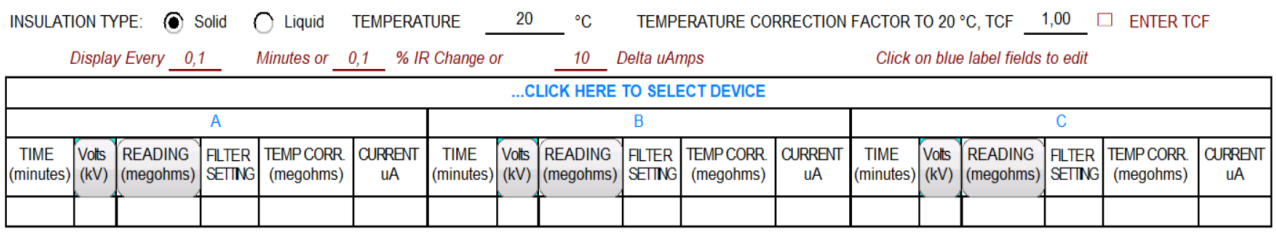

Figure 4.20: The PowerDB table that activates measurements

Next, the Import/ Live Stream Control Application window will launch. This window allows for multiple functions by clicking each button of the image in 4.21.

- The Start New Live Stream function activates the capture of live streaming data. Test results are recorded every second for the total duration of the test. Different graphs can be recorded if different quantities are selected, including time in minutes or seconds, current, voltage and resistance
- The Start Importing Results function allows the downloading of results stored on the instrument
- The Save Selected To Form function saves a selected test result from the top-right-hand menu to the current form in PowerDB Lite. Tests listed under Test Info in the Import/Live Stream Control application can be saved to any form by exiting the logger (Go Back To Form option), then clicking the desired phase in the form and selecting Save Selected To Form.
- The Copy Results to Clipboard function copies all data as Excel cell values, which facilitates to be pasted in a CSV or XLSX file.
- The Export Selected function facilitates the export of data of a test from the top-right-hand menu as a file, so these can be then imported to another software or application, while the Export All button exports all tests from the menu.
- The Delete functions are separated into three different buttons. The Delete Selected Data button removes test data from the Test Info section. The Delete Selected button removes a test from the top-right-hand menu and the Delete All button deletes all tests from the menu.

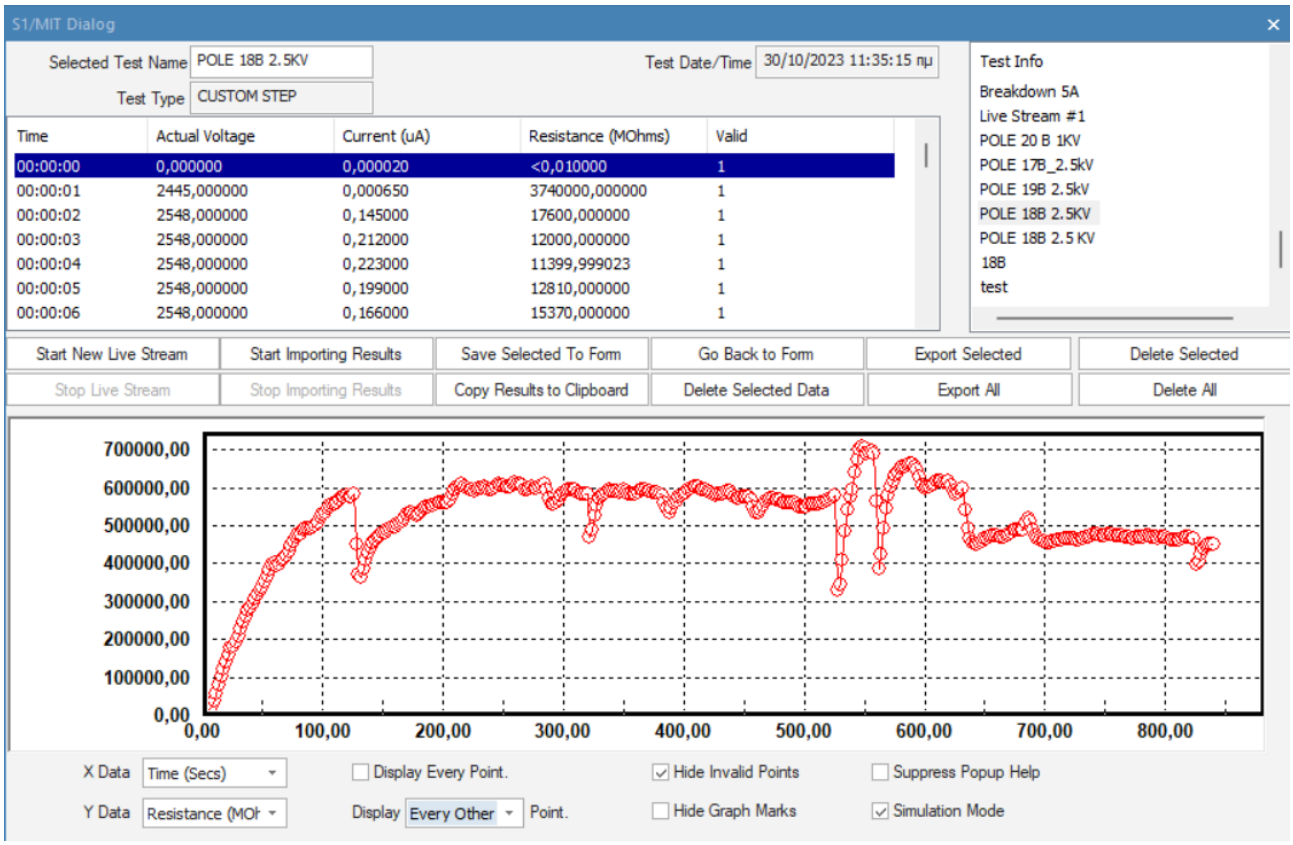

Figure 4.21: A sample of Live Stream Control Application window after a test

PowerDB enables real-time trending of any data values within the test results. This trending feature allows for easy comparison of new readings with historical values, as well as with similar

equipment in the database of the user. It appears as a very useful tool for statistical information based on the selected and retrieved data to help assess the test results and determine the condition of the equipment.

4.6 Battery and Errors indicators

The MIT unit is equipped with 2 Li-ion batteries of 10.8V, 5.2Ah. The battery symbol on the LDC screen consists of four pairs of segments. While the device is turned on, the battery is continuously monitored. The following pairs of segments indicate the remaining battery charge:

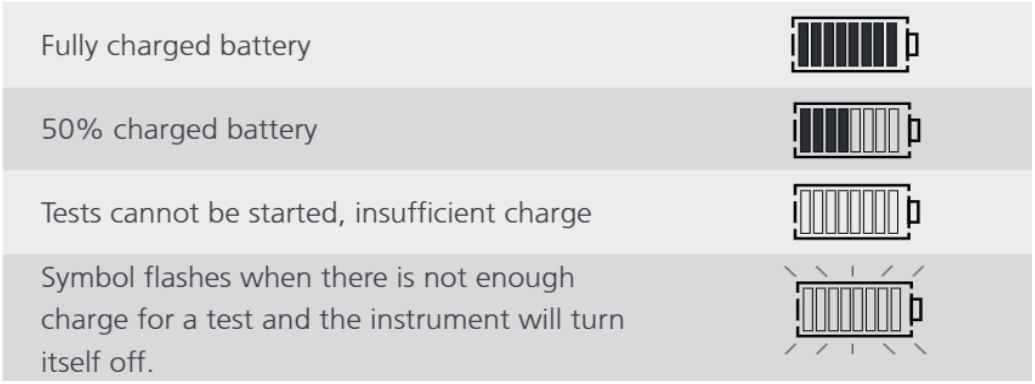

Figure 4.22: Battery symbols

When mains power is available, the indicator displays the state of charge by animating the bar graph segments. If the full battery icon blinks, it means that charging is prevented either because the temperature is outside the allowed range of 0°C to 40°C or the battery has failed. The total battery charge time lasts about 2.5 hours and the total battery life lasts for 4.5 hours of continuous testing at 15kV with a 100MΩ load.

During the operation of the instrument, various errors can occur. These errors are reported with different error codes and preceded by 'Err' on the display screen. The following table provides the list of the error codes accompanied by the faults they indicate.

'Err' code	Fault
2	Output voltage over limit
3	FIFO (memory) overflow
4	HV board mismatch with control board setup
5	Battery low error
6	Control board detected inter-board communication failure
7	Test button stuck
8	Measurement board i2c failed
9	Measurement board detected inter-board communication failure
10	Isolation power supply cut-out
11	Instrument attempted auto power off but failed
12	HV circuit control fault

Table 4.5: Faults indicated by their error codes

5 Experimental procedure

This thesis analysis is part of a large research project, the TEAMstress project, which focuses on comprehending the deterioration processes of the pole insulation of permanent magnet synchronous axial flux motors having the yokeless and segmented armature topology (see the 1.4.6 section). Unfortunately, it is not possible to provide any photos of these poles due to a customer's product agreement. The coil armature of stator poles handles high currents to maintain a high torque density, which is critical for pole insulation. The research involved the development of the pole model, the design and development of test benches to conduct quality test procedures, the analysis of the results and the extraction of valuable conclusions. There will be a summary of the stages followed chronologically during the realization of the project, presenting the model development and the tests conducted, but with a primary focus on the fixed thermal stress procedures. Specifically, there is a reference to the thermomechanical effects caused by thermal cycling testing and are compared to the stresses from the typical fixed thermal stress testing. Test samples included stator copper bars and stator poles with mounted windings, some impregnated with epoxy resin and some not. Additionally, the results of multi-stress aging, which includes mechanical oscillations, are presented. The ultimate goal is to evaluate the effectiveness of impedance spectroscopy as a reliable and sensitive tool for assessing insulation health.

5.1 Pole Model Development

Although literature includes numerous models that attempt to describe the coil behavior at different frequencies [135],[136],[137],[138], less work has been done on experimentally modeling the actual components with high levels of complexity to enable accurate predictions and account for most real-world phenomena and manufacturing characteristics. Older models exhibited lower complexity levels and were developed for design or control only at specific operating frequencies [139],[140]. An experimentally derived more complex model of stator poles with mounted windings had to be developed and utilized to support the analysis of data collected from the accelerated aging methods. A view of the stator pole is provided in 5.1a and its equivalent circuit in 5.1b with its parameters defined in 5.1.

The stator pole comprises the iron core, encased by a Nomex layer and the coil on the outside, while the entire assembly is impregnated with epoxy resin. For the conduction of the experimental procedures, 95 pieces of this segmented stator pole assembly were used, while some poles that did not undergo impregnation were also used to observe the impact of epoxy resin on the spectroscopy of the poles after accelerated aging. Equivalent circuit parameters are extracted from both the pole and the mounted coil, along with additional factors derived from the equipment used in measurements. This model ensures that poles meet the expected standards during the manufacturing process, as it ensures that quality inspection, fault prognosis and diagnosis purposes are served. Any parameter variations during aging processes can cause unique changes in the impedance spectroscopy or Nyquist plots. Therefore, the model can identify which parameter is leading to that change and subsequently, it can identify the corresponding defect or issue.

A certain degree of asymmetry has been inserted in the turns modeling. All the coil turns, except for the first and last turns, share the same characteristics considering R_a, L_a, C_i, R_i. The first and last turns are affected by capacitance fringing and coil end effects [141],[142], thus they exhibit different properties. Additionally, the surface areas of the first and last turns are smaller than those of the inner coil turns. L_{series} represents a parasitic inductance caused by the impedance spectroscopy instrument, increased by the inductance of one turn. This additional turn is actually the combined inductance of the two halves of the first and last turns, which

are not linked by a capacitance to the second and the second from the end turns. Further explanation of the other parameters follows in the text later on.

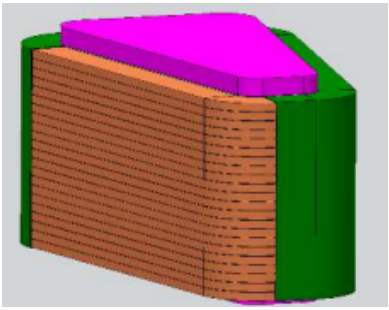

(a) The stator pole with the mounted armature coil

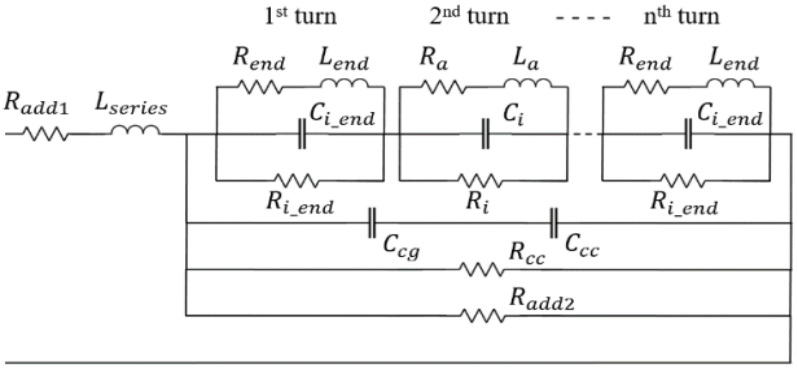

(b) Equivalent circuit of the examined poles

Figure 5.1: The stator pole design and its equivalent circuit

R_{add1}	Additional resistance due to the circuit winding
L_{series}	In-series inductance due to the instrument augmented by 1 turn's inductance
R_{end}	Internal turn resistance of the first and last turns of the coil
L_{end}	Inductance of the first and last turns of the coil
C_{iend}	Capacitance between the 1st and 2nd turn of the coil
R_{iend}	Insulation resistance between the 1st and 2nd turn of the coil
R_a	Internal turn resistance
L_a	Single turn inductance
C_i	Capacitance between two turns of the coil
R_i	Insulation resistance between two turns of the coil
C_{cg}	Added capacitance aiming to measurement correction
C_{cc}	Capacitance between the core and coil
R_{cc}	Insulation resistance between the core and the coil
R_{add2}	Shunt resistance of the impedance spectroscopy

Table 5.1: Equivalent Circuit Parameters Index

5.1.1 Turn parameters

- **Internal turn resistance** R_a

The internal resistance of the coil was measured using an ohmmeter. However, the skin effect [143] must be considered since the spectroscopy reaches high frequencies up to 20 MHz. Consequently, the resistance has been calculated for each frequency step, as shown in Figure 5.2. The plot consists of the DC part which remains almost stable and the AC part where the resistance increments linearly.

$$R_{HF} = \frac{l}{2 \cdot \sigma \cdot (w + t) \cdot \delta} \tag{5.1}$$

where l is the length, σ denotes the conductivity, ρ stands for resistivity, w signifies the thickness, t defines thickness, δ represents the skin effect depth and f_{se} is the critical frequency in which the skin effect acts, where:

$$\delta = \frac{1}{\sqrt{\pi f \mu \sigma}} \quad and \quad f_{se} = \frac{4}{\pi \mu \sigma}\left(\frac{w \cdot t}{w + t}\right)^2 \tag{5.2}$$

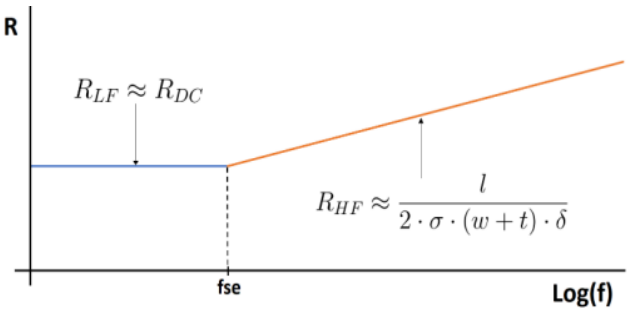

Figure 5.2: Skin effect impact on the coil internal resistance

- **Coil Inductance L_a**

The coil inductance was measured using an impedance spectroscopy analyzer for the total of 95 poles. This population allows for reliable statistical analysis. As the frequency increases, the coil inductance starts to dominate and the phase moves towards 90°. The maximum angle is identified, which is approximately 90°, and the impedance at this frequency is extracted, which signifies the total coil impedance. This value is then divided by the total number of turns and is incorporated into the model. The measured inductances are listed in table 5.2 and their corresponding statistical data are shown in Figure 5.3. The vast majority of the poles do not exhibit significant variations, with the average inductance being 37.9 μH.

Limits (μH)	**Number of Points**
37.2 - 37.48	3
37.48 - 37.76	3
37.76 - 38.04	30
38.04 - 38.32	31
38.32 - 38.6	18
38.6 - 38.88	4
38.88 - 39.16	1
39.16 - 39.44	3
39.44 - 39.72	1
39.72 - 40	1

Table 5.2: Coil Inductance Ranges and Distributions

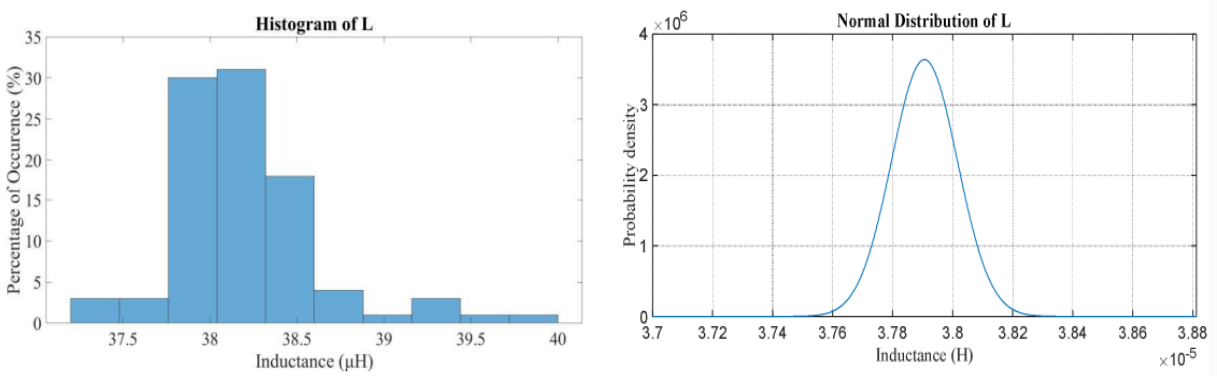

Figure 5.3: Histogram and distribution of measured poles' inductance

- **Turn-to-turn Insulation Capacitance C_i**

For measuring the insulation capacitance between the coil turns, a set of 10 copper bars with thin-film insulation, each coated with PAI insulation and made from the same coil wire, was used (Figure 5.4). The measurement procedure is straightforward. Each time a pair of bars is inserted into two ducts within a specially made case, as shown in Figure 5.5. The bars are positioned perpendicular to each other, forming a square contact area due to their identical widths. This arrangement allows the first bar to move up and down and the second bar to move left and right, creating multiple contact areas between them. The ends of the bars have been stripped of their PAI insulation and function as the electrical contact points for impedance spectroscopy electrodes.

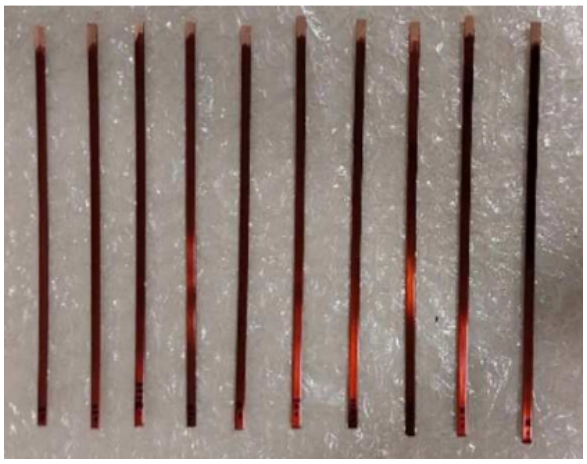

Figure 5.4: The copper wire specimens

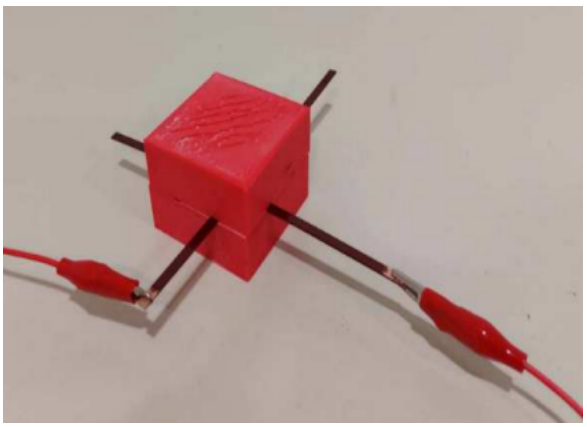

Figure 5.5: The insulation capacitance measurement between turns setup

A total of 80 measurements were conducted to enable a robust statistical analysis. The impedance spectroscopy results with their corresponding phase are depicted in Figure 5.6. From these measurements, the minimum angle and the frequency in which occurs were tracked. A frequency of 80kHz was uniformly chosen, in which the angle for all samples is greater than -89.8°(≈-90°). In this frequency, the circuit behaves like an ideal capacitor. The impedance value is then extracted at these points and using the following equation the corresponding capacitance value is calculated:

$$X_C = \frac{1}{\omega C} \Longrightarrow C = \frac{1}{2\pi f X_C}, \quad where \;\; \omega = 2\pi f \tag{5.3}$$

After solving the equation for all sample setpoints, the corresponding capacitance values were calculated and organized into groups, as shown in Table 5.3. The corresponding histogram is depicted in Fig. 5.7a and the calculated normal distribution in Fig. 5.7b. Although the average capacitance value is 5.1723 pF, the minimum capacitance value is 4.1262 pF while the maximum value is 6.1355 pF. These values are 20.2% lower and 18.6% higher than the average respectively.

The mean capacitance value was utilized in this work. It was first adjusted to the correct surface area before being incorporated into the model. Initially, the measured value was normalized according to the surface area. Next, the mean length of one turn and the actual surface area of the turn were calculated. Finally, the normalized capacitance was multiplied by the turn's surface area and this value was integrated into the model, denoted as C_i.

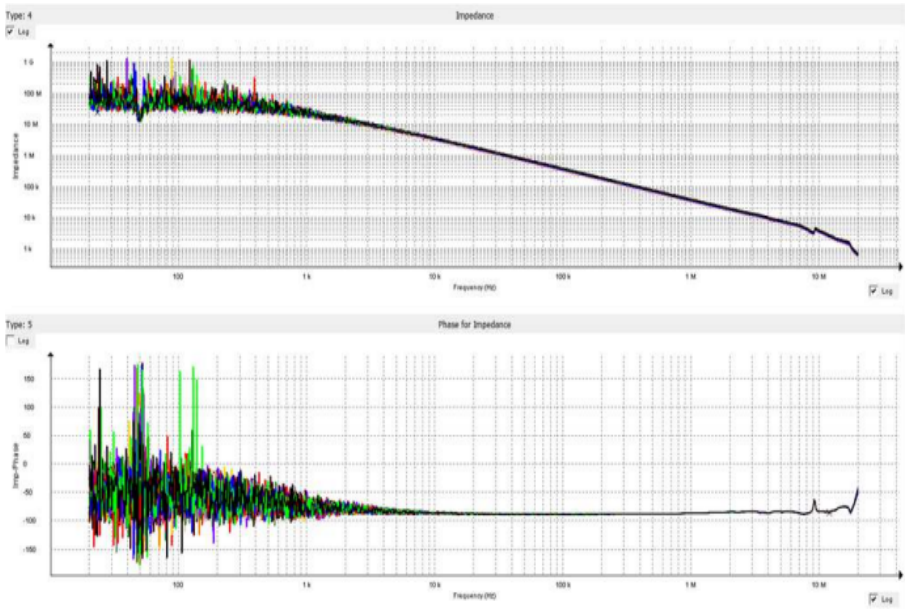

Figure 5.6: Impedance spectroscopy of the contact area between couples of bars

Limits (pF)	Number of Points
4.1 - 4.29	2
4.29 - 4.48	4
4.48 - 4.67	8
4.67 - 4.86	9
4.86 - 5.05	11
5.05 - 5.24	11
5.24 - 5.43	9
5.43 - 5.62	7
5.62 - 5.81	6
5.81 - 6.0	9
6.0 - 6.19	4

Table 5.3: Capacitance Values of the 80 Area Samples

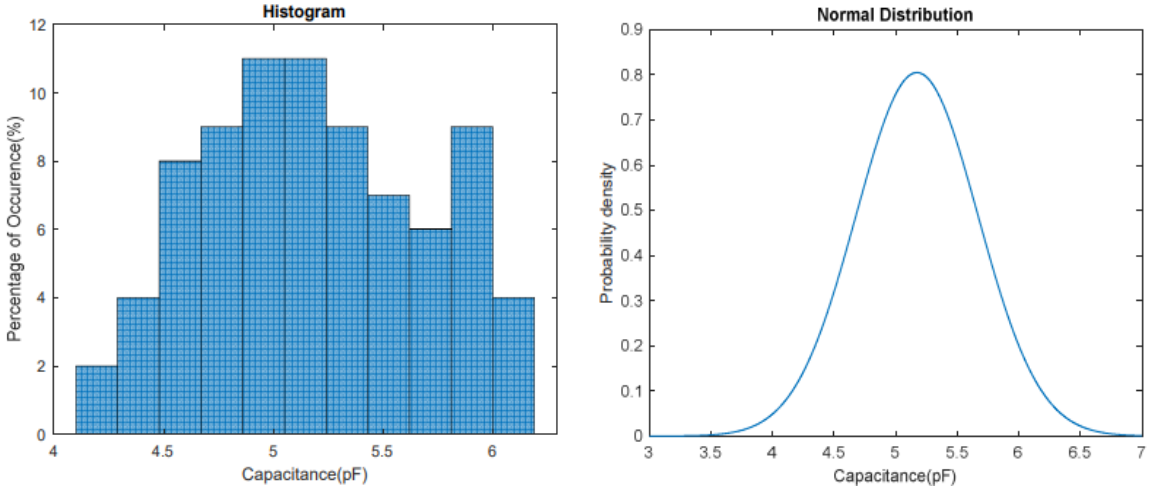

(a) (b)

Figure 5.7: Histogram and distribution of measured areas capacitance

- **Turn-to-turn Insulation Resistance R_i**

For the insulation resistance measurement between turns, the available 10 copper bars were utilized, divided into 5 pairs for simultaneous testing. Each pair was placed inside the shielding case in two parallel ducts, with a thin copper plate crossing over both of them. The ends of the copper bars are shorted on one side and left open on the other side, leading to a parallel connection of the bars with the shorted ends and the copper plate. The 15kV Meggohmmeter was used, described in section Megger user manual, with its two electrodes connected to the shorted ends of the two bars and the copper plate. The complete setup is depicted and described in Fig. 5.8. This connection was made since otherwise the insulation resistance has too high value and the instrument cannot record it directly. By measuring the resistance of two insulation areas in parallel, their combined resistance R_t is recorded by the Megohmmeter. To find the resistance of each bar, it was assumed that the bars were identical, meaning that they were made from the same material and had the same dimensions, as well as the resistances are equal. Therefore, by using the equation for parallel resistance, the resistance R_i for each bar is calculated:

$$R_t = \frac{R_{i,1} \cdot R_{i,2}}{R_{i,1} + R_{i,2}} = \frac{R_i \cdot R_i}{R_i + R_i} = \frac{R_i^2}{2R_i} = \frac{R_i}{2} \tag{5.4}$$

The IR test mode was set to the 15kV Megohmmeter to subject each sample to 5kV for 8 minutes until the measurement was stabilized, as shown in Figure 5.9. By repositioning the copper plate, measurements were taken at three different locations on the bars. This approach generated a statistically significant dataset, from which the mean value was extracted.

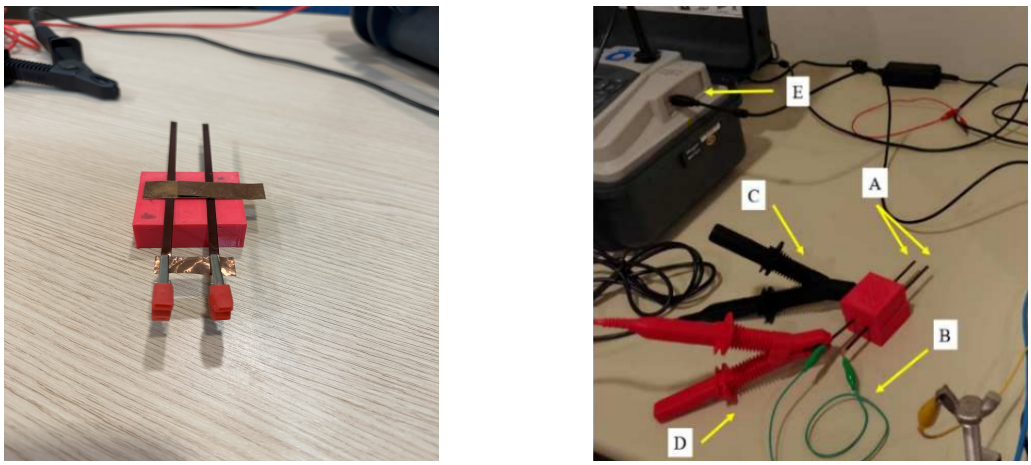

Figure 5.8: Measurement setup for insulation resistance: A)the two copper bars, B)the short circuit at one end of the bars, C)electrode connected to the copper plate placed on top of the bars, D)electrode connected to the shorted end of the bars, E)the Megohmmeter producing high voltage

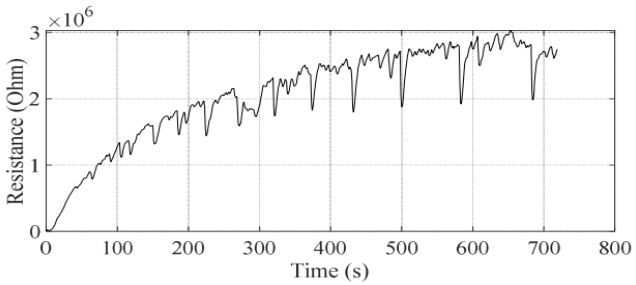

Figure 5.9: Typical insulation resistance measurement for 8 minutes at 5kV

- **Coil-to-pole properties**

The parameters between the coils and core of the poles, inserted in the model, are the insulation resistance and the capacitance denoted as R_{cc} and C_{cc} respectively. First, to measure the insulation resistance between the coils and core (or the groundwall resistance), the poles had to be placed above the copper plate on top of the custom-made case. The connection with the Megohmmeter is achieved, with one terminal being connected with the contact point between the copper plate and the pole and the other with the stripped end of the mounted coil of the pole. The IR test mode was selected on the instrument and the measurement time was set to 14 minutes. This time was sufficient for the capacitive and charge currents to become zero and the resistance to be stabilized, dependent solely on the leakage current. The mean resistance value was found $R_{cc} = 2.78\ T\Omega$ through the statistical analysis of the results of the 95 poles and was inserted in the model.

For measuring the insulation capacitance between the core and the coils (or the groundwall capacitance) a 3D-printed box was crafted with a conducting layer on the bottom to provide galvanic connection, depicted in Figure 5.11. The pole was placed inside that box, with the conducting layer being in absolute contact with the pole's core surface. An impedance analyzer was used, with one electrode of the analyzer connected to the stripped end of the mounted coil and the other to the electrode extended from the end of the bottom layer. The impedance and phase plots were examined similarly to the C_i measurement and the capacitance was computed ensuring that the phase angle was at its minimum and close to $-90°$.

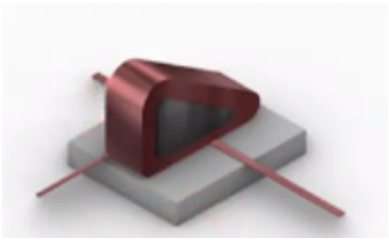

Figure 5.10: Setup for core-to-coil IR measurement

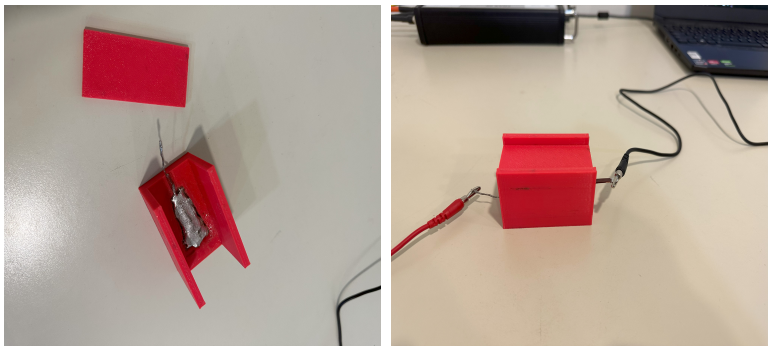

Figure 5.11: The custom-made 3D printed box with conducting bottom for groundwall capacitance measurements

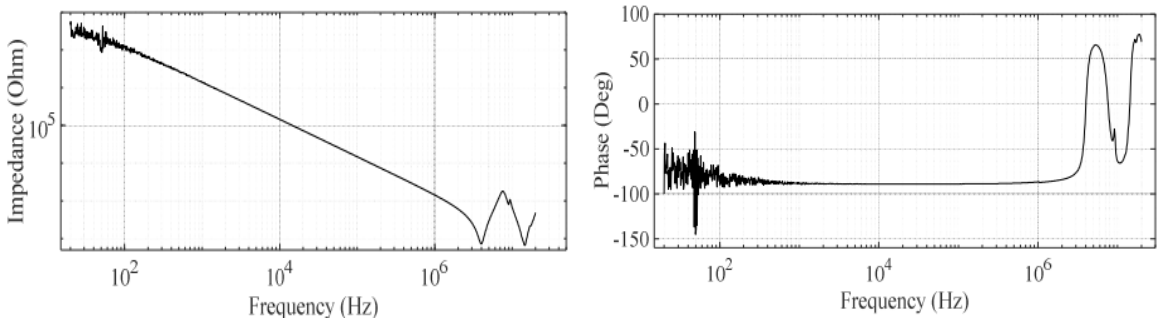

(a) (b)

Figure 5.12: Impedance spectroscopy of the insulation capacitance between the coil and the core where: a) the impedance and b) the phase

- **End-turn parameters**

As already mentioned, the first and last turns of the coils exhibit different properties from the intermediate turns due to fringing effects and coil end effects. In particular:

1. L_{iend}: The first and last turns of the coil do not complete a full turn and the inductance is proportional to the square of the number of the turns, thereby a factor k_L is used, equal to 0.8. Thus, $L_{iend} = k_L \cdot L_a$.

2. C_{iend}: The capacitance of the first and last turns has to be increased by a fringing factor k_f. Since the copper bars are very close to each other, electric field lines form from the sides of the bars and the external surface areas of the first and last turns. The factor k_f was calculated using the following formula [144]:

$$C = \frac{\varepsilon_0 \varepsilon_r w l}{g} + \frac{\pi \varepsilon_0 \varepsilon_r (w + l)}{ln(\frac{\pi}{2}(1 + \frac{g}{t}) + \sqrt{\frac{\pi^2}{4}(1 + \frac{g}{t})^2 - 1})} \tag{5.5}$$

   where l and w denote the length and width of the capacitor plates respectively, g signifies the distance between the plates and t describes the thickness of the plates.
   Finally, k_f was found equal to 1.1, thus $C_{iend} = k_f \cdot C_i$.

3. R_{iend}: The first and last coil turns do not complete a full turn, leading to a difference in resistance from the intermediate turns by a factor k_R. Thus, $R_{iend} = k_R \cdot R_a$.

- **Additional parameters**

Additional parameters had to be calculated and integrated into the model due to interference of the measuring equipment. First, R_{add1} is the additional DC resistance in series with the entire circuit due to electrodes used for pole wiring with the impedance analyzer, which was found equal to 1.37Ω. L_{series} is the inductance in series with the entire circuit due to the instrument augmented by 1 turn's inductance, equal to $2.09\mu H$. R_{add2} is the shunt resistance of the impedance analyzer, which has a total of 50Ω resistors, and finally, C_{cg} is the added capacitance, which was estimated for measurement correction so that the impedance spectra of the equivalent circuit model and the experimentally measured pole match each other.

5.1.2 Frequency response analysis

Once the equivalent circuit model was complete with all its parameters taken into account and estimated, the impedance spectroscopy method was employed to record the impedance and phase diagrams of the poles. The FRAX-99 Sweep Frequency Response Analyzer was the measuring instrument for that purpose, depicted in Fig. 5.13a.

For that purpose, a dedicated table was used to install the relevant equipment. As shown in Fig. 5.13b, the two electrodes were mounted on the table at fixed positions, spaced in such a way as to eliminate any parasitic phenomena. These electrodes were properly connected to the analyzer, particularly to the generator, reference, and measure plugs to enable the production of the sinusoidal voltage over the entire range of frequencies and the readings to be recorded. Two smaller wires were connected to the electrodes with crocodile clips at their ends, to which the pole under test was connected, between the two electrodes. Finally, a laptop was connected to the instrument to control the measurement process and store the results.

The impedance spectroscopy of the poles was measured by connecting the crocodile clips of the small wires attached to the electrodes of the analyzer to the stripped ends of the coils. The diagrams of impedance and phase angle were produced by recording the readings for

each frequency component in the range of 20Hz to 20 MHz. The impedance spectroscopy of an experimentally measured pole in comparison to the spectroscopy of the equivalent circuit model is depicted in Fig. 5.14. Similarly, for the turn-to-turn capacitance measurements, the stripped ends of the bars were connected to the crocodile clips of the small wires between the electrodes, to produce the diagrams for C_i with the FRAX instrument. For the groundwall capacitance diagrams, the FRAX analyzer produced its impedance and phase plots for the whole range of 20Hz to 20MHz by connecting one crocodile clip to the stripped end of the coil under test and the other clip to the electrode extended from the conducting bottom layer, while the pole is inside the 3D printed box between the electrodes.

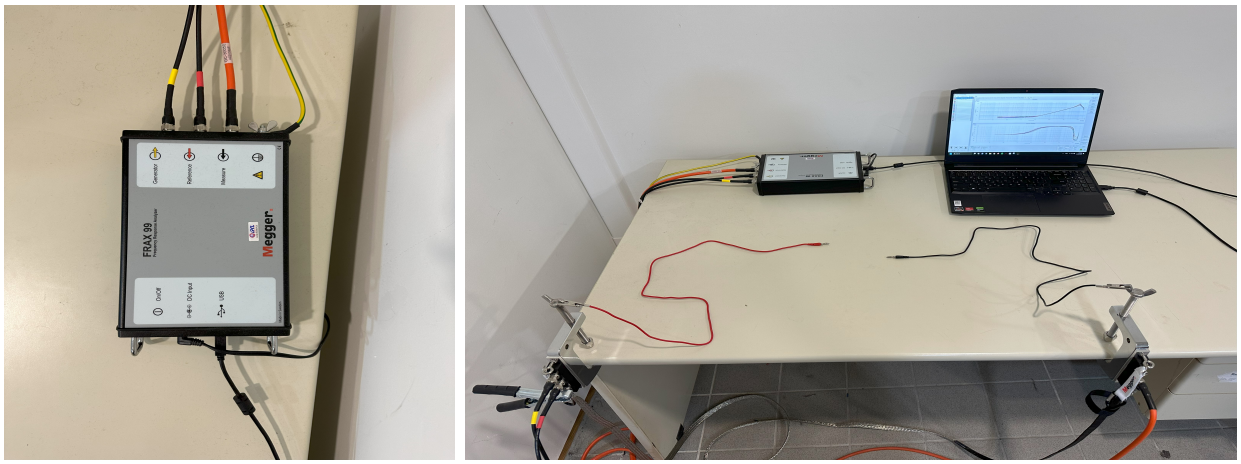

(a) The FRAX-99 analyzer (b) The experimental setup for impedance spectroscopy

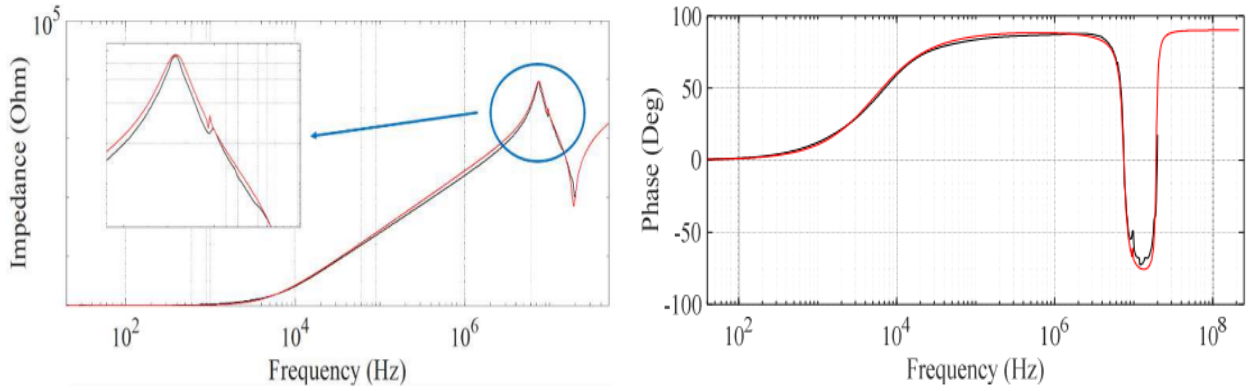

(a) (b)

Figure 5.14: Impedance spectroscopy of the complete equivalent circuit model (red) and the experimentally measured pole (black) where: a) the impedance and b) the phase

It is noted that two types of poles were used in this research. Although they have similar geometrical features, the poles from the first group are impregnated and will be referred to as Group A. Conversely, Group B comprises non-impregnated poles. Both groups consist of 95 poles in total, all of them have undergone impedance spectroscopy, which will be used as a reference, referred to as healthy poles, for comparison with the aging test results.

Furthermore, all poles underwent a High-Voltage IR test before thermal stress to determine the insulation resistance between the coil and core during the modeling stages. This test affected the coil's impedance, which is why the results have been included in the analysis alongside the conditions of both healthy and aged poles. Specifically, the majority of the poles experienced a drop in impedance amplitude without shifting on the frequency axis, which was attributed to a decrease of the coil-to-core insulation resistance.

5.2 Thermal cycling test

Poles were subjected to a thermal cycling test, which simulates the temperature fluctuations in insulating materials during motor operation under varying loads, but with minimal variations. More specifically, 18 impregnated poles of Group A and 18 non-impregnated poles of Group B have undergone this stress. The stress testing of Group A poles was carried out first and was thus more exploratory. The stressing temperature along with the duration for each cycle are detailed in Tables 5.4 and 5.5.

Cycle	**Temperature Range**	**Duration**
C1	180-220°C	6 hours
C2	180-220°C	6 hours
C3	180-220°C	6 hours
C4	180-220°C	6 hours
C5	180-220°C	6 hours
C6	180-220°C	6 hours
C7	210-250°C	3 hours
C8	210-250°C	3 hours

Table 5.4: Group A Thermal Cycling Strategy

Cycle	**Temperature Range**	**Duration**
C1	180-220°C	6 hours
C2	190-230°C	6 hours
C3	200-240°C	6 hours
C4	210-250°C	6 hours

Table 5.5: Group B Thermal Cycling Strategy

An oven was used to passively apply the thermal cycling stress on the poles and achieve the desired temperatures. One digital and one analog thermometer were placed inside the oven to monitor the temperature throughout the process. Since the insulation class of the poles is rated for 220°C, the initial aim of the experiment was to stress the poles up to this insulation limit (220°C). However, minimal changes were observed, thus the temperature limits were increased to 250°C for the last cycles, but the duration was halved. Each thermal cycle maintained a constant temperature range of 40°C, with a cycle period of approximately 8 minutes, covering the time needed for the temperature to rise from the lower limit to the upper and back. At the end of each cycle, the insulation condition of the poles was assessed using impedance spectroscopy, producing the corresponding impedance and Nyquist plots.

The impedance spectroscopy results of Group A poles with their corresponding phase diagram are depicted in Figure 5.15 and 5.17. The average behavior of all the samples has been taken for each cycle. Impedance depends on the DC resistance of the electrodes and wiring with the analyzer at low frequencies. At the same time, spectrum changes can occur at high frequencies due to the skin effect and aging mechanisms. Since impedance remains unaffected in frequencies $\leq 10^4$ Hz, the focus lies on frequency components around 10^7 Hz, where the primary and second spikes exist. Hence, the impedance diagrams have been zoomed in to provide a better insight into the effects of each thermal cycle on the primary and second spike of the impedance in Figure 5.16. In addition, the Nyquist plot of Figure 5.18 complements the results of impedance spectroscopy.

The High-Voltage IR test leads to a reduction in impedance amplitude. Consequently, the Nyquist ellipsis exhibited a smaller radius. Moreover, the secondary impedance peak increased and shifted to the left compared to the healthy poles.

Upon the completion of the first thermal cycle, results significantly changed. The ellipsis size expanded at its maximum, impedance increased and the secondary spike shifted to the right of the healthy one with a higher amplitude. This outcome is attributed to chemical changes in the entire insulation system. Hence, it is reasonable to infer that the primary change is due to a reduction in the thin film capacitance, leading to higher impedance.

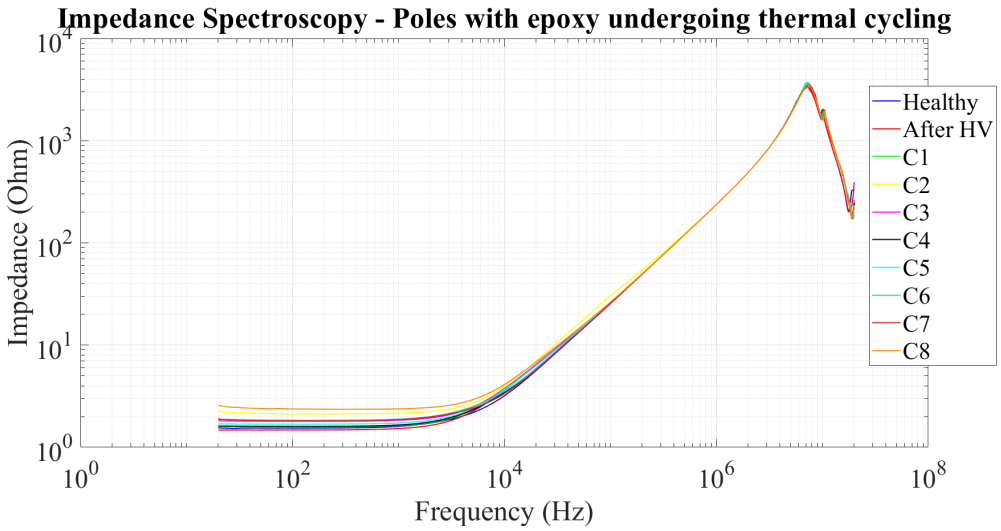

Figure 5.15: Impedance spectroscopy of the Group A poles subjected to thermal cycling stress conditions

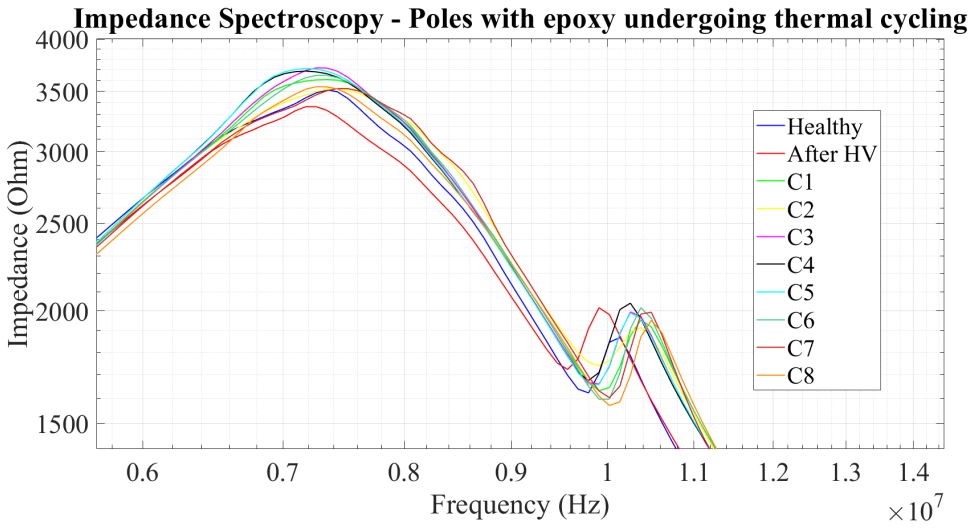

Figure 5.16: Zoomed impedance spectroscopy to emphasize the impact on the primary and 2nd spike

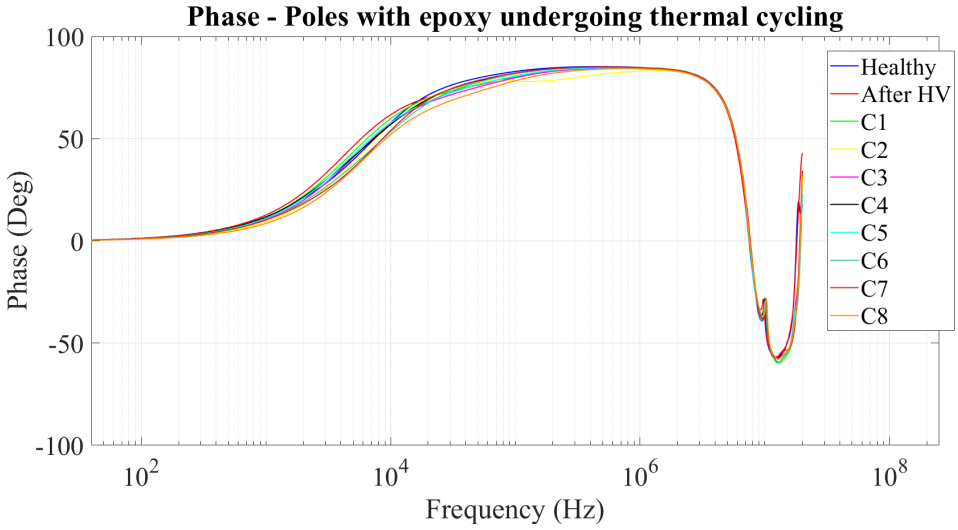

Figure 5.17: Phase of the Group A poles subjected to thermal cycling stress conditions

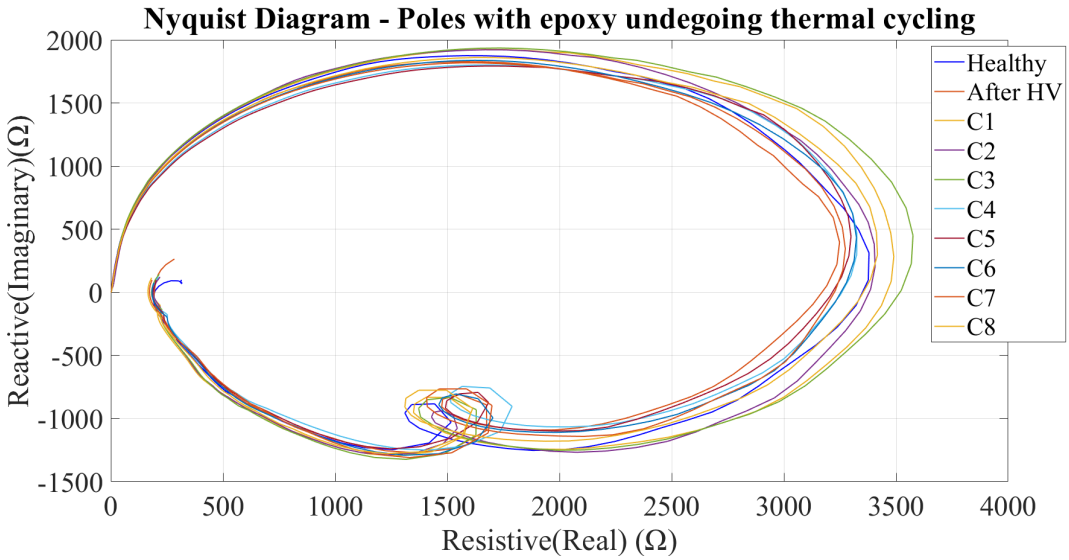

Figure 5.18: Nyquist diagram of the Group A poles subjected to thermal cycling stress

Interestingly, the behavior of the impedance spectra and the Nyquist plots did not follow a monotonic pattern during the accelerated thermal aging process. The amplitude fluctuated after each cycle, but the Nyquist ellipsis gradually returned to its original size. The most notable change is the rightward shift and increased amplitude of the secondary spike compared to the healthy poles. This complex behavior is due to changes in the chemical composition of the different coexisting insulating materials, the epoxy and thin film. Their respective electrical parameters exhibit opposite effects on the total impedance. The insulation resistance decreases with aging, reducing the impedance. Conversely, aging also reduces the capacitance, increasing the capacitive reactance and consequently the impedance.

The results of the poles of Group B, which are not impregnated with epoxy to secure the turns of the coils, are presented in Figures 5.19, 5.20 and 5.21. Less thermal cycles were executed with the temperature range escalating after each cycle for 6 hours. Similar to Group A, the IR test caused a reduction in impedance without any frequency axis shift. Additionally, after the first thermal round, the impedance increased, indicating a decrease in insulation capacitance, which was also observed in Group A. However, the patterns differ thereafter. In Group B, impedance decreased with prolonged aging time and stress. The Nyquist plot shows a consistent reduction of the ellipsis size with increasing thermal stress. That indicates that when considering only the thin film insulation (no epoxy), the thin film material experiences a rapid drop in capacitance. Subsequently, the resistance decreases at a faster rate than capacitance, leading to a steady and monotonic reduction in total coil impedance.

After the 7 thermal cycles, the poles of Group A had undergone an early voltage breakdown test, using the Megohmmeter. The ramp test mode was selected to produce a ramp-like voltage gradually increasing by 1kV every minute, reaching 15kV after 15 minutes. However, none of the poles withstood such high voltages. Particularly, the setup was achieved by having each pole in full contact with all its turns with a copper bar. One electrode of the Megger was connected to the stripped end of the bar and the other to one stripped terminal of the coil. Hence, a high voltage difference could be generated to test the insulation. As the insulation breakdown approached, the instrument stopped the measurement to prevent a sudden current surge and recorded the breakdown voltage.

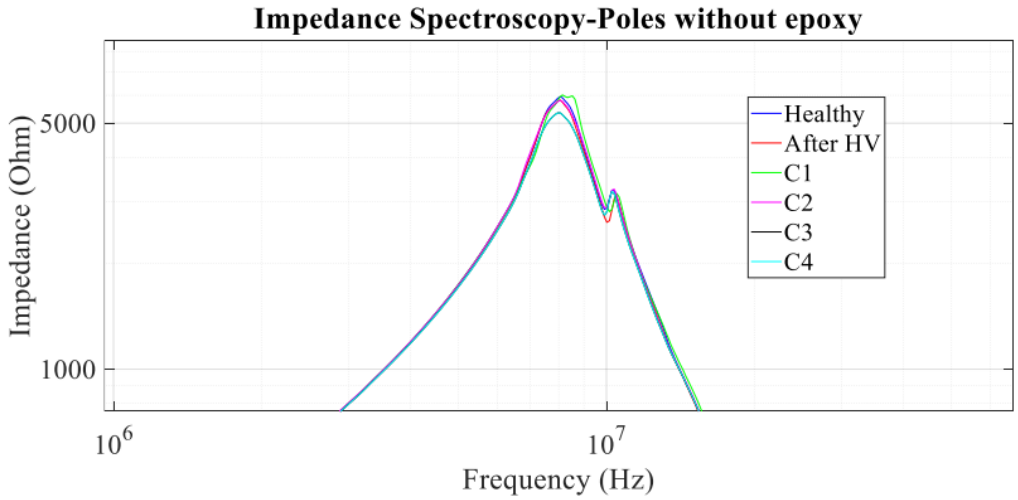

Figure 5.19: Impedance spectroscopy at high frequencies of the Group B poles subjected to thermal cycling stress conditions

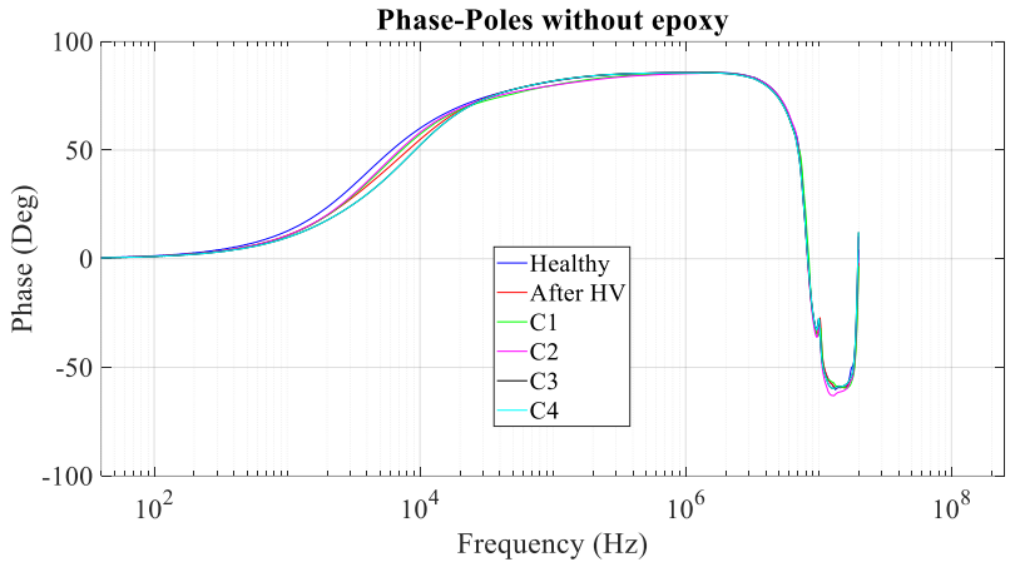

Figure 5.20: Phase diagram of the Group B poles subjected to thermal cycling stress conditions

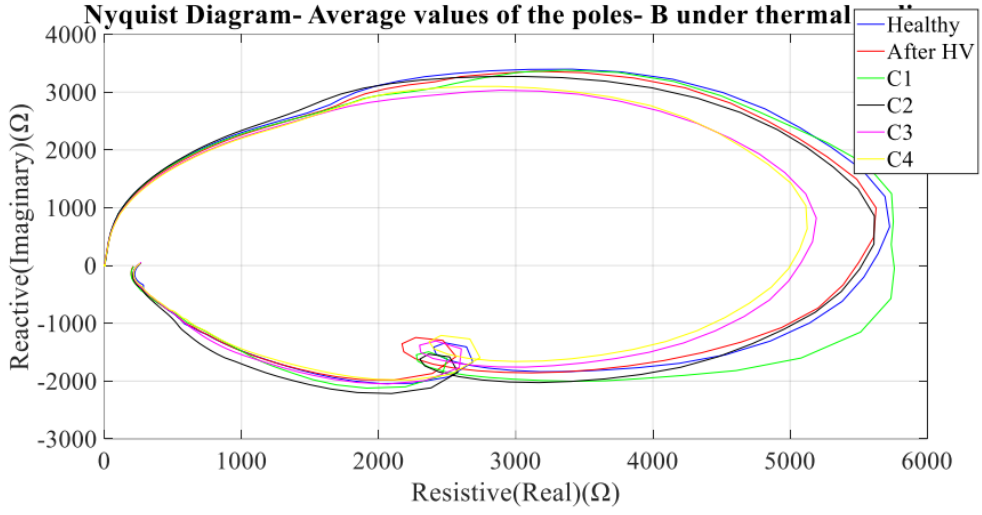

Figure 5.21: Nyquist diagram of the Group B poles subjected to thermal cycling

5.3 Fixed thermal stress

A series of fixed thermal cycles was planned to gather information about the impact of thermal aging on the poles. These tests are designed to isolate the actual thermal degradation resulting from the elevated temperature operation from the thermomechanical effects, characteristic of the thermal cycling stress. The outcomes of this test have been used as a comparative study alongside the thermal cycling stress results. For a precise analysis, six coils from Group A, six coils from Group B and ten copper bars were utilized. All of them were aged at each cycle simultaneously under the same conditions inside the same oven. The oven used was different from the thermal cycling oven, as this could maintain a constant temperature throughout the cycles. The detailed testing process is outlined in Table 5.6.

Poles of Group A, Group B & Copper Bars		
Cycle	**Temperature**	**Duration**
C1	200°C	6 hours
C2	207.5°C	6 hours
C3	215°C	6 hours
C4	220°C	6 hours
C5	225°C	6 hours
C6	230°C	6 hours
C7	240°C	6 hours

Table 5.6: Fixed Thermal Stress Strategy

5.3.1 Setup and bars

The initial thermal cycle was set at the constant temperature of 200°C for six hours. For the second and third cycles, the temperature was elevated by 7.5°C each time, while for the next three cycles, it was progressively increased by 5°C and by 10°C for the last one. Finally, the temperature was set at 240°C, which surpasses the upper limit of the insulation class. All thermal cycles lasted for six hours each. Similar to the thermal cycling tests, the poles and bars were placed inside a clay pot in the oven and two thermometers, one digital and one analog, were continuously monitoring the temperature to ensure that it would remain constant throughout the cycle.

The histograms of the bars of each cycle with their corresponding normal distribution are presented below. The capacitance behavior is complex, preventing any definitive conclusions. The average capacitance does not exhibit any monotonic trend as the temperature increases. However, it has been observed that the minimum capacitance at thermal stresses of 230°C and 240°C is lower than the minimum capacitance observed in the analysis of the healthy poles (Table 5.3).

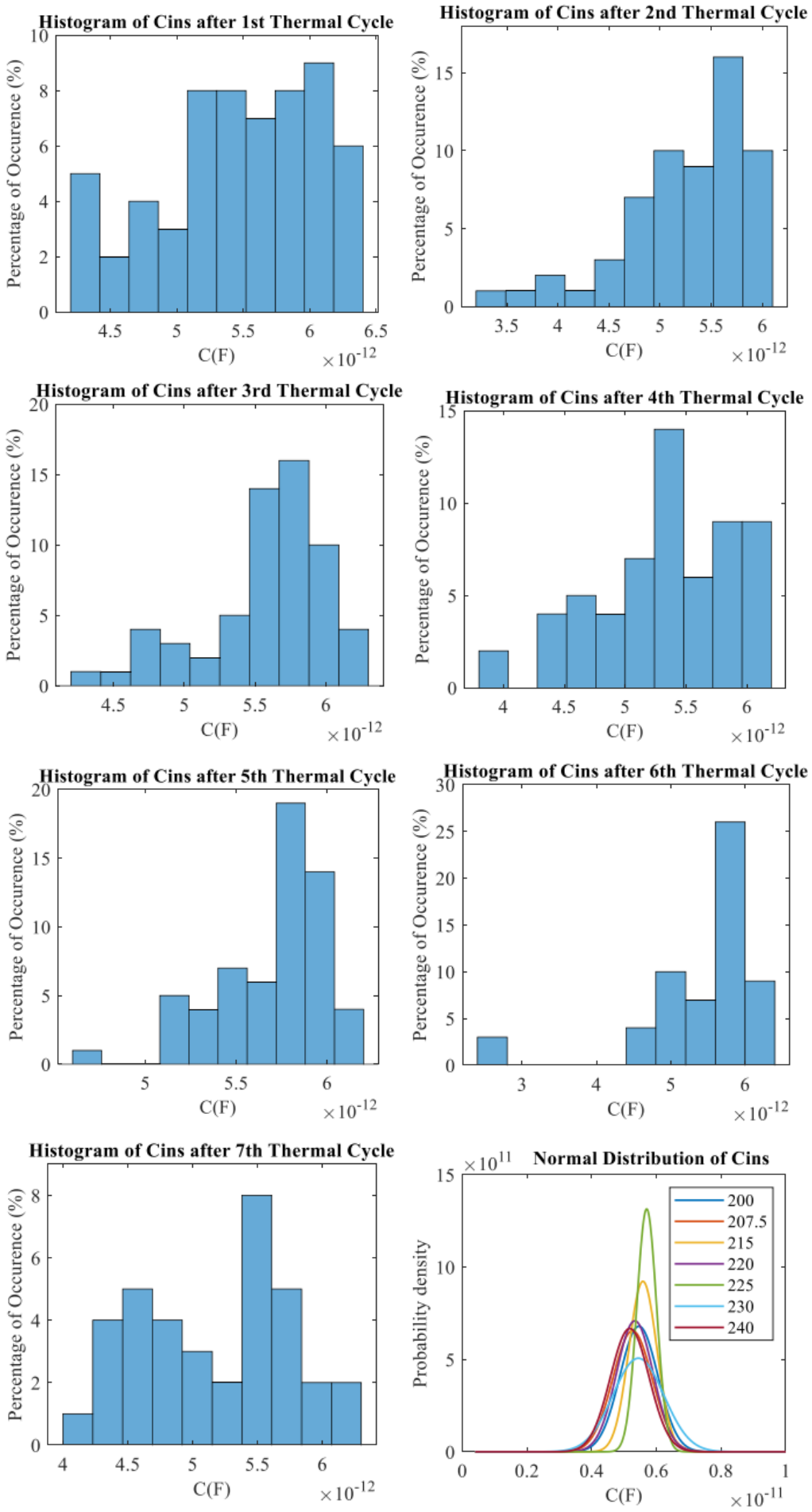

Figure 5.22: Histograms of the various thermal cycles of the 10 copper bars along with their calculated normal distributions

5.3.2 Poles with and without epoxy

The results of impedance spectroscopy for the poles of Group A, displaying both impedance and phase, are presented in Figures 5.23 and 5.25. Similar to thermal cycling, these results reflect the collective behavior of the samples for each cycle. Changes at low frequencies are attributed to the impedance analyzer and the overall wiring of the spectroscopy. Since impedance remains unaffected in frequencies $\leq 10^4$ Hz, the focus again lies on the high frequency components at $\geq 10^6$ Hz. The resonance frequencies vary from 0.65×10^7 to 0.78×10^7 Hz. Thus, a zoomed version of impedance diagrams is provided in Figure 5.24, where the primary and second spikes are located and variations in amplitude and frequency shifts can occur. Also, the Nyquist plot of Figure 5.26 allows for an enhanced understanding of the observed variations.

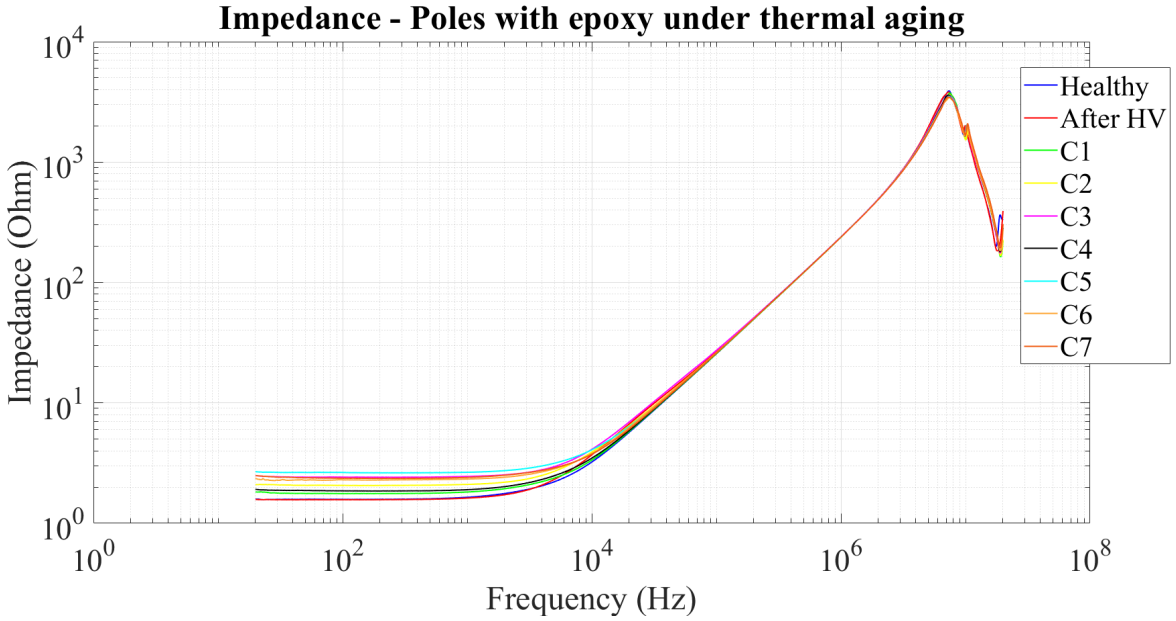

Figure 5.23: Impedance spectroscopy of poles with epoxy under various fixed thermal stresses

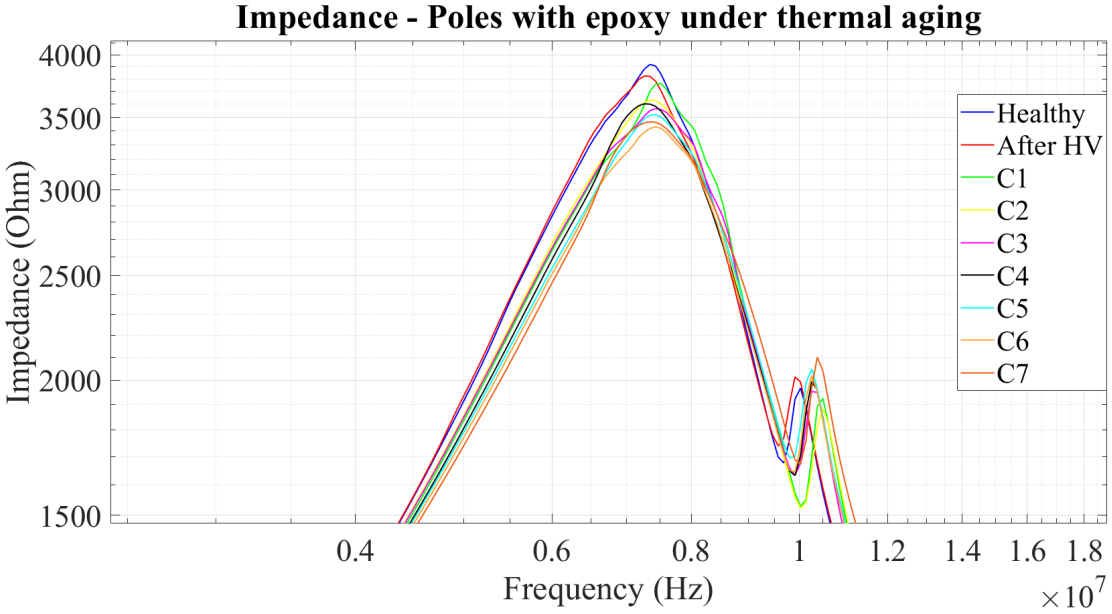

Figure 5.24: Impedance of poles with epoxy at high frequencies

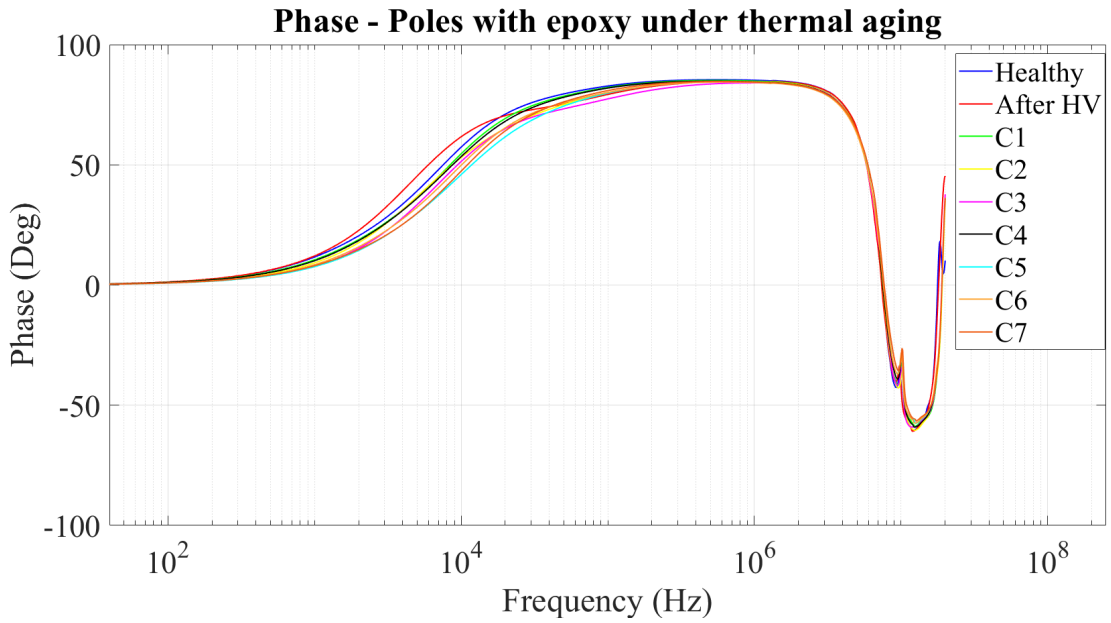

Figure 5.25: Phase of poles with epoxy under various fixed thermal stresses

From the spectroscopy diagrams for the impregnated poles, it can be seen that the IR test resulted in a reduction in impedance amplitude with a concomitant decrease in the radius of the Nyquist ellipsis. Also, the secondary peak amplitude increased and shifted leftwards compared to the unaged state. The first thermal cycle caused a decrease in the impedance, which can be justified by the leftward shift in the x-axis of the Nyquist plot, with a concurrent decrease in amplitude of the secondary spike and shift to the right. The second thermal cycle resulted in a higher decrease of the resistance, and consequently a decrease of both impedance amplitude and Nyquist curve size. In the third thermal cycle, phenomena related to thermal aging become evident. Air bubbles have been introduced in the turn-to-turn insulation, as the Nyquist ellipsis shifted towards the capacitance region meaning the capacitance has been reduced. Simultaneously, the resistance also reduced at a higher rate than the increase of the capacitive reactance, justifying the small decrease of the impedance amplitude and the leftward shift of the secondary spike. Hence, in the fourth thermal cycle, a sharp expansion of the Nyquist ellipsis manifested, while the impedance amplitude slightly increased, implying changes of the dielectric properties of the insulating materials. The fifth thermal cycle dropped the resistance since the selected fixed temperature surpassed the upper-rated limit of the insulation class. Both impedance amplitude and Nyquist curve shrunk in size, although the secondary spike increased and shifted to the right. Similar observations were extracted from the sixth thermal cycle, as the selected temperature caused a greater drop in resistance value, but the secondary spike maximized in amplitude and shifted rightwards. In the final thermal cycle, permanent chemical changes in the dielectric properties of the insulating materials have likely occurred since the Nyquist curve remained stable in the x-axis with a concurrent upward shift in the y-axis due to increased capacitance.

Without the influence of thermomechanical phenomena, the effects of fixed thermal stress on coil impedance become more distinct. There is a continuous decrease in impedance accompanied by a slight rightward shift in spectra, as the temperature of the thermal stress increases. Moreover, the size of the ellipsis decreases after the initial cycle, in the following two and the last three cycles, exhibiting a monotonic reduction, with an additional change in the shape of the ellipsis after the final stress cycle (no more horizontal axial changes). This can be caused by the concurrent changes in the dielectric properties of the epoxy and the thin film insulating materials.

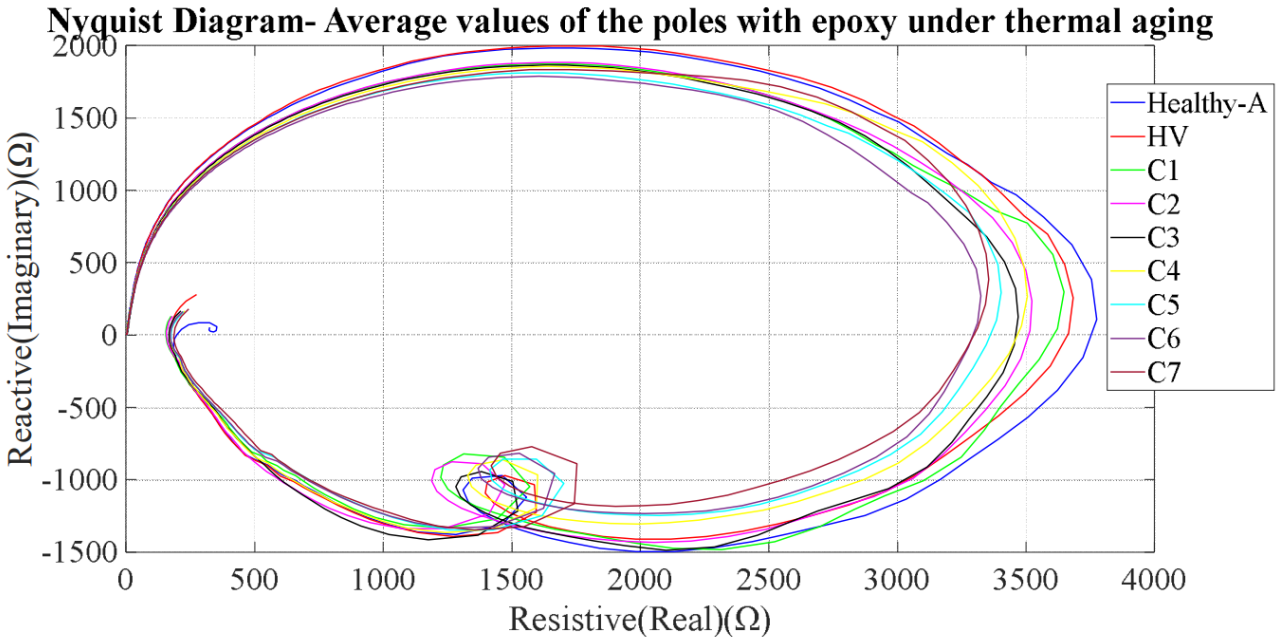

Figure 5.26: Nyquist diagram of poles with epoxy under various fixed thermal stresses

Similarly, the results of the impedance spectroscopy for the poles of Group B, including impedance and phase plots, along with the Nyquist diagram are presented in Figures 5.27, 5.28 and 5.30 respectively. These poles are not impregnated and thereby they exhibit higher impedance. The resonance frequencies of each plot occurred from 0.8×10^7 to 0.86×10^7 Hz for all aging cycles, except for the third cycle in which it was observed at $\approx 0.94 \times 10^7$ Hz. Due to variations observed in high frequencies $\geq 10^6$ Hz, the plot of Figure 5.29 focuses on the impact on the primary and second spike, while the Nyquist plot provides a deeper understanding and comparison with the poles with epoxy.

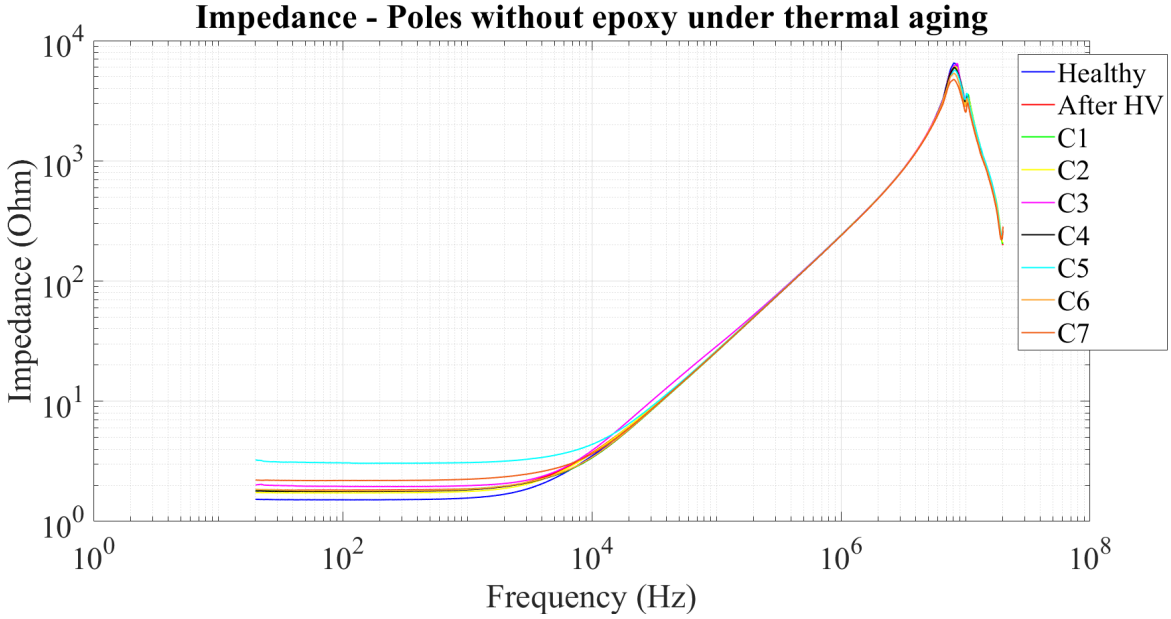

Figure 5.27: Impedance spectroscopy of poles without epoxy under various fixed thermal stresses

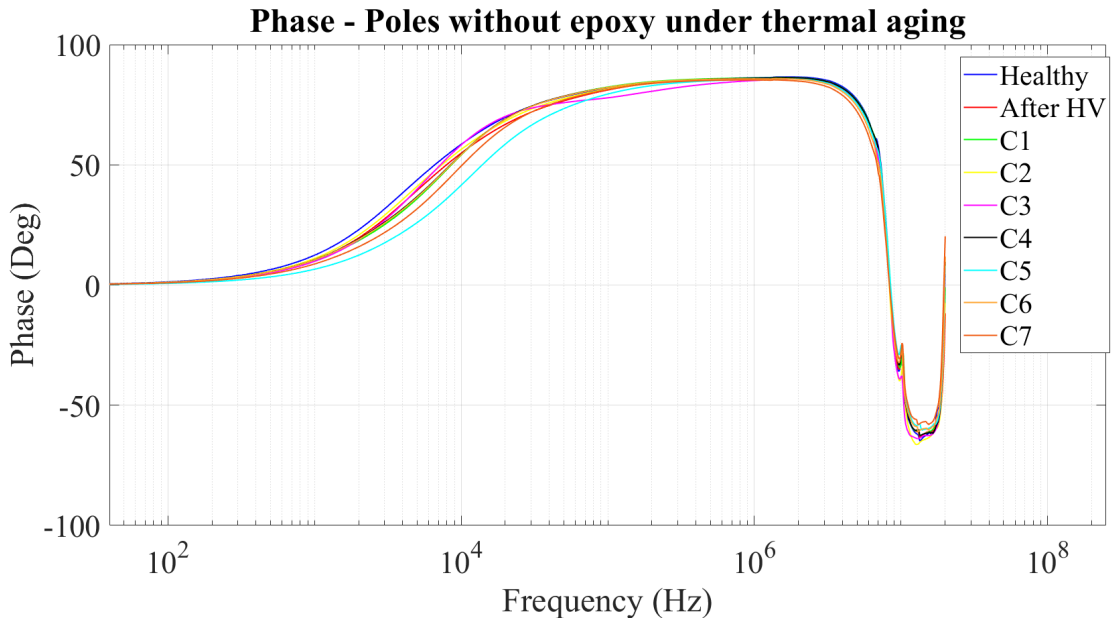

Figure 5.28: Phase of poles without epoxy under various fixed thermal stresses

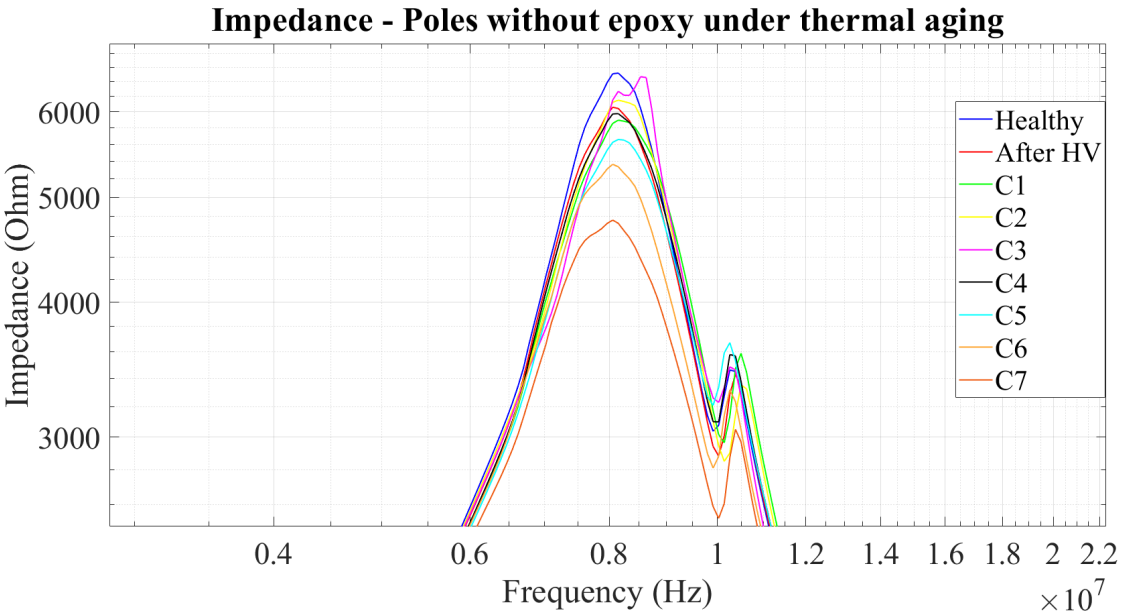

Figure 5.29: Impedance of poles without epoxy at high frequencies

The IR test has the same effects as those previously reported. However, in contrast to the impregnated poles, the non-impregnated poles do not exhibit a monotonic behavior throughout the aging procedure. Below the maximum allowable temperature of 220°C, the impedance does not show a clear pattern. More specifically, the first thermal cycle caused a reduction of the resistance due to thermal aging which led to a decrease of the impedance amplitude and Nyquist curve size. In the second thermal cycle though, the impedance amplitude and Nyquist ellipsis size increased. The absence of epoxy led to the insertion of air between the coil turns, which decreased the capacitance and increased the capacitive reactance, as implied by the downward shift of the Nyquist plot. In the third thermal cycle, the corresponding results of the irregular shapes in both impedance spectroscopy and Nyquist plot showed that probably a high quantity of air was introduced that destroyed the measurement. From that point though, the results started to seem more reasonable. The results of the fourth thermal cycle had slight differences

in resistance from those of the first thermal cycle. In the three last cycles, a clear monotonic reduction of the maximum impedance amplitude is exhibited, which can be associated with the fact that the selected fixed temperature in each cycle surpassed the upper rated limit of the insulation class. Concurrently, a monotonic decrease in the amplitude of the second spike with a rightward shift on the frequency axis is observed. Also, the size of the ellipsis of the Nyquist plot monotonically decreases, which can indicate a decrease in insulation resistance. Particularly, the Nyquist ellipsis of the fifth thermal cycle shifted upwards and leftwards, implying a simultaneous decrease in resistance and increase of capacitance. The dielectric properties of the thin film insulating material likely started to change. Similarly, the impedance dropped in the sixth cycle due to an additional reduction of the resistance and increase of capacitance, while in the final thermal cycle, the impedance reached its minimum as the dielectric properties of the thin film insulating material were probably highly deteriorated.

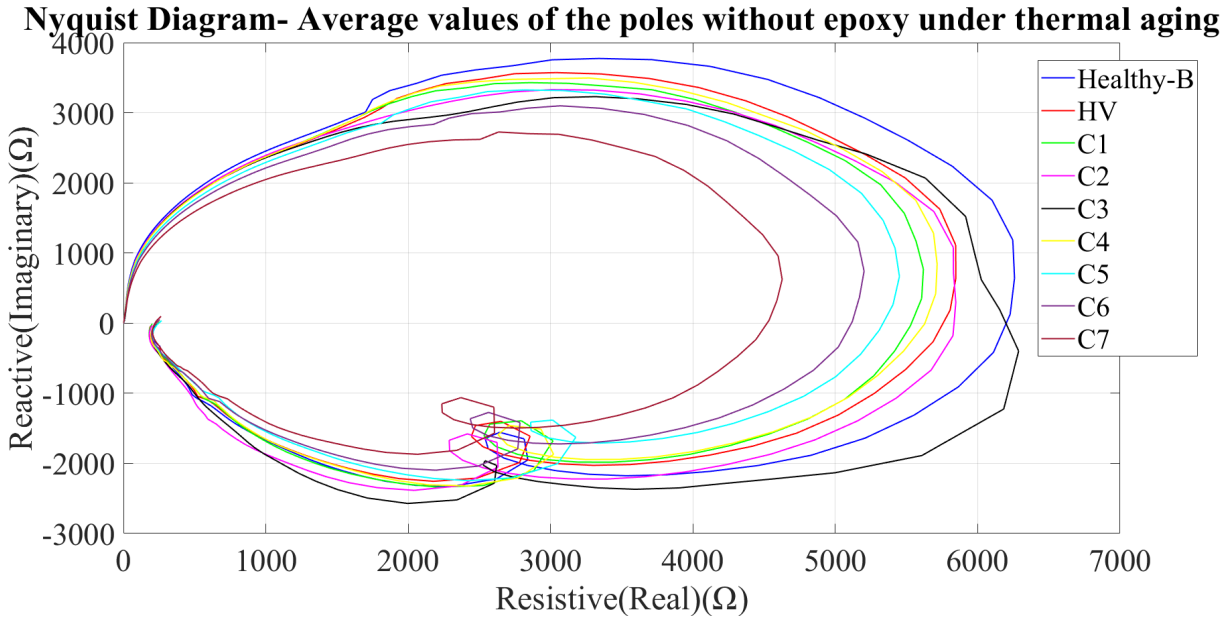

Figure 5.30: Nyquist diagram of poles without epoxy under various fixed thermal stresses

A close examination of Figures 5.31 and 5.32 highlights the significant impact of epoxy on pole impedance. The complex impedance of the impregnated poles is notably lower than that of the non-impregnated poles. For example, the average impedance of the healthy poles of Group B poles is approximately 6500Ω, while the corresponding impedance of the Group A poles is 3900Ω. Such differences are observed in all corresponding aging stages. Moreover, the resonance frequencies of the non-impregnated poles are shifted more to the right compared with the impregnates poles ones. According to the developed model, this outcome indicates that the additional resistance introduced by the epoxy does not significantly affect the total pole impedance. The resistance of the thin film is already compared to the other model parameters. If the epoxy resistance had any substantial effect, the impedance would increase rather than decrease.

However, the epoxy incorporation augments the total capacitance in the model, which results in a reduction of the capacitive reactance and consequently decreases the size of the Nyquist ellipsis. Moreover, air is trapped between the turns of the non-impregnated poles, since the coil turns remain unwelded due to the absence of epoxy. Because of that air, the turn-to-turn capacitance is reduced, leading to a subsequent increase in the capacitive reactance and impedance.

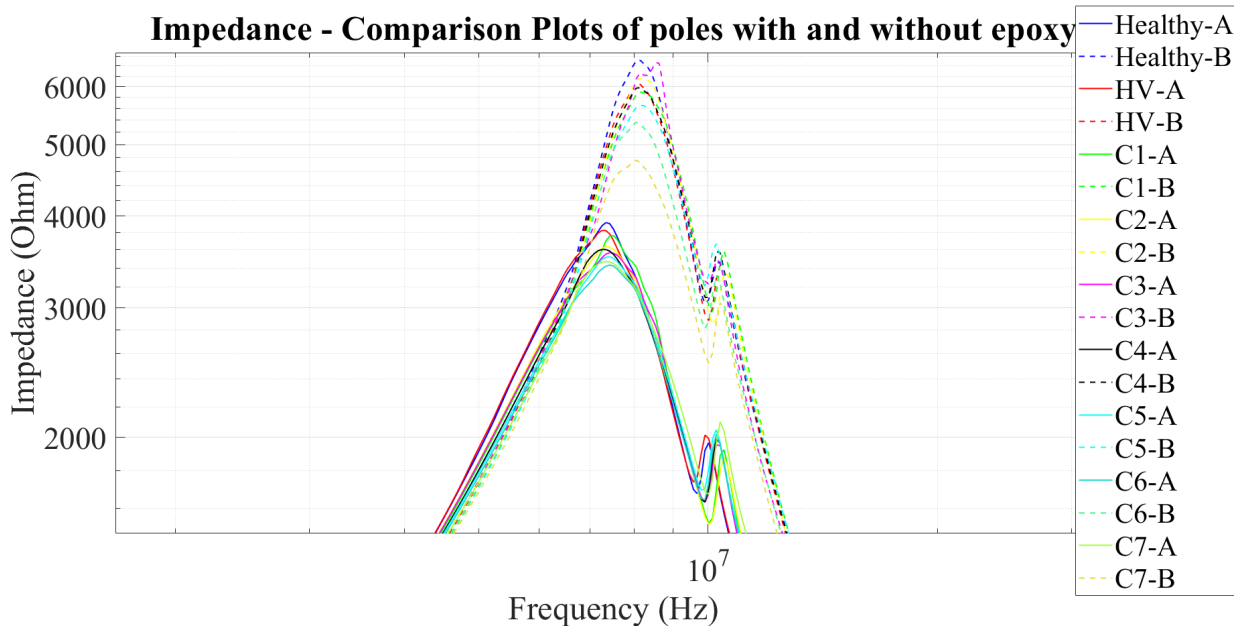

Figure 5.31: Comparative impedance plots between the Group A & B poles subjected to various fixed thermal stresses

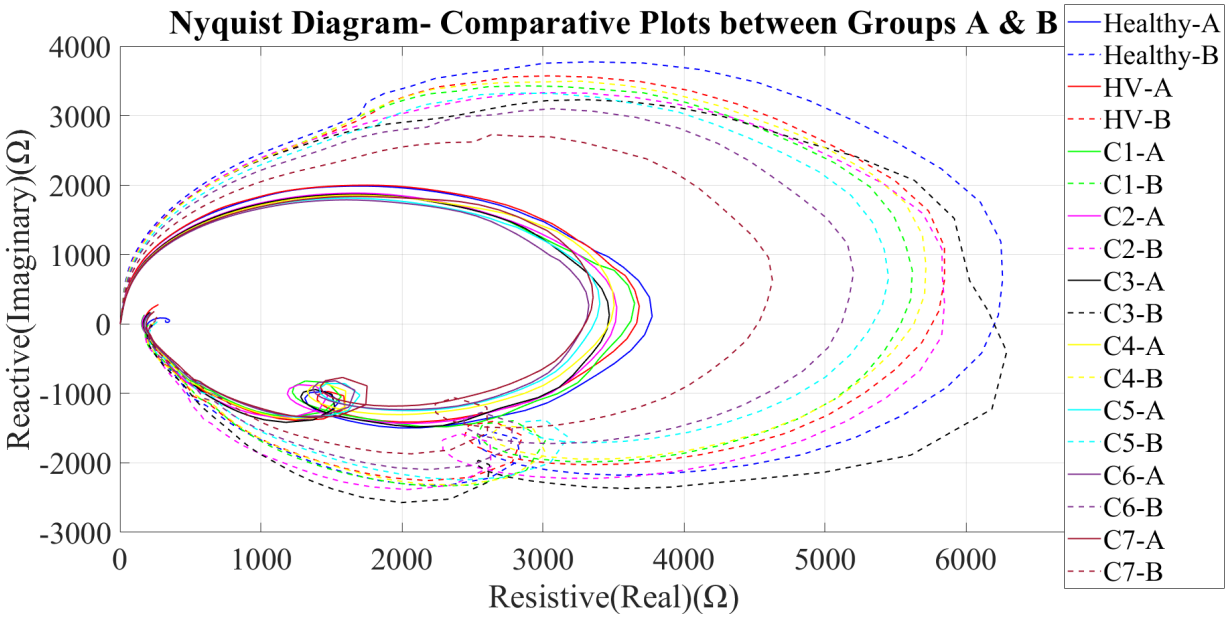

Figure 5.32: Comparative Nyquist plots between the Group A & B poles subjected to various fixed thermal stresses

5.4 Multi-stress analysis

Mechanical stresses are a type of stress that occurs within the environment of the motors. Hence, it is paramount to investigate the impact of mechanical stress. This stress can vary in form and is primarily induced by the different forces produced inside a motor and exerted on the conductors.

A specially designed mechanical accelerator has been constructed to conduct accelerated mechanical stress testing, shown in Figure 5.33. The setup comprises an inverter-fed three-phase induction motor that converts rotational speed into linear oscillation. This pulsating linear movement is transferred through the front shaft to a wagon, which is screwed into four linear bearings. The wagon can hold six poles that are connected in series and short-circuited. The wagon is enclosed inside a C-shaped iron chamber, moving along a track lined with a series of magnets. Consequently, the poles experience mechanical vibration from the induction motor and an induced EMF due to Faraday's law, generating eddy currents and, subsequently, Laplace forces at twice the oscillation frequency.

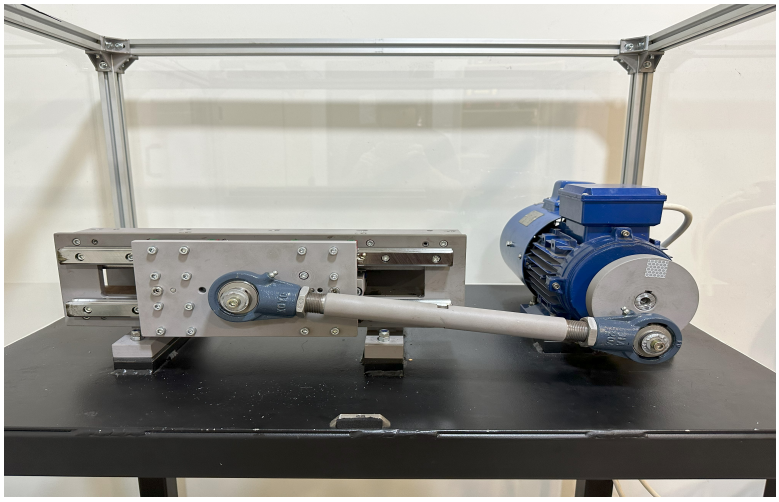

Figure 5.33: The developed setup for mechanical stressing

(a) The inverter used

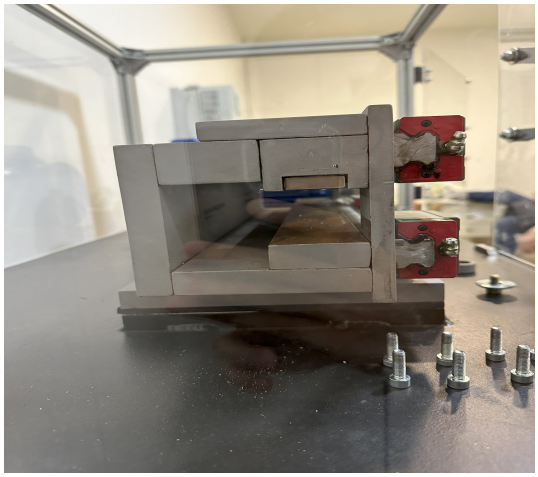

(b) The side view of the iron chamber with the magnets mounted on top

Figure 5.34: The inverter and the iron chamber with the magnets

The mechanical stress acts as an additional stress rotating with fixed thermal stress. Specifically, 18 impregnated poles of Group A have undergone a multi-stress aging. The accelerated

aging process is detailed in Table 5.7. Initially, the poles underwent a thermal cycling stress with the temperature ranging from 200°C to 240°C for 3 hours. Then, the poles were subjected to four cycles consisting of a fixed thermal stress at 225°C followed by a mechanical stress produced by the mechanical accelerator. The inverter used is shown in Fig. 5.34a and was set at 5Hz. This frequency was selected after experimentally finding it was the upper limit that would not cause any damage to the setup and adjusted the rotational speed of the motor, which was transformed into the linear oscillation that mechanically stressed the poles. Each fixed thermal stress lasted for 3 hours, while each mechanical stress lasted for 1 hour. For this type of mixed stressing, 5 thermal and 4 mechanical stressing cycles were executed, with the thermal preceding the mechanical ones.

Stress type	Duration (hours)	Stress parameters
Thermal - Cycling	3	200 - 240°C
Thermal - Fixed	3	225°C
Mechanical	1	5 Hz (motor)
Thermal - Fixed	3	225°C
Mechanical	1	5 Hz (motor)
Thermal - Fixed	3	225°C
Mechanical	1	5 Hz (motor)
Thermal - Fixed	3	225°C
Mechanical	1	5 Hz (motor)

Table 5.7: Stressing procedure of the 18 impregnated poles

The corresponding impedance, phase, and Nyquist plots of the average values of the poles are displayed in Figures 5.35, 5.36, 5.37 respectively. Generally, except for the third mechanical stress cycle, the mechanical stress generally caused an increase in the dimensions of the Nyquist ellipsis. Since the chemical composition of the insulation remained unchanged during this test, no changes in resistance were expected. However, local delamination might have occurred, introducing air bubbles within the coil turns, altering the dielectric constant of the turn-to-turn insulation, thereby decreasing its capacitance and increasing the capacitive reactance. Additionally, for all aging stages, the secondary spike was shifted to the right compared to the healthy condition and its amplitude significantly decreased during the final stressing cycles, coinciding with the maximum size of the ellipsis.

More specifically, the IR test manifested an elevation in both resistance and capacitance, leading to increased impedance amplitude. The first thermal cycle led to a decrease of resistance and therefore a reduction of impedance amplitude and Nyquist ellipsis size. During the second thermal cycle, the Nyquist curve shifted towards the capacitive region, which indicates a reduction of the capacitance due to air introduced within the poles. The first mechanical stress cycle caused an increase in the impedance amplitude due to the decrease of the capacitance as seen from the downward shift of the Nyquist plot. The third thermal cycle resulted in a decrease of the resistance due to thermal aging, thus a decrease of both impedance amplitude and Nyquist ellipsis size. The second mechanical stress cycle led to an additional reduction of capacitance and thereby an increase of both impedance amplitude and the dimensions of the Nyquist plot. In the fourth thermal cycle, the impedance amplitude significantly increased with a simultaneous sharp expansion of the Nyquist curve. It is showcased that local delamination is likely to have occurred as air bubbles increased the resistance. Hence, the impedance did not increase during the third mechanical stress cycle but instead decreased, although the increase of capacitive reactance, as the mechanical oscillations created cracks in the insulation. Afterwards, the behavior of the pole changed, as in the final thermal stress cycle the impedance and phase rapidly increased with a concurrent sharp expansion of the Nyquist ellipsis.

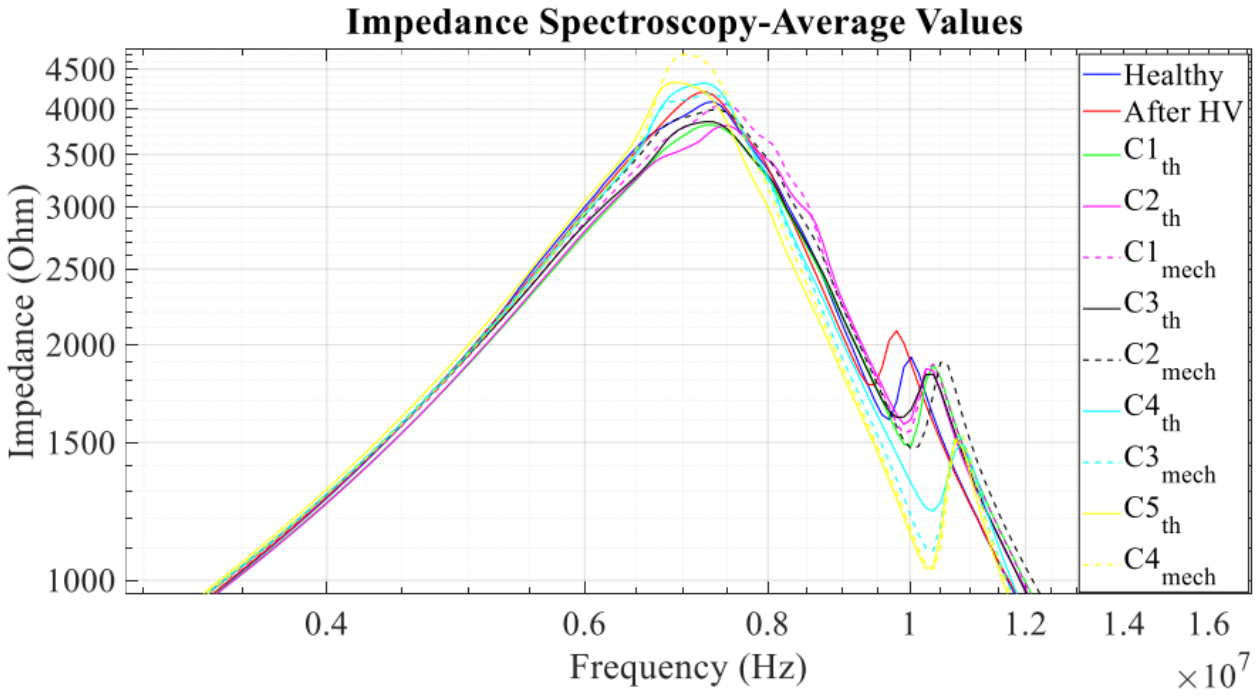

Figure 5.35: Comparative impedance plot between the 18 impregnated poles undergoing mixed stressing

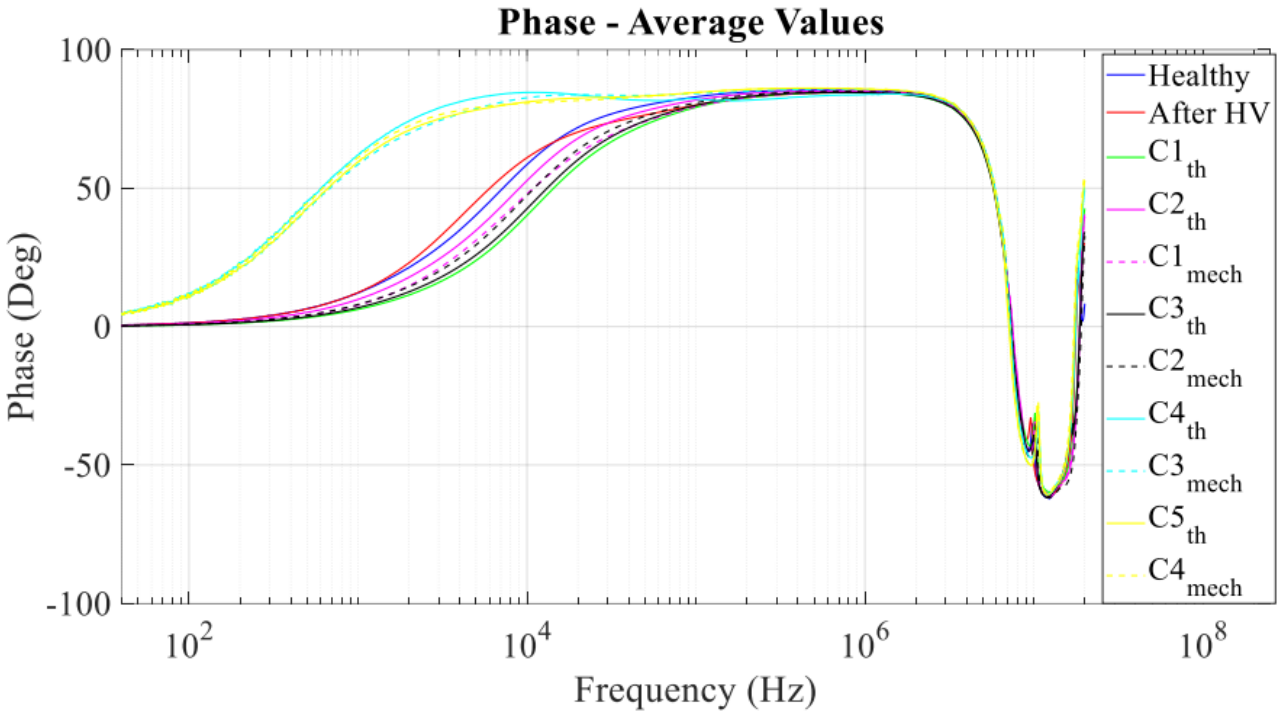

Figure 5.36: Comparative phase plot between the 18 impregnated poles undergoing mixed stressing

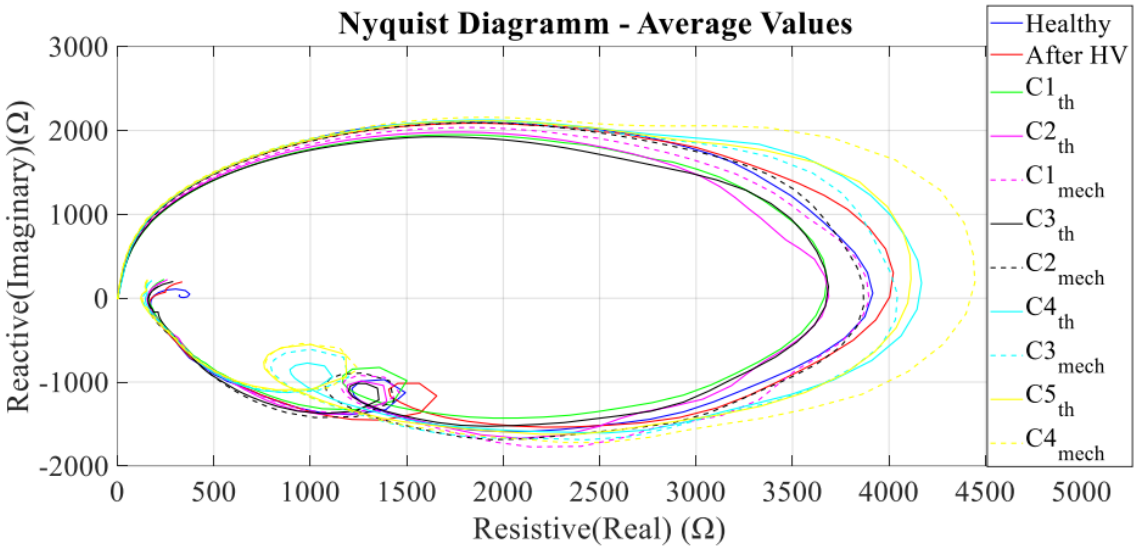

Figure 5.37: Comparative Nyquist plot between the 18 impregnated poles under mixed stress

A second series, consisting of 6 poles, underwent a multi-stress aging procedure, outlined in Table 5.8. This time the mechanical stress cycles precede the fixed thermal stresses, having in total 5 mechanical cycles and four fixed thermal cycles with an initial thermal cycling stress. These tests were conducted separately to verify the conclusions from the analysis of the previous team of poles and to observe the behavior of the secondary spike in impedance spectroscopy during the final stages of degradation.

Stress type	Duration (hours)	Stress parameters
Thermal - Cycling	3	200 - 240°C
Mechanical	1	5 Hz (motor)
Thermal - Fixed	3	225°C
Mechanical	1	5 Hz (motor)
Thermal - Fixed	3	225°C
Mechanical	1	5 Hz (motor)
Thermal - Fixed	3	225°C
Mechanical	1	5 Hz (motor)
Thermal - Fixed	3	225°C
Mechanical	1	5 Hz (motor)

Table 5.8: Stressing procedure of the 6 impregnated poles

The average impedance plots with their corresponding phase plots and Nyquist curves are displayed in Figures 5.38a, 5.38b and 5.39 respectively. The findings indicated a strong similarity between the two groups. The phase variations at low frequencies between the early and late stages of degradation in both teams are due to the different cables used to connect samples, which has a minor effect on the Nyquist curve. Additionally, the impedance spectroscopy of the 6 impregnated poles revealed a critical threshold for the coil's health. Between every cycle of mechanical and thermal stress, poles underwent an early breakdown voltage, using the Megohmmeter, recording the corresponding breakdown resistance of the coils. After the high-voltage test, the secondary spike moved to the left of the healthy condition, but the subsequent aging cycles forthwith shifted it to the right. Up until the third thermal cycle, the amplitude of the secondary spike remained relatively stable, however in the third mechanical stress cycle its amplitude greatly dropped. In the last four degradation stages, the amplitude was significantly

reduced, accompanied by a pronounced local minimum. This consistent pattern across both teams indicated a potential critical threshold that requires further experimental procedures.

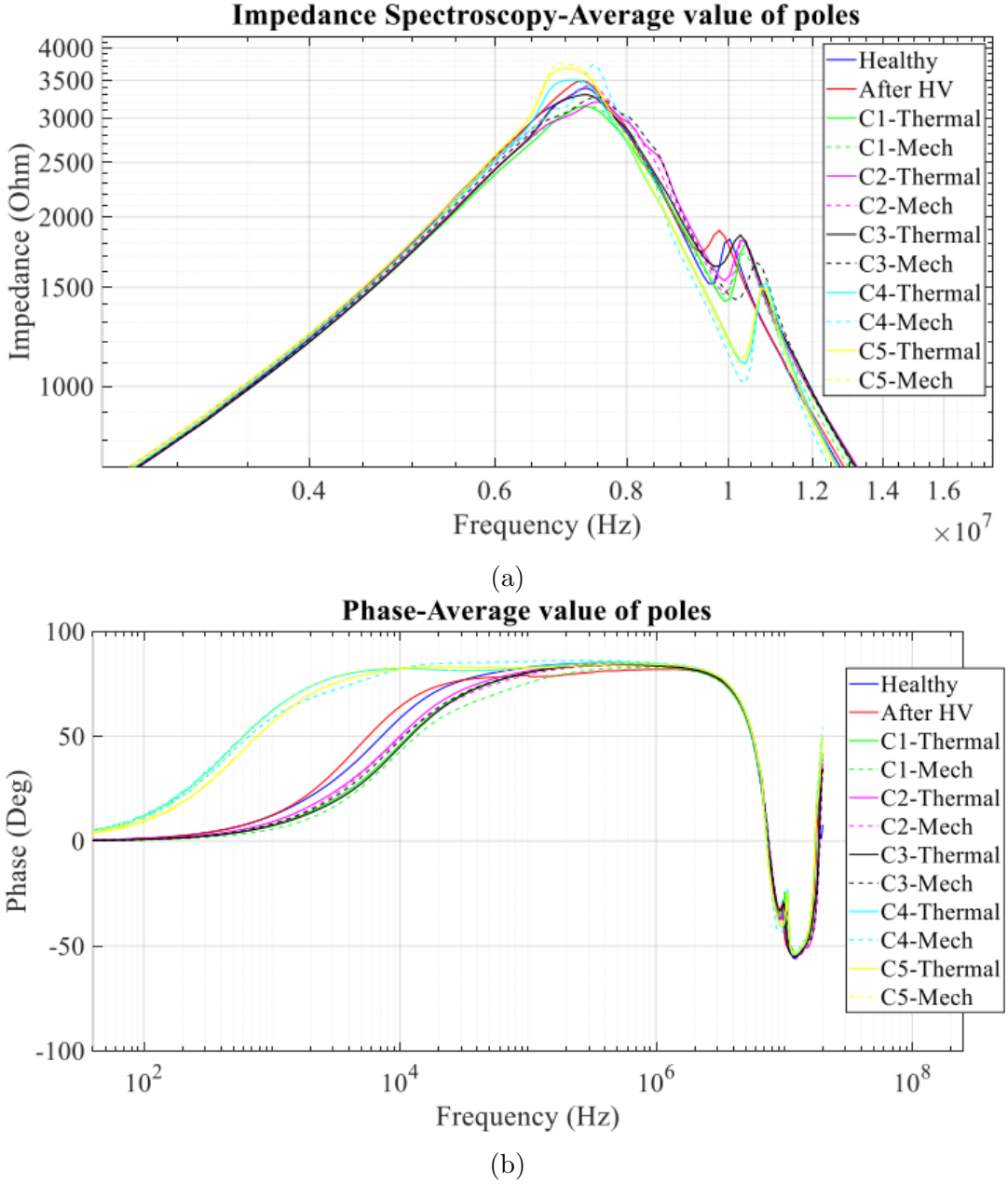

Figure 5.38: Comparative impedance and phase plots between the 6 impregnated poles undergoing the 2nd mixed stressing

Finally, ensuring full contact between the copper bar and each pole, a final breakdown voltage cycle was applied to both groups of poles subjected to consecutive thermal and mechanical stressing cycles. These results were compared to the readings of six healthy, unaged poles with the same characteristics that underwent solely a high-voltage test. The corresponding histogram and normal distribution are displayed in Figure 5.40. A consistent reduction of the breakdown voltage along with an increase in standard deviation is evident for aged poles. This rise in standard deviation is due to the inclusion of more aged poles rather than unaged poles and the occurrence of significantly lower breakdown voltages in some aged poles. The shift of the normal distribution towards lower voltages identified the monotonic decrease in breakdown voltage for aged samples. This outcome validated the effectiveness of the multistress accelerated aging methods.

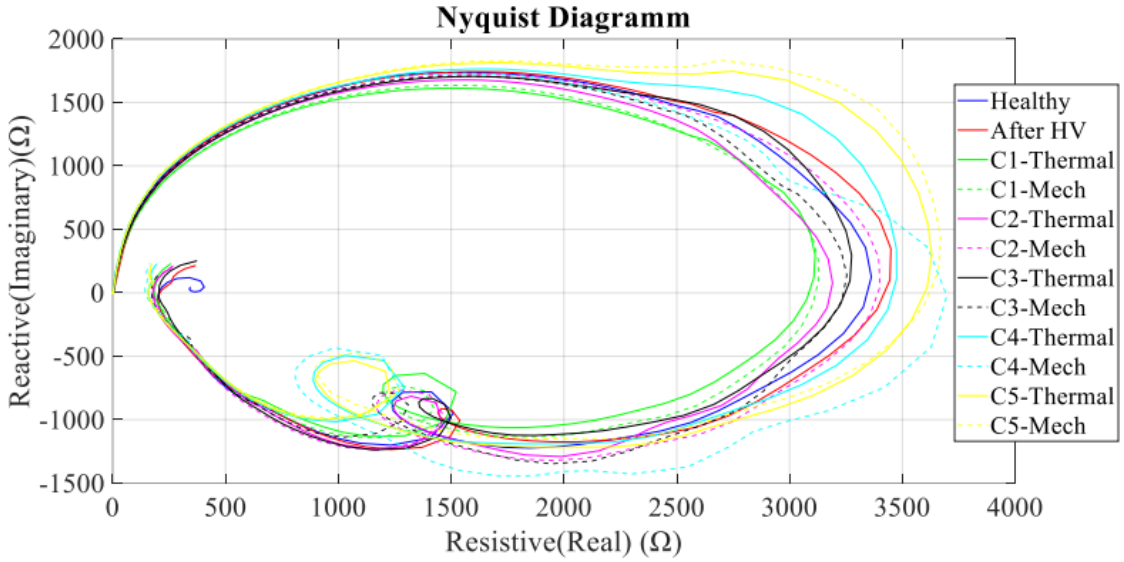

Figure 5.39: Comparative Nyquist diagram between the 6 impregnated poles undergoing the 2nd mixed stressing

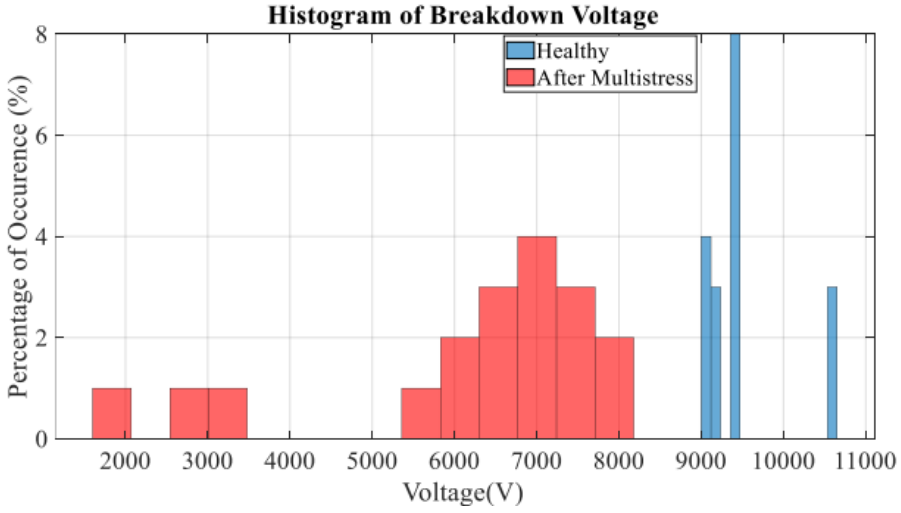

(a)

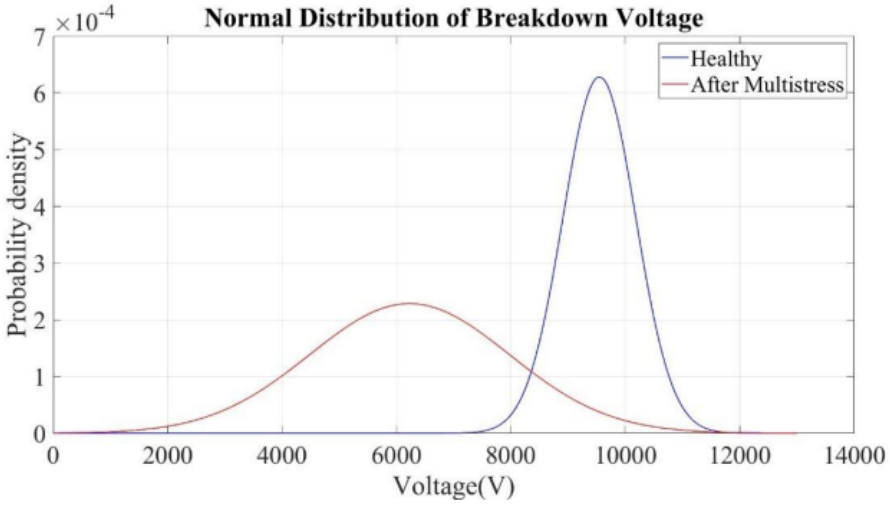

(b)

Figure 5.40: a)Histogram and b)Normal distribution of the breakdown voltage of the poles subjected to consecutive thermal and mechanical stress cycles compared to healthy samples

6 Conclusion and recommendations for future work

The realization of this thesis has led to some significant outcomes, concerning the model and the experimental results. The development of the model has greatly enhanced the understanding of various underlying aging conditions, allowing significant progress to be made in a short period. Despite that, the project is subject to future efforts for further examination.

6.1 Discussion & Conclusion

First, an accurate equivalent circuit has been constructed to represent the poles with their mounted armature coils of a permanent magnet synchronous axial flux motor through experimental testing. A library of potential manufacturing faults was developed by leveraging this established model, serving as a valuable tool for both prognosis and diagnosis. In the context of prognosis, the model allows for predictions for changes in the dielectric characteristics of the pole as it degrades. For diagnosis, this library facilitates the identification of these faults through the application of impedance spectroscopy and the generation of the corresponding Nyquist diagrams. The specific element of the equivalent circuit responsible for the deviations in resistance and capacitance can be determined. Moreover, this model facilitated the investigation of material and manufacturing tolerances. This analysis was achieved through statistical evaluation of measured parameters from a significant population of pole samples.

Changes in insulation resistance appear to have a negligible effect on the impedance spectroscopy measurements unless an actual fault arises within the system. An IR fault leads to an increase in angle. Conversely, changes in the chemical composition of the insulating materials significantly affect the impedance spectroscopy records. This is primarily manifested through variations observed in the respective capacitance values due to the absorption current.

Impedance spectroscopy plots include a main maximum amplitude and a second local maximum impedance (high-frequency resonance spike) at high frequencies, which both contain significant diagnostic information about the insulation condition. Specifically, alterations in the second peak are indicative of insulation cracks, delaminations, and detachments of the PAI insulation from the copper windings. Nyquist plots offer a valuable tool for visualizing overall changes within the impedance spectra. This graphical representation combines both impedance and phase information across the frequency range, providing a comprehensive overview of the dielectric behavior.

While impedance spectroscopy is promising for identifying manufacturing defects within individual poles, its effectiveness diminishes with the degradation phenomena involved. This limitation arises from the inherent complexity of the Nyquist plot, which reflects the interplay of multiple parameters that can change simultaneously and potentially mask the effects of degradation. Notably, the Nyquist ellipsis of a population of aged poles can closely resemble those of healthy poles in terms of size and shape. However, breakdown voltage measurements indicate a substantial degradation of the insulation properties.

A clear monotonic relationship between impedance spectroscopy results and the degradation levels of the poles was only observed under specific conditions: fixed thermal stress applied to non-impregnated poles. When thermal cycling and impregnated poles were involved, the relationship between the spectroscopy results and the degradation of the poles became non-monotonic. This complexity is attributed to the multifaceted chemical composition of the different, co-existing insulating materials (epoxy and PAI) of the impregnated poles. On one side, the aging process leads to a reduction in the insulation resistance and thereby to a decrease in the total impedance magnitude. On the other side, aging also typically results in a decrease in the insulation capacitance. This translates to an increase in the capacitive reactance and subsequently to an increase in the total impedance. Moreover, fixed thermal stress may induce

discoloration of the poles as a consequence of chemical changes that occur during the thermal stress.

Electromechanical stress can exacerbate material weakening, particularly following prior thermal stress. This phenomenon is likely linked to initiating or propagating delaminations within the coil at an early stage. Once the pole reaches a critical degradation state, the electromechanical stress tends to increase the size of the Nyquist ellipsis. This is a direct result of delamination effects, which cause a decrease in insulation capacitance and, consequently, an increase in capacitive reactance.

The high-voltage testing has shown that the insulation became more susceptible to breakdown after exposure to electromechanical stress. While the average breakdown voltage of the material might not exhibit a significant change, the mechanical stress appears to introduce weak spots within the previously thermally degraded insulation. These weak spots can lead to premature breakdown events at considerably lower voltages.

The fixed thermal stress lowered the required breakdown voltage as anticipated and caused changes to the standard deviation of the sample distribution compared to the healthy samples as well. This change was not observed when the multi-stress procedure involved thermal cycling stress instead of fixed thermal aging, where the standard deviation of the normal distribution of the samples remained similar to that of the healthy cases.

The analysis suggests that early faults may be more likely attributed to phenomena involving adjacent poles rather than inter-turn short circuits within the winding. This conclusion is supported by the observation that the only broken pole exhibits such a failure mode. An additional protective insulation layer around the coil before the impregnation process could be proposed to protect the windings from short circuits.

6.2 Future work

Although the derived model is more analytical than those proposed in existing literature, it can be further enhanced for a more complex and precise representation of the pole. This model will incorporate the individual complex inductance between each turn and the core. This refined model has the potential to reveal the location of faults within the winding with greater accuracy and could be used for degradation mechanisms analysis.

A series of degradation studies involving adjacent poles could be conducted. This research would provide valuable insights into the mechanisms responsible for turn-to-turn short circuits within the windings.

Extended fixed thermal cycles with longer durations are recommended to gain deeper insights into the behavior of the poles under fixed thermal stress. This approach will likely yield more pronounced and severe degradation effects, facilitating a more comprehensive understanding of the failure mechanisms. Exploring the combined effects of various thermo-electrical-mechanical stresses is crucial for a holistic perspective on complex degradation processes. By investigating the interplay of these stresses, the research can provide more accurate conclusions about the longevity and integrity of the poles under realistic operating conditions.

References

[1] G. Nanda and N. C. Kar, "A survey and comparison of characteristics of motor drives used in electric vehicles," *2006 Canadian Conference on Electrical and Computer Engineering*, May 2006.

[2] N. Hashernnia and B. Asaei, "Comparative study of using different electric motors in the electric vehicles," *in International Conference on Electrical Machines*, Sept. 2008.

[3] D. S. Yadav and M. Manisha, "Electric propulsion motors: A comparative review for electric and hybrid electric vehicles," *in 2022 IEEE International Conference on Distributed Computing and Electrical Circuits and Electronics (ICDCECE)*, 2022.

[4] M. YILDIRIM, M. POLAT, and H. KÜRÜM, "A survey on comparison of electric motor types and drives used for electric vehicles," *in 16th International Power Electronics and Motion Control Conference and Exposition*, Sept. 2014. Antalya, Turkey.

[5] K. Rahman, B. Fahimi, G. Suresh, A. Rajarathnam, and M. Ehsani, "Advantages of Switched Reluctance motor applications to EV and HEV: design and control issues," *IEEE Transactions on Industry Applications*, vol. 36, no. 1, pp. 111–121, 2000.

[6] C.-A. Bilaţiu, S. I. Cosman, R.-A. Marţiş, C. S. Marţiş, and S. Morariu, "Identification and evaluation of electric and hybrid vehicles propulsion systems," *2019 Electric Vehicles International Conference (EV)*, Oct. 2019.

[7] M. Zeraoulia, M. E. H. Benbouzid, and D. Diallo, "Electric motor drive selection issues for HEV propulsion systems: A comparative study," *in IEEE Transactions on Vehicular Technology*, vol. 55, no. 2, pp. 1756 – 1764, Nov. 2006.

[8] N. Bianchi, S. Bolognani, E. Carraro, M. Castiello, and E. Fornasiero, "Electric vehicle traction based on synchronous reluctance motors," *in IEEE TRANSACTIONS ON INDUSTRY APPLICATIONS*, vol. 52, no. 6, pp. 4762 – 4769, Nov. - Dec. 2016.

[9] S. Taghavi and P. Pillay, "A sizing methodology of the synchronous reluctance motor for traction applications," *IEEE JOURNAL OF EMERGING AND SELECTED TOPICS IN POWER ELECTRONICS*, vol. 2, no. 2, pp. 329 – 340, June 2014.

[10] M. Wang and Z. Chen, "Research on permanent magnet structure of permanent magnet synchronous motor for electric vehicle," *in 2022 2nd International Conference on Electrical Engineering and Control Science (IC2ECS)*, Dec. 2022.

[11] Q. Chen, H. Wang, Z. Sang, W. Qian, G. Liu, G. Xu, and Z. Liu, "A multi-mode high-efficiency fault-tolerant permanent magnet machine," *IEEE Transactions on Energy Conversion*, vol. 38, no. 3, pp. 1999 – 2010, 2023.

[12] S. Prabhu, V. Arun, M. Balaji, V. Kalaimagal, A. Manikandan, and V. Chandrasekar, "Electromagnetic analysis on brushless DC hub motor for electrified transportation systems," *2023 9th International Conference on Electrical Energy Systems (ICEES)*, March 2023.

[13] Z. Q. Zhu and D. Howe, "Electrical machines and drives for electric, hybrid, and fuel cell vehicles," *Proceedings of the IEEE*, vol. 95, no. 4, pp. 746–765, 2007.

[14] J. West, "DC, induction, reluctance and PM motors for electric vehicles," *Power Engineering Journal*, vol. 8, pp. 77–88, 1994.

[15] A. S. Patil and R. T. Ugale, "Design and comparative analysis of axial flux and radial flux permanent magnet brushless DC motor for a 2-wheeler electric vehicle application," in *2022 IEEE Conference on Interdisciplinary Approaches in Technology and Management for Social Innovation (IATMSI)*, pp. 1–4, 2022.

[16] N. Polater, T. Kamel, and P. Tricoli, "Torque comparison of surface mount and interior permanent magnet synchronous motor for railway applications," in *2021 IEEE 15th International Conference on Compatibility, Power Electronics and Power Engineering (CPE-POWERENG)*, pp. 1–6, 2021.

[17] D. D. Hanselman, *Brushless Permanent Magnet Motor Design, Second Edition.* The Writers' Collective, 2003.

[18] A. Naina, S. Paryani, and S. S. N. Jani, "Comparison between surface-mounted and interior PM motor for EV application," in *2021 International Conference on Intelligent Technologies (CONIT)*, pp. 1–6, 2021.

[19] G. Pellegrino, A. Vagati, P. Guglielmi, and B. Boazzo, "Performance comparison between surface-mounted and interior PM motor drives for electric vehicle application," *IEEE Transactions on Industrial Electronics*, vol. 59, no. 2, pp. 803–811, 2012.

[20] S. V. Pawar and R. T. Ugale, "Comparative analysis of positive and negative salient IPMSM drive performance," in *2022 IEEE Conference on Interdisciplinary Approaches in Technology and Management for Social Innovation (IATMSI)*, pp. 1–6, 2022.

[21] R. Gudivada, K. K. Bodnapu, and K. R. Vavillapalli, "Virtual characterization of interior permanent magnet (IPM) motor for EV traction applications," in *2017 IEEE Transportation Electrification Conference (ITEC-India)*, pp. 1–4, 2017.

[22] A. Vagati, G. Pellegrino, and P. Guglielmi, "Comparison between SPM and IPM motor drives for EV application," in *The XIX International Conference on Electrical Machines - ICEM 2010*, pp. 1–6, 2010.

[23] T. Woolmer and M. McCulloch, "Analysis of the yokeless and segmented armature machine," in *2007 IEEE International Electric Machines & Drives Conference*, vol. 1, pp. 704–708, 2007.

[24] S. Huang, M. Aydin, and T. Lipo, "TORUS concept machines: pre-prototyping design assessment for two major topologies," in *Conference Record of the 2001 IEEE Industry Applications Conference. 36th IAS Annual Meeting (Cat. No.01CH37248)*, vol. 3, pp. 1619–1625, 2001.

[25] B. Zhang, T. Seidler, R. Dierken, and M. Doppelbauer, "Development of a yokeless and segmented armature axial flux machine," *IEEE Transactions on Industrial Electronics*, vol. 63, no. 4, pp. 2062–2071, 2016.

[26] A. Allca-Pekarovic, P. J. Kollmeyer, A. Forsyth, and A. Emadi, "Experimental characterization and modeling of a YASA P400 axial flux PM traction machine for electric vehicles," in *2022 IEEE Transportation Electrification Conference & Expo (ITEC)*, pp. 433–438, June 2022.

[27] A. Allca-Pekarovic, P. J. Kollmeyer, A. Forsyth, and A. Emadi, "Experimental characterization and modeling of a YASA P400 axial flux PM traction machine for performance analysis of a Chevy Bolt EV," *IEEE Transactions on Industry Applications*, pp. 1–11, Dec. 2023.

[28] G. Wang, Y. Wang, Y. Gao, W. Hua, Q. Ni, and H. Zhang, "Thermal model approach to the YASA machine for in-wheel traction applications," *Energies*, vol. 15, p. 5431, 07 2022.

[29] F. Blázquez, E. Rebollo, C. A. Platero, and F. R. Blánquez, "Design and construction of a laboratory bench system for the teaching and training of engineers on diagnostics of permanent magnet motors," in *2015 IEEE 10th International Symposium on Diagnostics for Electrical Machines, Power Electronics and Drives (SDEMPED)*, pp. 131–137, 2015.

[30] X. Wu, Y. Zhang, Z. Mao, B. Jiang, and Y. Shi, "Fault diagnosis for stator inter-turn short circuit fault of traction motors under closed-loop structure," in *2019 CAA Symposium on Fault Detection, Supervision and Safety for Technical Processes (SAFEPROCESS)*, pp. 76–81, 2019.

[31] S. B. Lee, G. C. Stone, J. A. Antonino-Daviu, K. N. Gyftakis, E. G. Strangas, P. Maussion, and C. A. Platero, "Condition monitoring of industrial electric machines: State of the art and future challenges," *IEEE Industrial Electronics Magazine*, vol. 14, pp. 158–167, 2020.

[32] B. Ebrahimi, J. Faiz, and M. Javan Roshtkhari, "Static-, dynamic-, and mixed-eccentricity fault diagnoses in permanent-magnet synchronous motors," *Industrial Electronics, IEEE Transactions on*, vol. 56, pp. 4727 – 4739, 12 2009.

[33] J. Portos, K. Dean Garner, B. Parker, and J. Cannon, "Most common mechanisms and reasons for electric motor failures in petrochemical industry," in *2015 IEEE Petroleum and Chemical Industry Committee Conference (PCIC)*, pp. 1–11, 2015.

[34] F. Feilong, C. Ming, and L. Qian, "Naturally-induced early aviation bearing fault test and early bearing fault detection," in *2021 Global Reliability and Prognostics and Health Management (PHM-Nanjing)*, pp. 1–6, 2021.

[35] B. V. Hecke, Y. Qu, D. He, and E. Bechhoefer, "A new spectral average-based bearing fault diagnostic approach," *Springer, Journal of Fail. Anal. And Prevent.*, vol. 14, no. 3, pp. 354–362, 2014.

[36] G. Niu, X. Dong, and Y. Chen, "Motor fault diagnostics based on current signatures: A review," *IEEE Transactions on Instrumentation and Measurement*, vol. 72, pp. 1–19, 2023.

[37] S. K. Kommuri, Y. Park, and S. B. Lee, "Online compensation of mechanical load defects with composite control in PMSM drives," *IEEE/ASME Transactions on Mechatronics*, vol. 26, no. 3, pp. 1392–1400, 2021.

[38] Y. Rao, Y. Wang, and W. Wang, "A simplified modeling and analysis method for interturn short-circuit fault of permanent magnet synchronous motor," in *2023 26th International Conference on Electrical Machines and Systems (ICEMS)*, pp. 4450–4455, 2023.

[39] V. Climente-Alarcon, J. A. Antonino-Daviu, M. Riera-Guasp, and M. Vlcek, "Induction motor diagnosis by advanced notch FIR filters and the Wigner–Ville distribution," *IEEE Transactions on Industrial Electronics*, vol. 61, no. 8, pp. 4217–4227, 2014.

[40] K. V. Tejan and B. S. Rajpurohit, "Open-circuit faults diagnosis in inverter switches using current control prediction method for PMSM drives," in *2023 IEEE IAS Global Conference on Renewable Energy and Hydrogen Technologies (GlobConHT)*, pp. 1–6, 2023.

[41] M. Drif and A. J. M. Cardoso, "The use of the instantaneous-reactive-power signature analysis for rotor-cage-fault diagnostics in three-phase induction motors," *IEEE Transactions on Industrial Electronics*, vol. 56, no. 11, pp. 4606–4614, 2009.

[42] J. Hong, S. Park, D. Hyun, T.-J. Kang, S. B. Lee, C. Kral, and A. Haumer, "Detection and classification of rotor demagnetization and eccentricity faults for PM synchronous motors," *IEEE Transactions on Industry Applications*, vol. 48, no. 3, pp. 923–932, 2012.

[43] F. Mahmouditabar, A. Vahedi, and M. Bafghi, "Investigation of direct & quadrature current effects on demagnetization of flux switching permanent magnet motors," *IOP Conference Series: Materials Science and Engineering*, vol. 433, p. 012092, 11 2018.

[44] G. Choi and T. M. Jahns, "Demagnetization characteristics of permanent magnet synchronous machines," in *IECON 2014 - 40th Annual Conference of the IEEE Industrial Electronics Society*, pp. 469–475, 2014.

[45] S. Ruoho, J. Kolehmainen, J. Ikaheimo, and A. Arkkio, "Interdependence of demagnetization, loading, and temperature rise in a permanent-magnet synchronous motor," *IEEE Transactions on Magnetics*, vol. 46, no. 3, pp. 949–953, 2010.

[46] D.-K. Woo and B. H. Jeong, "Irreversible demagnetization of permanent magnet in a surface-mounted permanent magnet motor with overhang structure," *IEEE Transactions on Magnetics*, vol. 52, no. 4, pp. 1–6, 2016.

[47] J. D. McFarland and T. M. Jahns, "Influence of d- and q-axis currents on demagnetization in PM synchronous machines," in *2013 IEEE Energy Conversion Congress and Exposition*, pp. 4380–4387, 2013.

[48] S. Wang and H. Li, "Analysis of electromagnetic vibration of permanent magnet synchronous motor under static and dynamic eccentricity fault," in *2021 6th International Conference on Control and Robotics Engineering (ICCRE)*, pp. 106–111, 2021.

[49] D. Dorrell, W. Thomson, and S. Roach, "Analysis of airgap flux, current, and vibration signals as a function of the combination of static and dynamic airgap eccentricity in 3-phase induction motors," *IEEE Transactions on Industry Applications*, vol. 33, no. 1, pp. 24–34, 1997.

[50] A. Polat, Y. D. Ertuğrul, and L. T. Ergene, "Static, dynamic and mixed eccentricity of induction motor," in *2015 IEEE 10th International Symposium on Diagnostics for Electrical Machines, Power Electronics and Drives (SDEMPED)*, pp. 284–288, 2015.

[51] K. Gyftakis, *Eccentricity*. Lecture of the course "Special Chapters of Electrical Machines", Technical University of Crete, 2023.

[52] J. Zhao, X. Guan, C. Li, Q. Mou, and Z. Chen, "Comprehensive evaluation of inter-turn short circuit faults in PMSM used for electric vehicles," *IEEE Transactions on Intelligent Transportation Systems*, vol. 22, no. 1, pp. 611–621, 2021.

[53] L. Zhao, Y. Bai, X. Wang, and P. Zhao, "Inter-turn short circuit fault detection of a novel PMSM with fault tolerance," in *2023 8th International Conference on Power and Renewable Energy (ICPRE)*, pp. 209–213, 2023.

[54] K. M. Siddiqui, F. I. Bakhsh, R. Ahmad, and V. Solanki, "Advanced signal processing based condition monitoring of PMSM for stator-inter turn fault," in *2021 IEEE 8th Uttar Pradesh Section International Conference on Electrical, Electronics and Computer Engineering (UPCON)*, pp. 1–4, 2021.

[55] W. Huang, J. Du, W. Hua, W. Lu, K. Bi, Y. Zhu, and Q. Fan, "Current-based open-circuit fault diagnosis for PMSM drives with model predictive control," *IEEE Transactions on Power Electronics*, vol. 36, no. 9, pp. 10695–10704, 2021.

[56] T. Orlowska-Kowalska, M. Wolkiewicz, P. Pietrzak, M. Skowron, P. Ewert, G. Tarchala, M. Krzysztofiak, and C. T. Kowalski, "Fault diagnosis and fault-tolerant control of PMSM drives–state of the art and future challenges," *IEEE Access*, vol. 10, pp. 59979–60024, 2022.

[57] Y. Chen, S. Liang, W. Li, H. Liang, and C. Wang, "Faults and diagnosis methods of permanent magnet synchronous motors: A review," *Applied Sciences*, vol. 9, no. 10, 2019.

[58] K. N. Gyftakis, "Detection of early inter-turn stator faults in induction motors via symmetrical components - current vs stray flux analysis," in *2020 IEEE Energy Conversion Congress and Exposition (ECCE)*, pp. 796–801, 2020.

[59] A. Cardoso, S. Cruz, and D. Fonseca, "Inter-turn stator winding fault diagnosis in three-phase induction motors, by park's vector approach," *1997 IEEE International Electric Machines and Drives Conference Record*, vol. 14, no. 3, pp. 595–598, Sept. 1997.

[60] S. Cruz and A. Cardoso, "Stator winding fault diagnosis in three-phase synchronous and asynchronous motors, by the extended park's vector approach," *IEEE Transactions on Industry Applications*, vol. 37, no. 5, pp. 1227–1233, 2001.

[61] H.-J. Shin, J.-Y. Choi, H.-I. Park, and S.-M. Jang, "Vibration analysis and measurements through prediction of electromagnetic vibration sources of permanent magnet synchronous motor based on analytical magnetic field calculations," *IEEE Transactions on Magnetics*, vol. 48, no. 11, pp. 4216–4219, 2012.

[62] V. Gurusamy, E. Bostanci, C. Li, Y. Qi, and B. Akin, "A stray magnetic flux-based robust diagnosis method for detection and location of interturn short circuit fault in PMSM," *IEEE Transactions on Instrumentation and Measurement*, vol. 70, pp. 1–11, 2021.

[63] Y. Park, C. Yang, J. Kim, H. Kim, S. B. Lee, K. N. Gyftakis, P. A. Panagiotou, S. H. Kia, and G.-A. Capolino, "Stray flux monitoring for reliable detection of rotor faults under the influence of rotor axial air ducts," *IEEE Transactions on Industrial Electronics*, vol. 66, no. 10, pp. 7561–7570, 2019.

[64] P. Nantivatana, W. Kongyim, P. Tasungnuen, P. Nivorn, and P. Kocharoen, "Efficiency estimation of on-service three-phase induction motors using infrared thermography," in *2018 International Workshop on Advanced Image Technology (IWAIT)*, pp. 1–3, 2018.

[65] R. Hemmati, F. Wu, and A. El-Refaie, "Survey of insulation systems in electrical machines," in *2019 IEEE International Electric Machines & Drives Conference (IEMDC)*, pp. 2069–2076, May 2019.

[66] G. C. Stone, I. Culbert, E. A. Boulter, and H. Dhirani, *Electrical Insulation for Rotating Machines*. John Wiley & Sons, 2014.

[67] P. A. Panagiotou, A. Lambourne, and G. W. Jewell, "Survey of insulation in electrical machines for aerospace: Systems, materials & inspection," in *2022 International Conference on Electrical Machines (ICEM)*, pp. 2318–2324, 2022.

[68] T. Tanaka, G. Montanari, and R. Mulhaupt, "Polymer nanocomposites as dielectrics and electrical insulation-perspectives for processing technologies, material characterization and future applications," *IEEE Transactions on Dielectrics and Electrical Insulation*, vol. 11, no. 5, pp. 763–784, 2004.

[69] H. Xu, Q. Bu, X. Shang, and Q. Zhang, "Influence of voltage frequency and filler content on breakdown characteristics of epoxy resin," in *2023 IEEE 6th International Electrical and Energy Conference (CIEEC)*, pp. 3306–3311, 2023.

[70] R. Bartnikas and R. Morin, "Multi-stress aging of stator bars with electrical, thermal, and mechanical stresses as simultaneous acceleration factors," *IEEE Transactions on Energy Conversion*, vol. 19, no. 4, pp. 702–714, 2004.

[71] C. Yang, W. Cai, Y. Xie, B. Shao, and Y. Tang, "A novel model to accurately acquire hot spot location in hairpin end winding of oil-cooled PMSM," in *2023 26th International Conference on Electrical Machines and Systems (ICEMS)*, pp. 459–463, 2023.

[72] H. McDonald, P. D. Bastidas, S. Rowland, and S. Morsch, "Chemical analysis of solid insulation degradation using the AFM-IR technique," in *2018 IEEE 2nd International Conference on Dielectrics (ICD)*, pp. 1–4, 2018.

[73] A. Gegenava, A. Khazanov, and B. Moore, "Evaluation of electrical insulation quality for high voltage stator windings machines through visual inspection of dissected coils," in *2016 IEEE Electrical Insulation Conference (EIC)*, pp. 156–161, 2016.

[74] D. E. Moghadam, J. Speck, S. Grossmann, and J. Stahl, "Parameters affecting the turn insulation lifetime and durability," *IEEE Transactions on Dielectrics and Electrical Insulation*, vol. 25, no. 2, pp. 516–523, 2018.

[75] M. R. Rahimi, R. Javadinezhad, and M. Vakilian, "DC partial discharge characteristics for corona, surface and void discharges," in *2015 IEEE 11th International Conference on the Properties and Applications of Dielectric Materials (ICPADM)*, pp. 260–263, 2015.

[76] M. N. Horenstein, "A simulation model for understanding propagating brush discharges: Comparison of theory and experiments," *IEEE Transactions on Industry Applications*, vol. 47, no. 1, pp. 344–349, 2011.

[77] R. Zhao, J. Li, Y. Chen, B. Cui, Y. Teng, X. Kong, and B. Du, "Electrical treeing characteristics in glass fiber reinforced epoxy resin," in *2022 IEEE 4th International Conference on Dielectrics (ICD)*, pp. 643–646, 2022.

[78] S. Wu, S. Zheng, Z. Zhang, A. Zhong, R. Cao, and C. Wang, "The relationship between electrical tree growth and partial discharge characteristics in XLPE," in *2021 IEEE Electrical Insulation Conference (EIC)*, pp. 461–464, 2021.

[79] C. Forssen and H. Edin, "Modeling partial discharges in a cavity at different applied frequencies," in *2007 Annual Report - Conference on Electrical Insulation and Dielectric Phenomena*, pp. 132–135, 2007.

[80] D. Gowda and Anandraj, "Modeling of partial discharge (PD) for solid insulation with void and building a hardware setup to measure partial discharge," *2016 Biennial International Conference on Power and Energy Systems: Towards Sustainable Energy (PESTSE)*, pp. 1–7, 2016.

[81] G. Stone, E. A. Boulter, I. Culbert, and H. Dhirani, *OffLine Rotor and Stator Winding Tests*, pp. 235–283. 2004.

[82] H. W. Penrose, "Study of insulation resistance profiling use on random and form wound machines under 6kV," in *2012 IEEE International Symposium on Electrical Insulation*, pp. 606–608, 2012.

[83] "IEEE Recommended Practice for Testing Insulation Resistance of Rotating Machinery," *IEEE Std 43-2000*, pp. 1–28, 2000.

[84] D. L. McKinnon, "Insulation Resistance profile (IRP) and its use for assessing insulation systems," in *2010 IEEE International Symposium on Electrical Insulation*, pp. 1–4, 2010.

[85] H. Torkaman and F. Karimi, "Influence of ambient and test conditions on insulation resistance/polarization index in HV electrical machines - a survey," *IEEE Transactions on Dielectrics and Electrical Insulation*, vol. 22, no. 1, pp. 241–250, 2015.

[86] S. Grubic, R. G. Harley, T. G. Habetler, and J. A. Restrepo, "Sensitivity analysis of the surge test applied to ac machines," *2011 IEEE International Electric Machines & Drives Conference (IEMDC)*, pp. 618–623, 2011.

[87] "IEEE guide for testing turn insulation of form-wound stator coils for alternating-current electric machines," *IEEE Std 522-2023 (Revision of IEEE Std 522-2004)*, pp. 1–34, 2023.

[88] B. Gupta, "Risk in surge testing of turn insulation in windings of rotating machines," in *Proceedings: Electrical Insulation Conference and Electrical Manufacturing and Coil Winding Technology Conference (Cat. No.03CH37480)*, pp. 459–462, 2003.

[89] W. Chen, "The impact of high potential (HiPot) testing on globally VPI'ed stator winding," in *2015 IEEE 11th International Conference on the Properties and Applications of Dielectric Materials (ICPADM)*, pp. 987–990, 2015.

[90] "IEEE Recommended Practice for Insulation Testing of AC Electric Machinery (2300 V and Above) with High Direct Voltage," *IEEE Std 95-2002 (Revision of IEEE Std 95-1977)*, pp. 1–56, 2002.

[91] S. Mota, S. Prasad, A. Gopale, P. Parab, and R. Harchandani, "Generation of DC high voltage pulse for HiPot testing using PFN based marx generator," in *2019 International Conference on Intelligent Computing and Control Systems (ICCS)*, pp. 1386–1390, 2019.

[92] K. Kimura, "The role of IEC 60034-27-5 for IEC 60034-18-41: Offline PD test methods with repetitive impulse voltage," in *2017 International Symposium on Electrical Insulating Materials (ISEIM)*, vol. 1, pp. 155–158, 2017.

[93] B. K. Gupta, G. C. Stone, and J. Stein, "Stator winding hipot (high potential) testing," in *2009 IEEE Electrical Insulation Conference*, pp. 409–413, 2009.

[94] E. David, G. Stone, and M. Sasic, "Dielectric response of machine insulation extracted from DC ramp test on individual stator bars," in *2017 IEEE Electrical Insulation Conference (EIC)*, pp. 46–49, 2017.

[95] A. Nair, É. David, and T. Godin, "Experience with DC ramp test performed on asphalt-mica insulated hydraulic generators," *Conference Record of the 2008 IEEE International Symposium on Electrical Insulation*, pp. 166–169, 2008.

[96] V. Warren-Iris, B. F. Moore, and J. Williams, "Condition assessment of stator windings in medium voltage GVPI machines," in *Bradley's Motors*, 2015.

[97] "IEEE Guide for the Measurement of Partial Discharges in AC Electric Machinery," *IEEE Std 1434-2014 (Revision of IEEE Std 1434-2000)*, pp. 1–89, 2014.

[98] A. S. Guedes, S. M. Silva, B. de Jesus Cardoso Filho, and C. A. Conceição, "Evaluation of electrical insulation in three-phase induction motors and classification of failures using neural networks," *Electric Power Systems Research*, vol. 140, pp. 263–273, 2016.

[99] "IEC 60270 – High-voltage test techniques – Partial discharge measurements," *3rd edition, IEC*, 2000.

[100] *A Guide for Partial Discharge Measurements on medium voltage (MV) and high voltage (HV) apparatus.*

[101] Y. Ji, P. Giangrande, W. Zhao, V. Madonna, X. Zhang, H. Zhang, and M. Galea, "Partial discharge investigation under humidity conditions via dissipation factor and insulation capacitance tip-up test," *IEEE Transactions on Dielectrics and Electrical Insulation*, vol. 29, no. 4, pp. 1483–1490, 2022.

[102] M. Farahani, H. Borsi, and E. Gockenbach, "Study of capacitance and dissipation factor tip-up to evaluate the condition of insulating systems for high voltage rotating machines," *Electrical Engineering*, vol. 89, pp. 263–270, 03 2007.

[103] K. Younsi, P. Neti, M. Shah, J. Y. Zhou, J. Krahn, K. Weeber, and D. Whitefield, "Online capacitance and dissipation factor monitoring of AC motor stator insulation," in *2010 IEEE International Power Modulator and High Voltage Conference*, pp. 530–533, 2010.

[104] "IEEE recommended practice for measurement of power factor tip-up of electric machinery stator coil insulation," *IEEE Std 286-2000*, pp. 1–29, 2000.

[105] R. Omranipour and S. U. Haq, "How critical are IEC 60034-27-3 maximum values for dielectric dissipation factor and tip-up to determine the reliability of motor stator insulation?," in *2015 IEEE Electrical Insulation Conference (EIC)*, pp. 364–368, 2015.

[106] M. K. Stranges, S. Ul Haq, and A. O. Vouk, "Monitoring stator insulation in critical motors: Choosing diagnostic tests," *IEEE Industry Applications Magazine*, vol. 20, no. 1, pp. 50–55, 2014.

[107] A. Mugarra, C. Platero, J. Martínez, and U. Albizuri-Txurrka, "Large salient pole synchronous machines field windings diagnosis by frequency response," in *2018 XIII International Conference on Electrical Machines (ICEM)*, pp. 1875–1880, 2018.

[108] M. Bagheri, M. S. Naderi, T. Blackburn, and T. Phung, "Frequency response analysis and short-circuit impedance measurement in detection of winding deformation within power transformers," *IEEE Electrical Insulation Magazine*, vol. 29, no. 3, pp. 33–40, 2013.

[109] P. A. Panagiotou, A. Lambourne, and G. W. Jewell, "Ex-situ inspection of concentrated stator coils by means of impedance spectroscopy," in *2022 International Conference on Electrical Machines (ICEM)*, pp. 2331–2337, 2022.

[110] C. Hao and B. Gao, "Study on the frequency domain dielectric spectroscopy of rotating machines insulation," in *2016 IEEE International Conference on High Voltage Engineering and Application (ICHVE)*, pp. 1–4, 2016.

[111] E. David and L. Lamarre, "Influence of rise time on dielectric parameters extracted from time domain spectroscopy in the context of generator stator insulation," *IEEE Transactions on Dielectrics and Electrical Insulation*, vol. 12, no. 3, pp. 423–428, 2005.

[112] P. A. Panagiotou, E. J. W. Stone, J. Mühlthaler, A. Reeh, A. Lambourne, and G. W. Jewell, "Thermal degradation profile of concentrated stator winding insulation by impedance spectroscopy," in *2023 IEEE 14th International Symposium on Diagnostics for Electrical Machines, Power Electronics and Drives (SDEMPED)*, pp. 554–560, 2023.

[113] F. Perisse, P. Werynski, and D. Roger, "A new method for AC machine turn insulation diagnostic based on high frequency resonances," *IEEE Transactions on Dielectrics and Electrical Insulation*, vol. 14, no. 5, pp. 1308–1315, 2007.

[114] P. Neti and S. Grubic, "Online broadband insulation spectroscopy of induction machines using signal injection," in *2014 IEEE Energy Conversion Congress and Exposition (ECCE)*, pp. 630–637, 2014.

[115] N. Lahoud, J. Faucher, D. Malec, and P. Maussion, "Electrical aging of the insulation of low-voltage machines: Model definition and test with the design of experiments," *Industrial Electronics, IEEE Transactions on*, vol. 60, pp. 4147–4155, 09 2013.

[116] Z. Jia, Y. Hao, and H. Xie, "The degradation assessment of epoxy/mica insulation under multi-stresses aging," *IEEE Transactions on Dielectrics and Electrical Insulation*, vol. 13, no. 2, pp. 415–422, 2006.

[117] F. Guastavino, A. Ratto, E. Torello, and G. Biondi, "Aging tests on nanostructured enamels for winding wire insulation," *IEEE Transactions on Industrial Electronics*, vol. 61, no. 10, pp. 5550–5557, 2014.

[118] M. Farahani, E. Gockenbach, H. Borsi, K. Schäfer, and M. Kaufhold, "Behavior of machine insulation systems subjected to accelerated thermal aging test," *IEEE Transactions on Dielectrics and Electrical Insulation*, vol. 17, no. 5, pp. 1364–1372, 2010.

[119] G. Stone, B. Gupta, J. Lyles, and H. Sedding, "Experience with accelerated aging tests on stator bars and coils," in *IEEE International Symposium on Electrical Insulation*, pp. 356–360, 1990.

[120] M. Istad, M. Runde, and A. Nysveen, "A review of results from thermal cycling tests of hydrogenerator stator windings," *IEEE Transactions on Energy Conversion*, vol. 26, no. 3, pp. 890–903, 2011.

[121] H. Zhu, C. Morton, and S. Cherukupalli, "Quality evaluation of stator coils and bars under thermal cycling stress," *Conference Record of the 2006 IEEE International Symposium on Electrical Insulation*, pp. 384–387, 2006.

[122] G. Stone, J. Lyles, J. Braun, and C. Kaul, "A thermal cycling type test for generator stator winding insulation," *IEEE Transactions on Energy Conversion*, vol. 6, no. 4, pp. 707–713, 1991.

[123] K. N. Gyftakis, P. A. Panagiotou, N. Lophitis, D. A. Howey, and M. D. McCulloch, "Breakdown resistance analysis of traction motor winding insulation under thermal ageing," in *2017 IEEE Energy Conversion Congress and Exposition (ECCE)*, pp. 5819–5825, Oct. 2017.

[124] K. N. Gyftakis, M. Sumislawska, D. F. Kavanagh, D. A. Howey, and M. D. McCulloch, "Dielectric characteristics of electric vehicle traction motor winding insulation under thermal aging," *IEEE Transactions on Industry Applications*, vol. 52, no. 2, pp. 1398–1404, 2016.

[125] M. Sumislawska, K. N. Gyftakis, D. F. Kavanagh, M. D. McCulloch, K. J. Burnham, and D. A. Howey, "The impact of thermal degradation on properties of electrical machine winding insulation material," *IEEE Transactions on Industry Applications*, vol. 52, no. 4, pp. 2951–2960, 2016.

[126] P. A. Panagiotou, K. N. Gyftakis, N. Lophitis, M. D. McCulloch, and D. A. Howey, "Investigation of traction motor windings' insulation capacitance at switching frequencies under accelerated thermal stress," in *2017 IEEE 11th International Symposium on Diagnostics for Electrical Machines, Power Electronics and Drives (SDEMPED)*, pp. 537–543, 2017.

[127] S. J. Williamson, R. Wrobel, J. Yon, J. D. Booker, and P. H. Mellor, "Investigation of equivalent stator-winding thermal resistance during insulation system ageing," in *2017 IEEE 11th International Symposium on Diagnostics for Electrical Machines, Power Electronics and Drives (SDEMPED)*, pp. 550–556, 2017.

[128] M. Sumislawska, K. N. Gyftakis, D. F. Kavanagh, M. McCulloch, K. J. Burnham, and D. A. Howey, "The impact of thermal degradation on electrical machine winding insulation," in *2015 IEEE 10th International Symposium on Diagnostics for Electrical Machines, Power Electronics and Drives (SDEMPED)*, pp. 232–238, 2015.

[129] V. Madonna, P. Giangrande, and M. Galea, "Influence of thermal aging on the winding thermal conductivity in low voltage electrical machines," in *2020 23rd International Conference on Electrical Machines and Systems (ICEMS)*, pp. 123–128, 2020.

[130] H. Wang and R. Busch, "A discussion of some concepts in thermal aging test-thermal aging and thermal breakdown," in *ICSD'98. Proceedings of the 1998 IEEE 6th International Conference on Conduction and Breakdown in Solid Dielectrics (Cat. No.98CH36132)*, pp. 443–446, 1998.

[131] V. Madonna, P. Giangrande, G. Migliazza, G. Buticchi, and M. Galea, "A time-saving approach for the thermal lifetime evaluation of low-voltage electrical machines," *IEEE Transactions on Industrial Electronics*, vol. 67, no. 11, pp. 9195–9205, 2020.

[132] B. Nageshwar Rao, A. Sudhindra, and B. Ramachandra, "Low frequency dielectric response of thermally degraded epoxy-mica insulation," in *2009 IEEE 9th International Conference on the Properties and Applications of Dielectric Materials*, pp. 1026–1029, 2009.

[133] I. M. Y. Negara, N. K. Aryani, D. A. Asfani, D. Fahmi, R. Jauhari, and M. Wahyudi, "Analysis of physical and electrical characteristics of transformer oil insulation during accelerated thermal aging experiment and its lifetime estimation using arrhenius law and breakdown voltage test," in *2017 International Seminar on Intelligent Technology and Its Applications (ISITIA)*, pp. 139–143, 2017.

[134] D. F. Kavanagh, K. N. Gyftakis, and M. D. McCulloch, "Thermal degradation phenomena of polymer film on magnet wire for electromagnetic coils," *IEEE Transactions on Industry Applications*, vol. 57, no. 1, pp. 458–467, 2021.

[135] Z. Zhao, Y. Chen, Y. Yu, M. Han, C. Tang, and C. Yao, "Equivalent broadband electrical circuit of synchronous machine winding for frequency response analysis based on gray box model," *IEEE Transactions on Energy Conversion*, vol. 36, no. 4, pp. 3512–3521, 2021.

[136] H. Elmadah, D. Roger, and N. Takorabet, "HF model of high temperature machine coils," in *2019 19th International Symposium on Electromagnetic Fields in Mechatronics, Electrical and Electronic Engineering (ISEF)*, pp. 1–2, 2019.

[137] X. Cao, H. Yang, and X. Bai, "Equivalent capacitance model of segmented induction coil in electromagnetic exploration system for deep resources," *IEEE Sensors Journal*, vol. 21, no. 6, pp. 7756–7767, 2021.

[138] H. Zhang, S. Wang, D. Yuan, and X. Tao, "Double-ladder circuit model of transformer winding for frequency response analysis considering frequency-dependent losses," *IEEE Transactions on Magnetics*, vol. 51, no. 11, pp. 1–4, 2015.

[139] K. Nakahara and F. Kuroki, "Equivalent circuit model of multi-layered coils for integrated sensor applications in medium-wave frequencies," in *2016 IEEE International Symposium on Radio-Frequency Integration Technology (RFIT)*, pp. 1–3, 2016.

[140] W. Xue, Z. Huang, X. Xu, B. Shen, and Z. Jin, "Ramping loss analysis of no-insulation HTS coil under external field using an improved equivalent circuit model," *IEEE Transactions on Applied Superconductivity*, vol. 31, no. 8, pp. 1–5, 2021.

[141] X. Chen, Z. Zhang, S. Yu, and T.-G. Zsurzsan, "Fringing effect analysis of parallel plate capacitors for capacitive power transfer application," in *2019 IEEE 4th International Future Energy Electronics Conference (IFEEC)*, pp. 1–5, 2019.

[142] P. Chen, J. Liu, H. Zhang, and B. Chu, "Increase of capacitance of thick dielectrics by fringe effect," *IEEE Transactions on Dielectrics and Electrical Insulation*, vol. 26, no. 5, pp. 1716–1719, 2019.

[143] G. Lv, D. Zeng, and T. Zhou, "Analysis of secondary losses and efficiency in linear induction motors with composite secondary based on space harmonic method," *IEEE Transactions on Energy Conversion*, vol. 32, no. 4, pp. 1583–1591, 2017.

[144] Y. Feng, B. Shao, X. Tang, Y. Han, T. Wu, and Y. Suzuki, "Improved capacitance model involving fringing effects for electret-based rotational energy harvesting devices," *IEEE Transactions on Electron Devices*, vol. 65, no. 4, pp. 1597–1603, 2018.